UNIVERSIDADE DE LISBOA
FACULDADE DE CIÊNCIAS
DEPARTAMENTO DE ENGENHARIA GEOGRÁFICA, GEOFÍSICA E ENERGIA

Laser shallow melting of p-type silicon wafers as substrates for tunnel junctions in tandem solar cells

Yan Ribeiro Cardoso de Souza

Mestrado Integrado em Engenharia da Energia e do Ambiente

Dissertação orientada por:
Doutor Guilherme Gaspar
Prof. Doutor Killian Lobato

2022

– BLANK PAGE –

– PÁGINA EM BRANCO –

Acknowledgments

First, I would like to express my appreciation towards Doctor Guilherme Gaspar and Professor Killian Lobato, for the opportunity to embrace this project, the effort, and the valuable guidance, which helped me complete this dissertation.

To S-LoTTuSS research members, for the help and feedback in many matters, especially Afonso Guerra and Filipe Serra.

To the two most important people in my life, my mother and my father, for the unconditional love and support throughout my life, and to all my family.

To Ana, thank you for sticking by my side through thick and thin. Forever with you and for you.

To my friends Diogo and Filipe, for the brotherhood.

To the amazing people I've met at the university, Carolina, David, Tiago, Joana and Adriana.

Finally, to all the University of Lisbon - Faculty of Sciences community, for the acceptance and overall, personal and professional, growth.

This dissertation was supported by the S-LoTTuSS project through the grant agreement PTDC/CTM-CTM/28962/2017, financed by national funds FCT/MCTES (PIDDAC).

Abstract

The fabrication of tandem solar cells requires a specific connectivity between layers, with specific characteristics such as the case of a tunnel junction that is made of two heavily doped narrow layers of different doping types (e.g. Phosphorus and Boron). When a certain amount of voltage is applied to the edges of the tunnel junction, the result is the alignment of both valence and conduction bands of the different subregions, enabling the electron flux from one cell to another without the need to energy variation of the electron.

The Gas Immersion Laser Doping (GILD) technique uses a laser as the source of radiation and a dopant gas. A silicon wafer is inserted inside a compartment with a controlled atmosphere saturated with the doping gas, which receives energy from the laser as pulsed beams, melting and solidifying into a very fast process. When the melting occurs, the dopants penetrate the wafer and remain there upon solidification. When a high concentration of the dopant is confined inside an ultra-shallow depth of the wafer, the probability of forming a tunnel junction is increased. Therefore, before implementing this process, it is necessary to study the interaction between the laser and silicon samples.

The purpose of this dissertation is to test and pre-select sample areas that were submitted to an infrared laser irradiation, varying on different sets of parameters, such has laser scan speed, number of scans, infrared transparent window type, among others. Samples will be evaluated regarding their topography, in terms of surface and in-depth melt homogeneity. These samples will be used as tests for the objective of the project in which this dissertation is inserted. The final goal of the project is thus to develop a process of tunnel junction formation with recurse to the GILD technique, using $POCl_3$ as the dopant source and to create abrupt n++/p+ doping profiles (with 10 nm wide). The approach should lead to a scalable and low-cost industrial process for forming tunnel junctions directly integrated in tandem solar cells.

Optical analysis of laser interaction on the silicon surface can be notable in slower laser scan speed for more than one successive scattering process. The results show an effective laser processed areas in a p-type Cz-Si wafer rather than in an emitter p++ on an p+ Cz-Si wafer. The chamber and the window that confines the sample in a controlled atmosphere affects positively the melting process when using a Quartz material rather than the Polycarbonate window.

Keywords: Laser-Silicon Interaction, Silicon Solar Cells, Tunnel Junctions, Wafer Melting.

Resumo

A evolução tecnológica tem permitido arranjar solução eficazes para combater a produção de energia à base de combustíveis fósseis. As energias renováveis estão a ser cada vez mais implementadas como fontes de conversão de energia primária para autoconsumo e distribuição na rede. A variabilidade e a inconstância que as fontes de energia renovável apresentam, devem ser colmatadas pontualmente por fontes alternativas ou convencionais de produção de energia, para garantir ao consumidor final de energia a sua utilização.

Por definição, uma célula fotovoltaica é um dispositivo elétrico que é afetado pela exposição a certos tipos de radiação, resultando num diferencial em características como a corrente e a tensão. Baseia-se num efeito químico e físico, denominado por efeito fotovoltaico. Através da absorção de fotões por parte de um material semiconductor, ocorre a excitação dos seus eletrões e, consequentemente, a separação do respetivo átomo. É gerada uma diferença de potencial elétrico proporcionada pela separação das cargas.

A radiação proveniente do sol é um recurso muito explorado atualmente, para produção de energia de fonte renovável. A irradiância espetral atinge valores máximos na região do infravermelho, permitindo correlacionar o grande destaque que o silício detém no mercado fotovoltaico, já que o intervalo de banda do mesmo encontra-se na região infravermelha, onde converte de forma eficiente grandes quantidades de radiação.

O aproveitamento das restantes regiões do espetro solar deverá ser considerado para a implementação nas futuras células solares. O empilhamento de camadas de diferentes materiais, permite abranger uma maior banda de comprimento de onda. A célula de topo permite absorver intervalos de banda superiores, enquanto os fotões que não são absorvidos percorrem a junção até chegar à célula base, onde irá ocorrer a conversão de energia. Uma célula solar *tandem* como é o caso da perovskita/silício resulta numa célula mais eficiente em que são aproveitados os fotões de diferentes regiões do espetro solar.

As células solares *tandem* são compostas por diferentes sub-células que têm intervalos de banda do espetro solar distintos. Permitem uma maior absorção de fotões pois abrangem um maior intervalo do comprimento de onda. A sua fabricação requer uma interligação complexa entre ambas as camadas denominadas por junção de túnel. Trata-se de uma região altamente dopada com duas camadas com concentração de dopantes distintos, como por exemplo Boro e Fósforo. Ambas as bandas de valência e condução das diferentes camadas alinham-se, possibilitando o fluxo de eletrões entre ambas sem necessidade de o fotão variar a sua energia.

O silício é o material semiconductor mais utilizado para o fabrico de células solares. Consoante o seu grau de cristalinidade, poderá apresentar diferentes eficiências e consequentemente, custos, face à complexidade dos processos em que é submetido. A maioria dos módulos fotovoltaicos utilizados nas centrais são do tipo monocristalino, apresentando uma maior eficiência comparativamente às outras células de primeira geração.

A eficiência da tecnologia fotovoltaica pode ser maximizada através de um processo denominado por dopagem. Ao introduzir impurezas em amostras, como por exemplo de silício, a conversão de energia é realizada de forma mais eficaz devido à alteração das propriedades elétricas. Dependendo da natureza das impurezas que serão inseridas nas amostras, será possível obter amostras

do tipo *p* ou do tipo *n*. A alteração da cristalinidade de uma bolacha de silício afetará as ligações covalentes entre os átomos. A liberdade de movimento de um eletrão em amostras do tipo *n*, aumentará a condutividade e, consequentemente, a eficiência da célula num todo.

A técnica GILD (*Gas Immersion Laser Doping*) é uma das alternativas para realizar processos de dopagem em silício. É utilizado um laser pulsado como fonte principal de radiação e uma atmosfera com um gás dopante. A amostra de silício permanece confinada num compartimento que possibilite criar uma atmosfera controlada com alta concentração de gás dopante. O laser pulsado incide na superfície da amostra proporcionando a fusão e solidificação intercalada, num processo extremamente rápido. Durante a fusão do silício, o dopante penetra a amostra, que permanece em profundidade quando ocorre a solidificação. Uma elevada concentração de dopante alocada numa camada ultra-fina, propicia a formação de uma junção de túnel. De forma a maximizar a eficácia da dopagem para o resultado pretendido, é fundamental analisar a interação entre o laser e o silício, e todos os fatores que estão associados.

A técnica SEM (*Scanning Electron Microscopy*) é bastante utilizada para estudar a topografia de células após a interação direta com fontes de energia muito elevadas. Um feixe primário de eletrões é disparado diretamente na superfície da amostra que, após o contacto, resulta na emissão de eletrões secundários. Estes são armazenados e filtrados por um sistema de deteção que, consequentemente, irá correlacionar a variação na topografia da superfície amostral. O estudo da interação entre fontes de energia e amostras de silício é fundamental de modo a compreender a os fatores que possibilitam uma melhor homogeneidade superficial.

O principal objetivo desta dissertação é testar, analisar e escolher as áreas amostrais que serão submetidas a um processo de irradiação recorrendo a um laser infravermelho, variando um conjunto de parâmetros, tais como, a velocidade de varrimento do laser, o número de repetições de cada ciclo de varrimento, o material que constitui a janela onde incide o laser, entre outros. Futuramente, as amostras que forem escolhidas, serão avaliadas relativamente à sua topografia, tanto em termos superficiais, como na fusão homogénea em profundidade. As amostras serão utilizadas como amostras teste para o objetivo do projeto em que esta dissertação se insere. O projeto tem a finalidade de desenvolver o processo de formação de junções de túnel pelo método de *Gas Immersion Laser Doping* utilizando como gás dopante o $POCl_3$, de forma a criar uma camada ultra-fina e altamente dopada do tipo n (n++) através de toda a bolacha de silício.

Um estudo preliminar acerca da interação entre laser e silício permite compreender de que maneira os vários fatores, tal como o tipo de equipamento, parâmetros e o tipo de amostra de silício utilizada, influenciam a homogeneidade do processo de fusão. Foram estudados e analisados os diferentes resultados comparando diretamente as várias variáveis. O material que constituía a janela onde incidia o laser, a velocidade de varrimento do pulso, a distância entre pontos focais (sucessivos e verticais) e a repetição do varrimento do laser, as diferentes amostras (emissor p++/p+ e bolacha p+, ambos de silício), foram comparados no âmbito desta dissertação. O processo de fabricação deverá conduzir a um método escalável e de baixo custo na produção industrial de junções de túnel para integrar nas células solares *tandem*.

Numa análise microscópica das diferentes áreas amostrais é possível observar que a velocidade de varrimento do laser e o número de repetições dos ciclos de varrimento são as variáveis que mais influenciam na eficácia da fusão do silício. Em velocidades mais baixas do feixe do laser, é possível obter uma maior área cujo laser interagiu com sucesso. Mesmo que existam pequenas zonas escuras, a sucessiva repetição do processo resulta numa correção da zona não tratada.

Num emissor sobre um wafer dopado (p++/p+) a interação do laser tornou-se numa fusão deficiente da superfície face à bolacha padrão (bolacha de silício tipo *p*). A grande concentração de boro na camada superior afeta negativamente a eficácia do processo de varrimento.

A fusão homogénea do silício foi afetada positivamente quando utilizada uma janela de Quartzo como superfície transparente que permite a incidência do laser. Face à janela de policarbonato, os fatores óticos dos dois tipos de materiais, são notavelmente relevantes nos resultados obtidos.

Palavras-Chave: Interação entre Laser e Silício, Células Solares de Silício, Junções de túnel, Fusão de Silício.

Index

List of Figures

List of Tables

List of Abbreviations and Acronyms

AFM	Atomic Force Microscopy
BSF	Back Surface Field
CIGS	Copper-Indium-Gallium-Selenide
CVD	Chemical Vapor Deposition
Cz	Czochralski
C-V	Capacitance-Voltage technique
ECV	Electrochemical Capacitance-Voltage
EQE	External Quantum Efficiency
EU	European Union
FF	Fill Factor
FWHM	Full Width at Half Maximum
GILD	Gas Immersion Laser Doping
IBC-SHJ	Interdigitated Back Contacts - Silicon Heterojunction
ICEMS/ IST	Institute of Materials and Surfaces Science and Engineering
I-V	Current-Voltage
MPP	Maximum Power Point
Nd:YAG	Neodymium-Doped Yttrium Aluminium Garnet
PECVD	Plasma Enhanced Chemical Vapor Deposition
PhCS	Photo Current Source
PSC	Perovskite Solar Cells
P-RTD	Proximity Rapid Thermal Diffusion
PV	Solar Photovoltaic
SEM	Scanning Electron Microscopy
SIMS	Secondary Ion Mass Spectroscopy
S-LoTTuSS	Scalable Low-cost Tandem Tunnel Junctions for Silicon Solar Cells
TCO	Transparent Conductive Oxide

List of Symbols and Units

A	Area
AM_0	Air Mass- zero atmosphere
$AM_{1.5\ Global}$	Air Mass- 1.5 atmospheres
AsH_3	Arsine
a-Si	Amorphous Silicon
a-Si:H	Hydrogenated Amorphous Silicon
a-Si:H (i)	i-doped Hydrogenated Amorphous Silicon
a-Si:H (n+)	n-doped Hydrogenated Amorphous Silicon
a-Si:H (p+)	p-doped Emitter Hydrogenated Amorphous Silicon
a-Si:H/c-Si	Hydrogenated Amorphous Silicon/ Crystalline silicon
B_2H_6	Diborane
BCl_3	Boron Trichloride
BF_3	Boron Trifluoride
c	Speed of light
$CaTiO_3$	Perovskite
Cd-free	Cadmium free
CdS	Cadmium Sulfide
CdTe	Cadmium Telluride
$CH_3NH_3PbY_3$	Methylammonium Lead Halide
$CH_3NH_3SnY_3$	Methylammonium Tin Halide
cm	Centimeter
cm^2	Square centimeter
cm^{-3}	Inversed cubic centimeter
CO_2	Carbon Dioxide
$Cu(InGa)Se_2$	Copper Indium Galium Selenide
$CuIn_yGa_{(1-y)}Se_2$	Copper Indium Gallium Selenide
d	Distance between the centre of two consecutive horizontal laser paths
E	Energy
E_c	Conduction Band
E_F	Fermi Level
E_g	Bandgap energy
eV	Electron-Volt
E_v	Valence Band
Fe	Iron
Fe	Force to accelerate electrons
F_R	Repelling force
G	Solar radiation
GaAs	Gallium Arsenide
h	Planck's constant
HF	Hydrofluoric Fluoride
Hz	Hertz
I_0	Diode reverse saturation current
I_D	Diode reverse saturation current
I_{MPP}	Current at maximum point conditions
I_{ph}	Photo current
I_s	Solar cell current
I_{sc}	Short circuit current
I_{sh}	Shunt current

J	Joules
k	Boltzmann's constant
K	Kelvin
k	Representing a certain sample area identification
ln	Natural logarithm of a number
m	Meter
m^2	Cubic meter
mA	Milliampere
mbar	Millibar
mJ	Millijoule
mm	Millimeter
mm^2	Square millimeter
n^+	N-doped layer
N_2	Nitrogen
n	Diode ideality factor
n	Number of scan's
nm	Nanometres
ns	Newton-second
^oC	Celsius
$p++$	Heavily p-doped layer
p^+	P-doped layer
Pb	Lead
PCl_3	Phosphorus trichloride
P_{ideal}	Ideal output power
P_{MPP}	Power at maximum point conditions
$POCl_3$	Phosphoryl chloride
p-n	p-n junction
q	Electron charge
R	Reflectance
R_s	Series resistance
R_{sh}	Shunt resistance
Si	Crystalline Silicon
Sn	Tin
t	time
T_0	Solar cell temperature
t_k	Time of a certain sample area identification
v	Laser´s scan speed
V	Voltage
V_{MPP}	Voltage at maximum power conditions
V_{oc}	Open circuit voltage
V_T	Thermal voltage
V_x	Diode and shunt resistance voltage
W	Watt
XeCl	Xenon monochloride
λ	Wavelength
µm	Micrometres
Ω	Ohm
η	Efficiency

1. Introduction

In the last three decades, the electricity demand has been increasing. In 2018, around 21% of the final energy consumed in the European Union (EU) belongs to electricity. Even though the renewable energy production is increasing, we still depend largely on fossil fuel-based power stations (~40%) to support European electricity grid. The renewable energy sources yet manage to stay above the nuclear power plants with a share of 33% and 26%, respectively. The most impactful renewable electricity production comes from wind turbines (11%), hydroelectric power plants (13%) and solar power with the lowest value among them (4%) [**1**].

The solar photovoltaic (PV) industry is continuously growing. Nowadays, the contribution is still a reduced portion of the total electricity production. PV implementation alongside the Mediterranean and Portugal has revealed to be a viable project with a potential to generate between 1100 and 1300 kWh/kW_p annually, using PV system based on typical crystalline Silicon (Si) panels without an angle optimization, mounted horizontally [**2**]. PV installation on urban areas, became a self-sufficient alternative since the electricity produced can be self-consumed or even sold to the electrical grid. The improvement of photovoltaic cells and technology is being studied for a long time, and the best way to increase its contribution for energy production is improving the conversion efficiency of the device.

The most common semiconductor material used in the fabrication of solar cells is silicon and it can have different types of crystallinities. It's considered three types, amorphous, multicrystalline, and monocrystalline, each type presenting different production costs and efficiencies Monocrystalline silicon presents a solid four-bonded tetrahedral structure and unbroken crystal lattice with an array of molecular connections each oriented the same way. This type delivers a higher efficiency but with a bigger cost. Multicrystalline silicon is formed by small crystals through the Siemens process. After this process, it's created a solid material with various small crystals (or grains) connect to each other with different sizes and orientations. This type of *Si* compared to monocrystalline has a lower efficiency but it's the cheapest of the first-generation solar cells.

Entering the second-generation solar cells, we have the amorphous silicon which is commonly used for thin films transistors rather than actual solar cells. This type has no molecular connection order, presenting a random network and resulting in an anomalous electrical behaviour. bonds, producing Hydrogenated Amorphous Silicon (a-Si:H). It's a technic that increase the performance since it reduces the electrical irregularity but on the other hand accelerate the material degradation induced by light. [**3**]

In addition to Si, there are other semiconductor materials with good electronic grade, those other options need to have a very pure crystallinity grade. A solid periodic array with aligned atoms seems to magnify semiconductor's electronic properties [**4**]. The covalent bonds with four electron connections between atoms in an array represent a strong bond, for example silicon. Being an element from the fourteenth group of the periodic table means that it has four valence electrons.
A similar array arrangement occurs in other combinations such has CdTe and GaAs. These two have an average of four valence electron with a covalent bond of two valence electron. CdTe and GaAs are examples of Silicon equivalent structural crystalline grade and belong to the second-generation solar cells or known as thin films technologies. Another thin films cell used nowadays is CIGS (Copper-Indium-Gallium-Selenide), $Cu(InGa)Se_2$, noted to have a high absorption coefficient.

Third generation solar cells are the most current type of emerging technology, focusing on a multi-layer combination to increase the photon absorption and consequentially the efficiency. Tandem

cells are devices that gather two different cells, each having different bandgaps, being able to absorb complementary solar spectrum wavelength regions. These devices can present a theoretical maximum value of 46.1% [5]. A tandem cell can be built with a monolithic architecture, where the top cell is fabricated directly above the top of the base cell using, either a recombination layer or a tunnel junction Perovskite is a good choice as top subcell, which stacked onto a Si base subcell, can be a revolution to the PV proliferation in a near future. Si absorbing mostly in infrared region and perovskite with a mean bandgap of around 1.95 eV has a high absorbance along the visible region of the spectrum will provide an External Quantum Efficiency (EQE), as shown in Figure 1.1, high distributed and with nearly no overlap of each individual subcell.

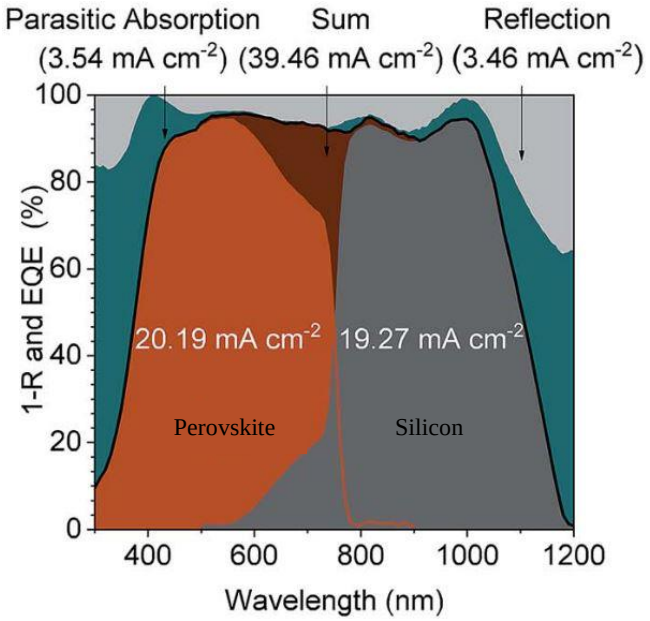

Figure 1.1. External quantum efficiency of a tandem cell composed by perovskite top subcell with heterogenous silicon base subcell, representing the utilization of incident light. Additionally, the 1-Reflectance (1-*R*) and the parasitic absorption, composing the integrated current loss from the same device. [6]

1.1. Objectives

This dissertation's purpose is to study a set of laser parameters and setup variables to further obtain laser processed Si samples with suitable surface melting/crystallization characteristics that suit the context of a Si tunnel junction for tandem solar cells. A pre-selection of laser processed samples will be made due to evaluate of its homogeneity and low melting depth, for future doping process that can lead to heavily doped, homogenous and low junction depth Si wafers.

This dissertation is inserted into the context of S-LoTTuSS (Scalable Low-cost Tandem Tunnel Junctions for Silicon Solar Cells) having concordance with its objectives. The goal of the project is to develop and characterize tunnel junction production through a scalable and low-cost process for tandem solar cells.

1.2. Structure

This dissertation will be divided into six chapters: Introduction, State of the art, Methodology, Results and Conclusions.

In the state of the art is compiled all relevant information throughout the development of this dissertation, which includes the solar spectrum, the constitution of different types of solar cells, the structure of tandem solar cells and its components, the tunnel junction effect and its electric behaviour, doping technics emphasising the Gas Immersion Laser Doping (GILD) method, and different types of tunnel junction characterizations.

In the methodology it will be described the experimental procedure for the diverse types of laser-silicon interactions, including the sample areas scheme for both emitter (p++/p+ wafer) and standard p-type silicon wafer, the set of parameters inserted on the laser scan and sample are sequence. It will be explained and identified some of the main components that affect the experiments, such as the laser, chamber, samples window and microscope.

In the results and analysis chapter are presented the chambers leakage test results and all the laser and silicon interactions. Some predicted results will be stated, the registered group of figures will be compared and commented relating what was expected and the results. All the phenomena that were identified will be submitted to an analysis and some ideas relating the cause will be explained.

At last, in conclusion, an overall evaluation of the different variables and components that were taken into consideration will be summarized.

2. State of the Art

In this chapter will be presented the main searched subjects to better understand the development of this dissertation objectives.

2.1. Solar Spectrum

Solar radiation is a result of Sun's constant nuclear fusion reactions, emitting an electromagnetic radiation with large amounts of energy. For solar cells it is considered two types of spectrums, the AM_0 is a standard spectrum with an integrated power around 1366 W/m^2 outside Earth's atmosphere. PV modules characterized by AM_0, for example GaAs, have better incident radiation flux. The $AM_{1.5;Global}$ spectrum affect the major solar project installations. It represents 1.5 atmospheres because in a global scale it's important to take in consideration the solar zenith angle, while 1 atmosphere is represented only around equatorial region. This spectrum defines the terrestrial solar panels, and it is designed for flat PV modules with an integrated power of 1000 W/m^2 (G) [**7**].

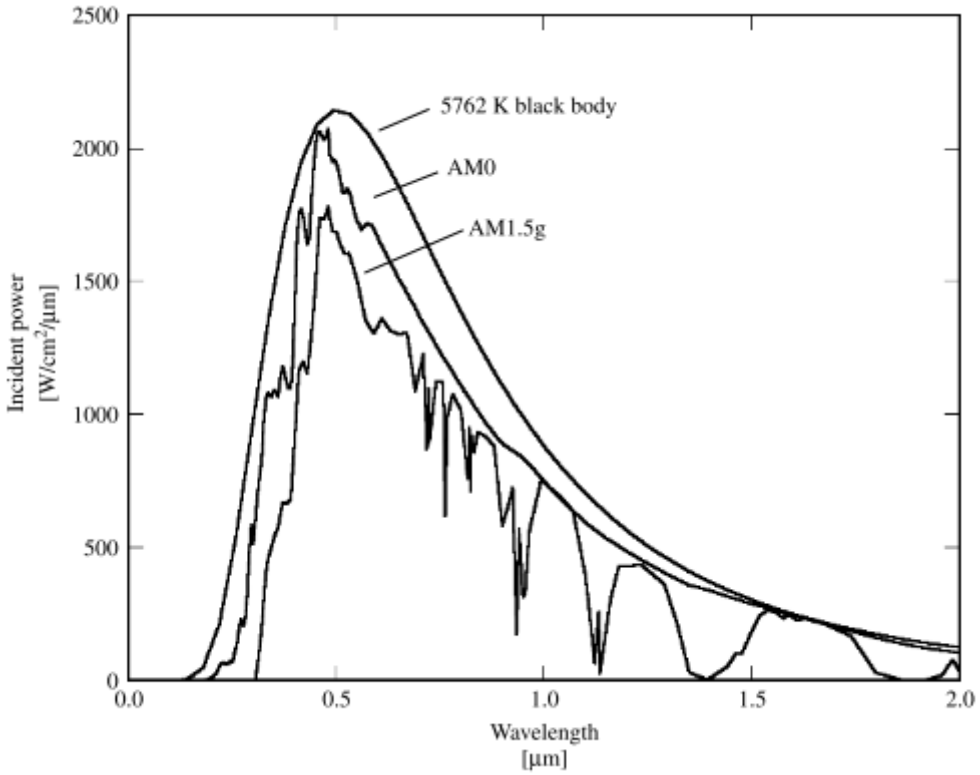

Figure 2.1. Comparison between the global terrestrial spectrum $AM_{1.5;Global}$, the extra-terrestrial spectrum AM_0 and a perfect black body. Image adapted from [4].

The spectral region interval of 0,15-4 μm cover more than 99% of the energy flux from the Sun and nearly half of the total amount is in between the visible light region of the spectrum (0.4-0.7 μm). The Figure 2.2.a shows the visible light wavelength interval where the integrated energy flux is higher as well as the infrared and ultraviolet regions. In solar cells instead of wavelength is commonly used the bandgap energy intervals to specify in which region of the spectrum a certain type of material can absorb a photon. The energy (E) is equal to the product between the Planck's constant (h) and the speed of light (c), divided by the wavelength (λ):

$$E = \frac{h \cdot c}{\lambda} \tag{2.1}$$

Where h = 6.626x10^{-34} J.s; c = 2.998x10^{8} m/s; E is in Joules (J) but can be converted to electron-volt (eV) according to the relation 1 eV = 1602x10^{-19} J, being able to get the values for the bandgap energy (E_g).

Observing Equation 2.1 is possible to conclude that the bandgap energy and the wavelength have an inversely proportional relationship:

$$E_g \propto \frac{1}{\lambda} \tag{2.2}$$

Presenting the same data from Figure 2.2.a but converting the wavelength values to bandgap energy values the spectrum regions will be completely reversed (Figure 2.2.b).

a)

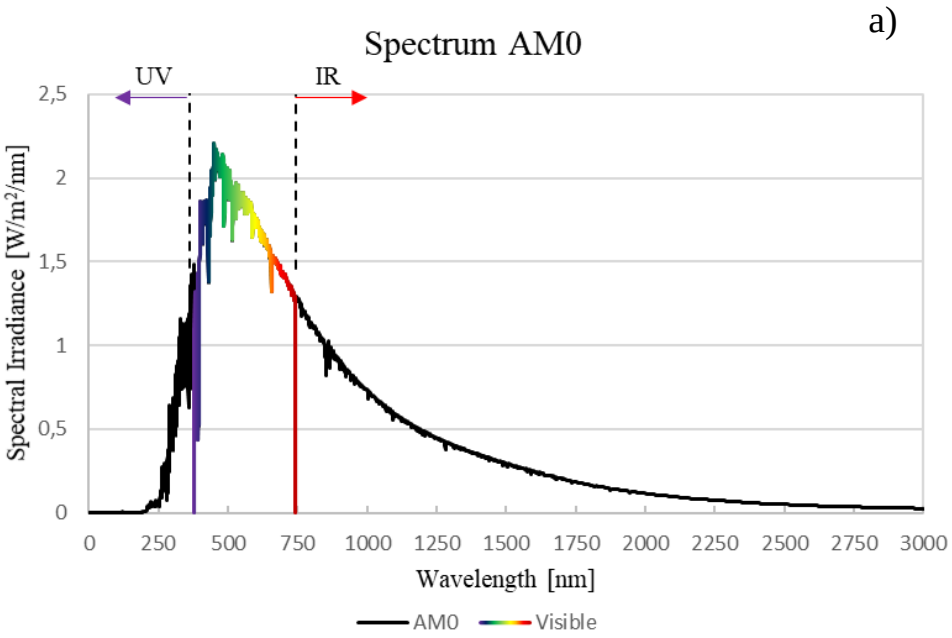

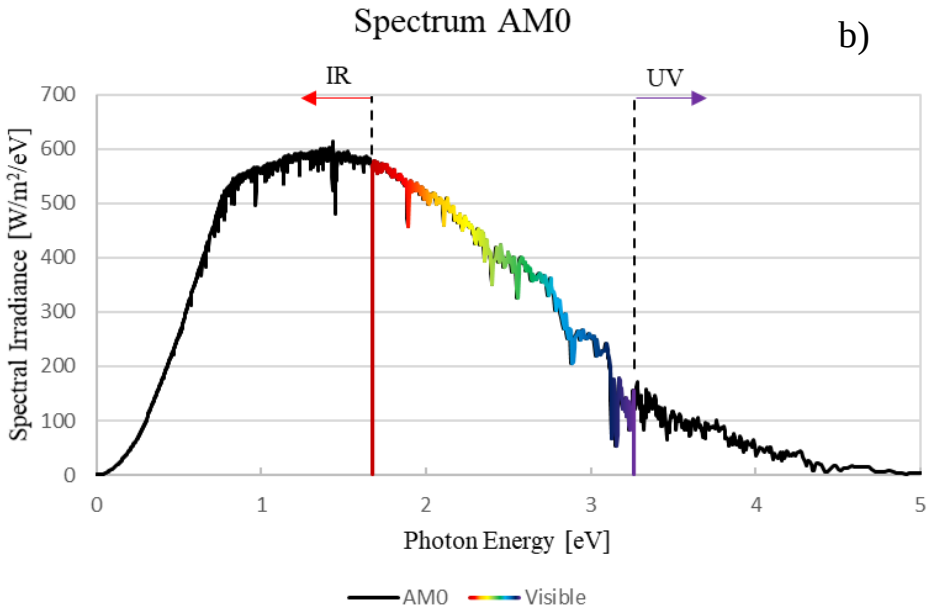

Figure 2.2. a) Representation of *AM0* spectrum, relating the amount of solar irradiance for each wavelength and limiting the visible light region within the spectrum. b) Representation of *AM0* spectrum, relating the amount of solar irradiance for each photon energy, and limiting the visible light region within the spectrum. *AM0* data from [8].

Since the main characteristic associated with different types of materials used in solar cells and its photon absorbance region, is the bandgap energy measured in *eV*. The Figure 2.2.a can demonstrate some energy intervals related to higher input irradiance on the top of PV modules. One of the main reasons that Silicon is the most used material is because it has a bandgap equals to 1.12 eV, being able to perform with high light conversion efficiency in the infrared region of the spectrum, where the spectral irradiance has maximum values.

2.2. Solar Cell Operating Principle

The scientist Edmond Becquerel found out, in 1839, that it was possible to generate electrical energy directly from solar radiation. The photoelectric effect is when a material, commonly metallic, is exposed to a high frequency radiation source and absorbs the incident photons, leading to its electrical charges (electrons and ions) being excited and consequently ejected as shown in Figure 2.3. There is a similar phenomenon with the same principle whose only difference is in the fate of the excited charge carrier. Instead of being ejected, the electrical charges get excited, separates from the atoms, and remain within the material, creating a potential difference and a direct current on the system. This phenomenon is the basic principle behind solar cells technology operation, known as the photovoltaic effect (Figure 2.4). Edmond Becquerel while watching this principle and using metal electrodes and electrolytes, discovered that conductance is directly proportional to incident lighting [7].

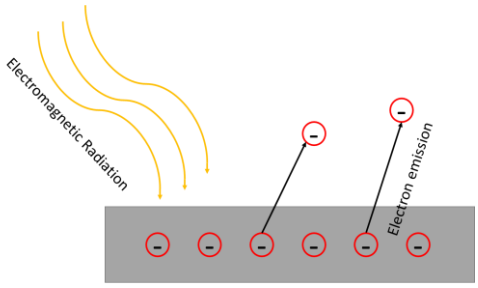

Figure 2.3. The photoelectric effect.

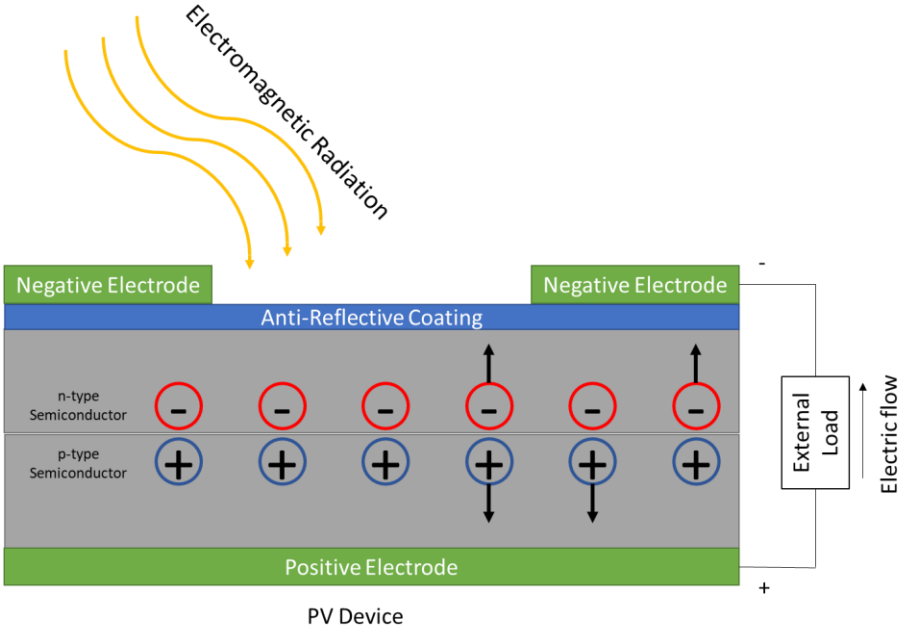

Figure 2.4. Example of a basic PV device model and the respective photovoltaic effect.

Knowing the basic phenomenon behind a solar cell, it now important to comprehend its electronic behaviour. To understand it is helpful to design an equivalent electrical circuit with basic electrical components. The main model of an ideal solar cell can be represented by diode in parallel with a current source, Figure 1.3.

The solar radiation, *G*, will hit the Photo Current Source (PhCS), and generate a photo current, I_{ph}. This current is separated by the diode current, and the actual current produced by the solar cell, I_D and I_s respectively [**9**][**10**].

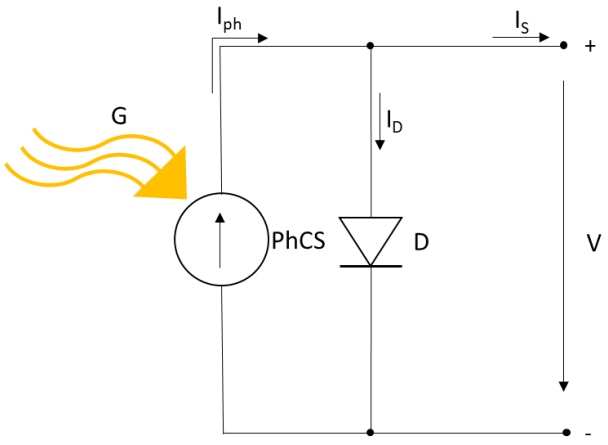

Figure 2.5. Ideal solar cell circuit with a single diode.

Since no solar cell is practically ideal, the circuit must contain a shunt resistance, R_{sh}, and a series resistance, R_s, to represent the parasite losses [**11**]. This procedure will result in a more realistic approach on the actual cell efficiency (Figure 2.6).

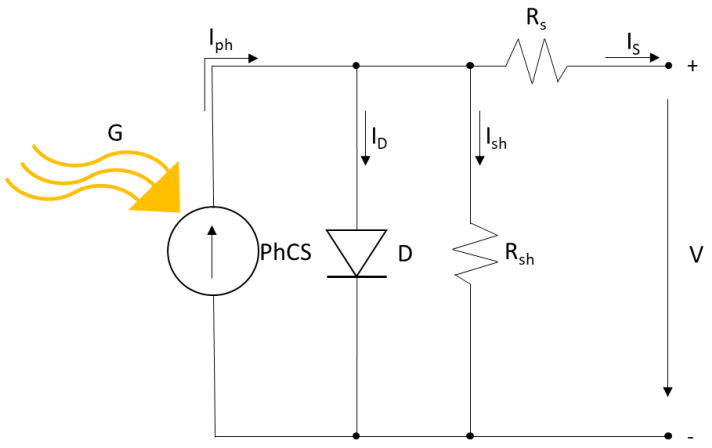

Figure 2.6. Single-diode *PV* model cell with shunt and series resistance.

Following the circuit from Figure 2.6 and applying Kirchhoff's nodal law, which rules that the sum of all the currents leaving and moving towards a node is equal to zero. The total current produced by the solar cell is equal to the photo current produced minus the diode current and the shunt current, as the Equation 2.3 shows:

$$I_s = I_{ph} - I_D - I_{sh} \tag{2.3}$$

The entire current throughout the electrical components is ruled by Kirchhoff's mesh law, stating that the sum of every potential difference points in a closed mesh is equal to zero. The potential difference between both diode and shunt resistance, V_x, is equal to the sum of the voltage across the

terminals of the PV model cell, *V*, and the voltage difference dropped on the series resistance, demonstrated by Equation 2.4:

$$V_x = V + R_s I_s \tag{2.4}$$

Using the Shockley-Queisser, equation that represents the behaviour of a diode and its current lost due recombination we get [**12**]:

$$I_D = I_0 \left\{ e^{\left(\frac{V_x}{nV_T}\right)} - 1 \right\} \tag{2.5}$$

Where the *n* is the diode ideality factor, I_0 is the diode reverse saturation current, and V_T is the thermal voltage given by Equation 2.6 [**11**]:

$$V_T = \frac{kT_0}{q} \tag{2.6}$$

Where *k* is Boltzmann's constant, 8,61x10^{-5} [eV/K], T_0 is the cell temperature and q is the electron. charge.
For the shunt current we can calculate by:

$$I_{sh} = \frac{V_x}{R_{sh}} \tag{2.7}$$

And combining the equations and replacing the parameters into Equation 2.3 results in the complete governing equation for a PV single-diode model:

$$I_s = I_{ph} - I_0 \left\{ e^{\left(\frac{V+R_s I_s}{nV_T}\right)} - 1 \right\} - \frac{V + R_s I_s}{R_{sh}} \tag{2.8}$$

The output solar cell power calculated by:

$$P_s = V \left(I_{ph} - I_0 \left\{ e^{\left(\frac{V+R_s I_s}{nV_T}\right)} - 1 \right\} - \frac{V + R_s I_s}{R_{sh}} \right) \tag{2.9}$$

It is important to understand the electrical behaviour of a single diode to comprehend the main characteristics of a solar cell, such as its efficiency (η), Fill Factor (FF) and Maximum Power Point (MPP). The I-V (Current-Voltage) of a solar cell is determined by its voltage under open circuit condition and its current under short circuit condition. Also, the maximum achievable output power is represented by a point in the curve where the voltage and the current are at its optimal operation conditions (Figure 2.7). Using Equation 2.8 and ignoring the I_{sh} (neglecting parasite losses), it is possible to demonstrate the theoretical maxims under the conditions of short circuit and open circuit [**9**][**10**]. For short circuit conditions there is no potential difference, then:

If: $V = 0$; $$I_{sc} = I_s = I_{ph} = I_{ph} - I_0 \{ e^{(0)} - 1 \} - 0 \tag{2.10}$$

When I_{sc} is the short circuit current.

For the open circuit condition there is no current flowing through the cell:

If: $I_s = 0$;

$$V_{oc} = nV_T ln\left(1 + \frac{I_{sc}}{I_0}\right) \tag{2.11}$$

These parameters represent ideal values, although it is practically impossible to obtain them since there is no energy production or no power generated because voltage or current are equal to zero in each individual conditions. Figure 2.7 is typical I-V curve of a photovoltaic cell according to Equation 2.8, representing a single-diode behaviour, the maximum operation power point, and its ideal maxim values (V_{oc} and I_{sc}).

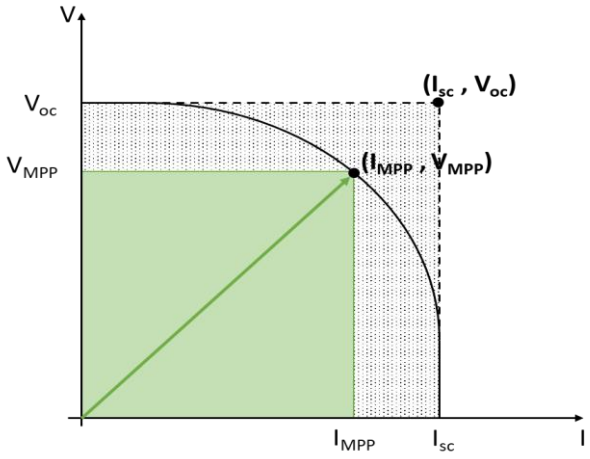

Figure 2.7. Representative solar cell IV curve.

To represent the ratio between the maximum operating conditions and the ideal output power is used a performance concept known as fill factor. Visualizing Figure 2.7, the fill factor is the occupancy ratio of the green square over the dot hatched square. The square's area represents the power output on maximum operation point, P_{MPP}, multiplying I_{MPP} by V_{MPP} (Equation 2.12), and the total ideal power output, P_{ideal}, multiplying I_{sc} by V_{oc} (Equation 2.13) [**7**]. The fill factor, is given by the ratio between both powers expressed in Equation 2.14:

$$P_{MPP} = I_{MPP}\, V_{MPP} \tag{2.12}$$

$$P_{ideal} = I_{sc}\, V_{oc} \tag{2.13}$$

$$FF = \frac{P_{MPP}}{P_{ideal}} = \frac{I_{MPP}\, V_{MPP}}{I_{sc}\, V_{oc}} \tag{2.14}$$

The higher the FF (Fill Factor) value the better its yield, in other words, the closer the I-V curve is to the vertex of the dot hatched square the bigger the efficiency of the solar cell. Then, the efficiency is the electrical output power generated by the cell, divided by incident solar radiation:

$$\eta = FF\frac{I_{sc}\, V_{oc}}{G\, A} = \frac{I_{MPP}\, V_{MPP}}{G\, A} \tag{2.15}$$

Considering an area, *A*, of 1 m^2 solar cell and *G* the incident solar radiation, 1000 W/m^2.

2.3. Solar Cells Materials

The PV solar cells production can be made by a vast number of semiconduction materials. Those resources can be differentiated in organic compounds and inorganic compounds. Organic materials can be used in solar cells and these types are also called plastic solar cells. The main substance used are polymers and results in a very cheap production in a large scale with cells that may present different bandgaps, since polymers can be molecularly engineered with very small environmental harm. On the other hand, is a material that presents low modules and cells efficiencies. With a top value of 15.2% for cell efficiency and a weaker structure (less durability and lower stability) compared to inorganic materials solar cells [**13**]. The inorganic materials advantages that stand out from organic solar make these the most used type holding more than 80% of global PV technology market share in 2016 [**14**]. With a big percentage of the PV technology market belonging to monocrystalline and polycrystalline Silicon, a small number of alternatives may offer different solutions to make the market more competitive. These solutions must present some sort of advantage to overcome the benefit of Silicon's efficiency. Developing technological alternatives resorting on materials with a lower raw extraction cost, with electricity production potential, without any secondary harmful impact over the environment and non-toxic, are considered below.

2.3.1 Silicon

The most common semiconductor material used in the fabrication of solar cells is Silicon (Si) and it can have distinct types of crystallinities. It is considered three types, amorphous, multicrystalline, and monocrystalline, each type presenting different production costs and efficiencies. Monocrystalline silicon presents a solid four-bonded tetrahedral structure and unbroken crystal lattice with an array of molecular connections each oriented the same way. This type delivers a higher efficiency but with a bigger cost. Multicrystalline silicon is formed by small crystals through the Siemens process. After this process, it is created a solid material with various small crystals (or grains) connect to each other with varied sizes and orientations. This type of Si compared to monocrystalline has a lower efficiency but is the cheapest of the first-generation solar cells.

Entering the second-generation solar cells, we have the amorphous silicon which is commonly used for thin films. This type has no molecular connection order, presenting a random network. The a-Si can be deposited by some techniques such as chemical vapor deposition (CVD) or plasma enhanced chemical vapor deposition (PECVD), resulting in a non-crystalline form of Silicon with random connections and dangling bonds, resulting in an anomalous electrical behaviour. To reduce the anomalies, it is common to passivate the a-Si by hydrogen, connecting the hydrogen atoms with dangling bonds, producing hydrogenated amorphous silicon (a-Si:H). It is very cheap and has lower efficiencies than multicrystalline and monocrystalline silicon cells.

2.3.2 CdTe

Cadmium Telluride is a polycrystalline material that have been investigated since the 1950s-1970s. This technology has many options for its processing reaching around 10 different methods, which four of them reached the pre-commercialization stage, spray pyrolysis, electrodeposition, vapor deposition and closed spaced sublimation. CdTe heterojunctions is typically formed by a n-type layer using cadmium sulphide (CdS) and by a p-type layer using CdTe, forming the *p-n* junction by first depositing the CdS layer on a conductive oxide substrate, usually transparent (optimizing optical effects), followed by the CdTe layer using chemical annealing [**4**]. CdTe PV films present a bandgap around 1.5 eV and are slightly p-type with a single junction cell top efficiency of 21%. [**13**] It has low need for water use, small carbon emissions and the quickest energy payback time not only compared to other thin films but of all the other PV technologies [**14**].

2.3.3 CIGS

Copper Indium Gallium Selenide is a material that presents the advantage to be deposited on flexible substrate materials. Given this, it is possible to make devices with high flexibility and very lightweight. Compared to other semiconductor materials, a much thinner film can be produced with a high absorption coefficient. CIGS is composed by copper indium selenide and copper gallium selenide representing the following chemical designation: $CuIn_yGa_{(1-y)}Se_2$. The bandgap of this compound varies according to the *y* value. If *y*=1 the material is pure copper indium selenide and has a bandgap of 1.0 eV (minimum value), if *y*=0 the material is considered pure copper gallium selenide and can achieve a maximum bandgap value of around 1.7 eV [**14**][**15**]. This technology has a reported record of 23.35% for a single junction solar cell without solar concentrator and with Cd-free, eliminating the environmental impact resulted by Cadmium [**13**].

2.3.4 Perovskite

Perovskite was first discovered in 1839 and it's referred as any material with a chemical formula equivalent to the $CaTiO_3$ mineral itself composed by Calcium, Titanium and three atoms of Oxygen. These compounds have a general formula that includes an anion (C) bonded with two cations (A and B) like in the next chemical formula ABC_3. As a solar cell technology, the perovskite material is a metal-halide compound which contains methylammonium Lead (Pb) or Tin (Sn) halide as the active layer for light absorption, with the following chemical formulas as an example, $CH_3NH_3PbY_3$ or $CH_3NH_3SnY_3$, where Y can be Indium, Bromine or Chlorine [**16**]. This technology presents a low material/module processing cost and a vast material abundancy which may permit a low CO_2 emission and with a short energy payback time. Perovskite Solar Cells (PSC) had a rapid power conversion efficiency increase from 2012 with cells achieving less than 10%, to achieving in 2016 a maximum of 22.1%. For future development of PSC's, the disadvantages such as its decomposition when operating under high humidity environment. There are also some issues that need to be resolved or mitigated, such as medium or large scalable and reproducible processes, increase the cell stability, enhance operative lifetime, and mitigate the cell toxicity associated [**17**]. PSC's technology has great adaptability since its bandgap varies depending on halide content (around 1.6 to 2.3 eV) to optimize the cell's needs. It has a high radiation absorption yield in the visible region of the solar spectrum. The reported record for a single junction PSC is 21.6% [**13**].

2.3.5 Solar Cell devices and limitations

In 1961, Shockley-Queisser experiments established a detailed balance limit value, which is the maximum theoretical efficiency for a PV cell based on a *p-n* junction, of 30% for a bandgap energy, E_g, of 1.1 eV [**12**]. For a bandgap energy values between 1.3 *eV* and 1.4 *eV* it is possible to reach a better efficiency. Considering radiative losses from the front and the rear side of PV cell, the maximum efficiency value could be 33.16%, if somehow is possible to include a perfect reflector on the rear side of the PV cell the radiation lost on its base would be neglected and the value would increase to 33.77%, for a bandgap energy of 1.34 eV [**18**]. New updates on the limit were again published by Kerr et al [**20**] presenting a maximum value of 29.05%, for a 90 μm solar cell thickness made of a high resistivity Silicon at 298 K, and by Richter et al [**21**] demonstrating a higher value of 29.43%, limited by Auger recombination and without photon recycling, for a 110 μm solar cell thickness made of undoped Silicon.

2.4. Silicon-based Solar Cells

In solar cells architecture there are three main types of different cell stacking, varying on its degree of simplicity and on the layers of one or more types of material. To identify the different types of solar cells it is used three terms known as homojunction, heterojunction and tandem solar cells.

2.4.1 Homojunction Solar Cells

This type of solar cell is the most simple, cheap and common architecture today. The structure is formed by two layers of the same material and crystallinity, each one having different types of doping enabling the creation of a p-n junction. Homojunction silicon solar cells represented 90% of world market in PV cells in 2018 [**22**]. Nowadays, it still represents a huge percentage on PV market share with energy conversion efficiencies above 20% [**13**].

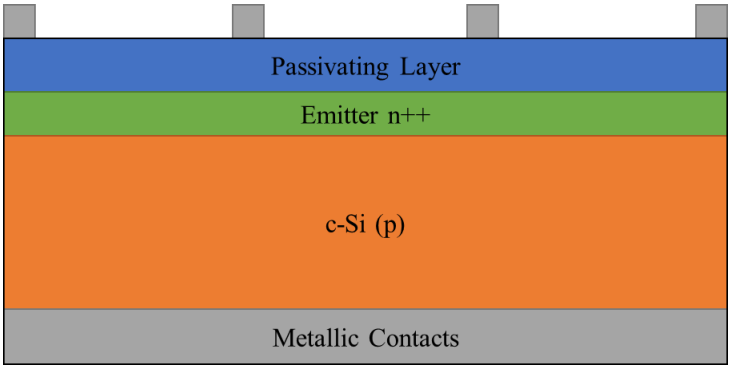

Figure 2.8. Example of a Si-based homojuction solar cell.

Figure 2.3 shows a type of homojunction solar cell, where is used silicon as a material. The p-n junction is created between a heavily doped n-type emitter and a doped p-type crystalline silicon or as studied for this dissertation, a heavily doped p-type emitter and a doped p-type crystalline silicon, that can be monocrystalline or multicrystalline. A passivating layer is also used to mitigate the surface premature recombination.

2.4.2 Heterojunction Solar cells

This solar cell architecture uses the same material in different layers with different crystallinity and the doping type, while using crystalline silicon as the base wafer. Silicon based heterojunction solar cell presents an advantage over homojunction solar cells, using a structure a-Si:H /*c-Si*, where the crystalline silicon wafer is in between layers of amorphous silicon enabling a higher V_{OC} throughout the cell, due to the high amorphous silicon passivation. The only issue, excluding the higher cost, is the parasite absorption on the *c-Si* layer terminals, due to the abrupt change in the lattice from amorphous silicon to crystalline silicon, reducing the power efficiency of the entire cell. Industrially, this architecture presents a viable high-efficiency solar cells presenting an efficiency around 20% [**23**].

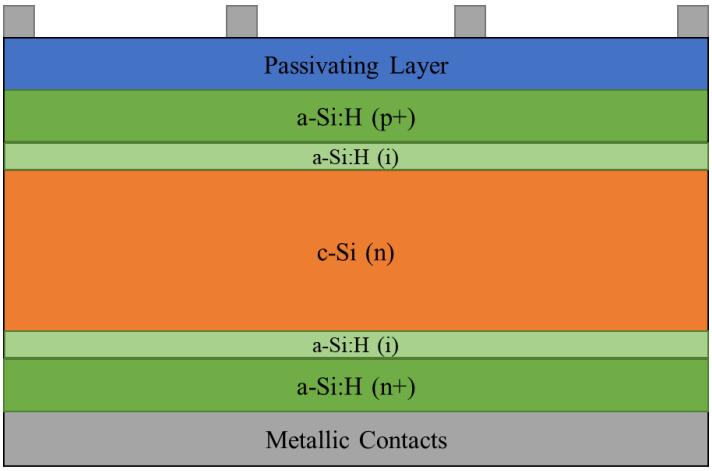

Figure 2.9. Example of a Si-based heterojunction solar cell.

Figure 2.9 shows a simplified schematic of a silicon heterojunction cell, where a passivating layer is used above the p-doped emitter, a-Si:H *(p+)*, for an example a *Transparent Conductive Oxide* (*TCO*), which is a transparent contact enabling a high penetration of photons while maintaining the connection with the external device for the electron flux. Both a-Si:H *(i)* thin films act as passivating layers to mitigate the parasitic losses and maintain the high open-circuit voltage at the terminals of the n-type crystalline silicon, *c-Si* (n). The n-doped hydrogenated amorphous silicon, a-Si:H *(n+)*, act as a Back Surface Field (BSF) which prevents minority carries (electrons) from recombining at the rear metallic contacts [**23**].

There is another type of heterojunction solar cell with interdigitated back contacts where instead of having a frontal electrode as front metallic contacts, they are placed in the rear contacts connected to a layer of interdigitated n-doped and p-doped material in an alternated array. This architecture mitigates the shadowing and increasing the photon penetration on the cell surface. Interdigitated back contacts can be implemented on homojunctions cells but usually is used on heterojunctions and have a higher cost associated but reaching higher efficiencies like 27.41% for an IBC-SHJ (Interdigitated Back Contacts – Silicon Heterojunction) solar cell [**24**].

2.4.3 Perovskite on Silicon Tandem Solar Cells

A multijunction or a tandem solar cell is the stacking of two or more subcells, usually from different types of materials. Tandem cells architecture increases the entire solar cell efficiency by resorting on materials with different bandgaps, which enables the absorption of a wider range of the solar spectrum [**25**]. By stacking subcells in order of decreasing bandgap, the incident photons are filtered by each bandgap energy level, making it possible the conversion of each corresponding solar spectrum range, as shown in Figure 2.10.

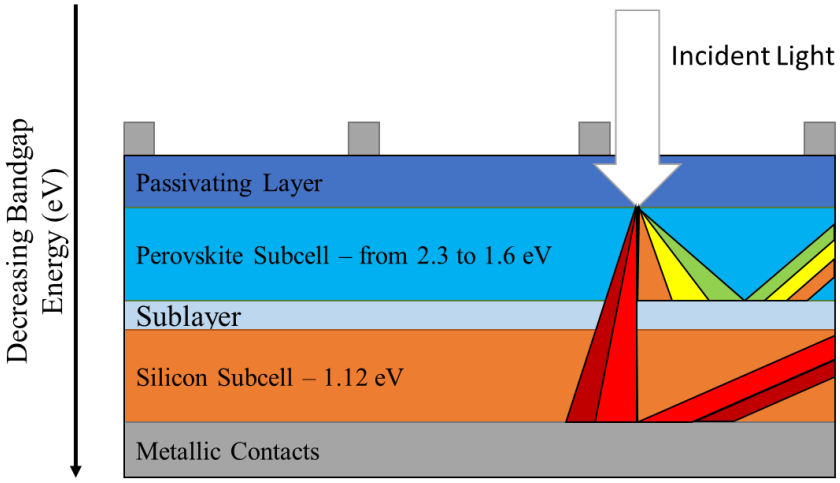

Figure 2.10. Simplified example of a type of tandem solar cell and its behaviour on photon absorption.

Figure 2.10 shows that the entire spectrum is not able to be absorbed by the top subcell because of its bandgap that only corresponds to a maximum between 2.3 *eV* to 1.6 *eV* (perovskite). Part of the incident photons are absorbed at the top subcell while the others, mainly the infrared region, is absorbed only at the silicon subcell.

There are different ways to fabricate tandem solar cells, each one with a different impact on the entire cell's power conversion efficiency. They differ in three main architectures, monolithic architecture relating the two-terminal tandem cells which consists in the electrical bonding between two separate subcells while still enabling the penetration of the photons in the bottom subcell. Mechanical stacking and spectral splitting, while both are associated to four-terminal tandem cells which allows the optimization of every subcell separately [**26**][**28**]. In the monolithic architecture, the top cell is directly fabricated upon a base subcell, separated by a recombination layer. This fabrication method has two terminals, meaning that they are connect in series and have front and back metallic contacts like most of the solar cells (Figure 2.11.a), allowing both subcells to have the same photocurrent if the generated electrons on the top cell can flow to the base cell. If not, the resulting output power is reduced and restricted by the lowest performance subcell. This architecture is the ideal since it's associated with low parasitic absorption losses resulted by the fewer contacts, lower processing and development costs and module solidity [**29**]. The mechanical stacking consists in producing two cells separately and connecting them together after. The spectral splitting relies on an advanced device or a system that can optically separate the solar spectrum in order to direct the correct energy photons to its respective subcell. Both of this fabrication methods use four-terminals architecture, meaning that each individual subcell terminals have metallic contacts, preventing the photocurrent from the top cell to flow to the base cell

(Figure 2.11.b and 2.11.c). Using a four-terminal architecture there is no need to worry about matching top and bottom cell generated photocurrent, although it presents the disadvantages related to parasitic absorptions and optic losses in between the subcells.

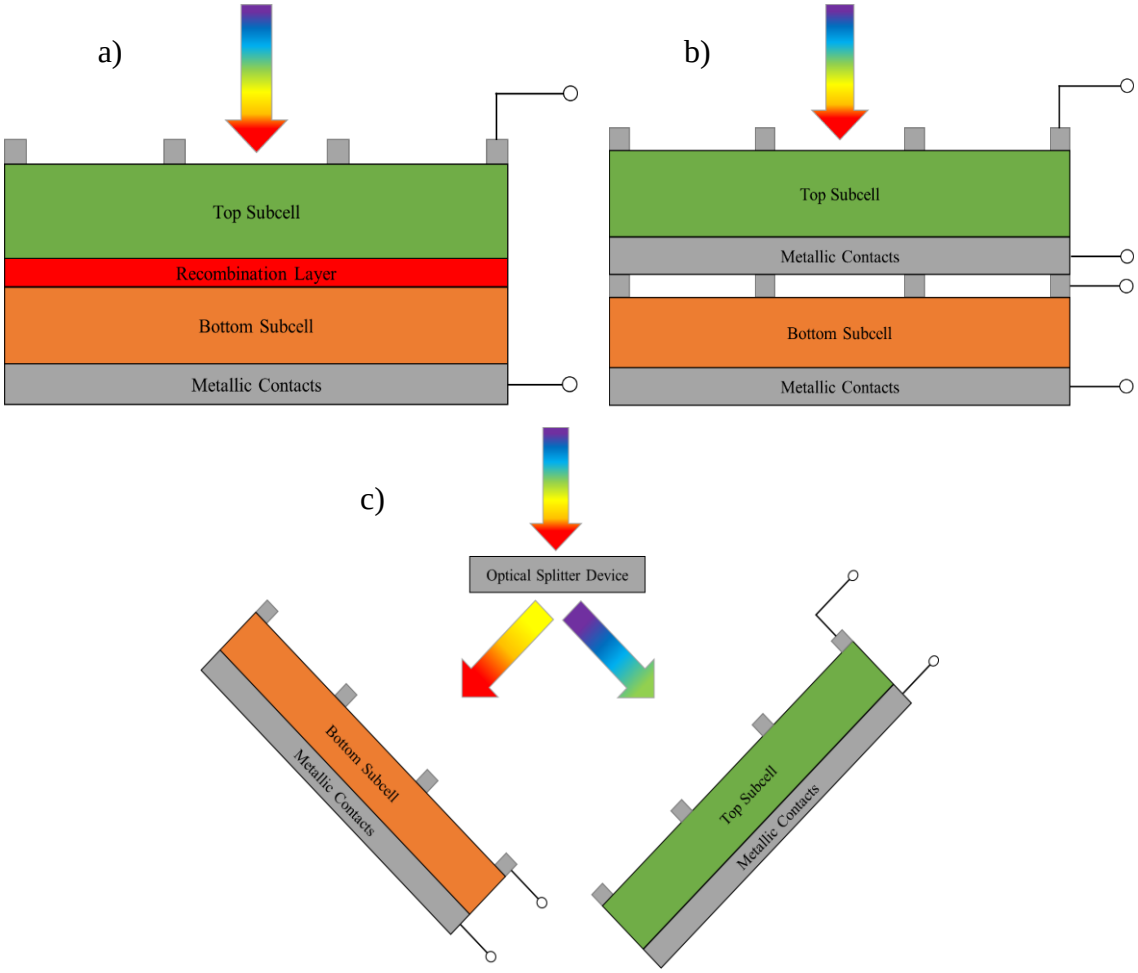

Figure 2.11. Schematic examples of different tandem solar cell architectures. a) Two-terminal monolithic tandem solar cell. b) Four-terminal mechanical stacked tandem solar cell. c) Four-terminal spectral splitting tandem solar cell- Adapted from [30].

Tandem solar cells development is presenting an alternative way to break the efficiency barriers imposed by single-junction solar cells. Using optimal bandgaps for the different stacked solar cells it is possible to reach higher theoretical efficiency limits. For an infinite number of stacked subcells under a sunlight unconcentrated illumination it is possible to achieve a theoretical efficiency limit of 68.2%, even though this option is unviable because as the production costs increase with the increase of the number of subcell. A more realistically situation is using two or three subcells, which under the same conditions, have theoretical maximum efficiencies of around 42% and 49% [**31**].

As referred before, perovskite/silicon tandem solar cells have the potential to become the high-performance solar cells for future applications. Both materials have nearly optimal bandgap energy for a double-junction cell, considering that the optimal bandgap for the top cell is 1.9 eV and for the base cell is 1.0 eV (for unconcentrated sunlight) [**31**]. Silicon, as the base cell, is very close to the ideal value and is considered the optimal bandgap of the solar spectrum (Figure 2.2.b). Perovskite with its great adaptability to vary the bandgap between 1.6 and 2.3 eV, is a good option as the top cell. Both of this subcells present high efficiency values (Table 2-1), when operating as separated single junctions. Latest developments led a two-terminal perovskite/silicon tandem solar cell with record efficiency of 29.2%, under $AM_{1.5;Global}$ [**13**]. This value may be further increased since the maximum theoretical efficiency for this structure is 35% [**32**].

2.5. Silicon doping

Solar cells are basically a group of semiconductors, that works as diodes, making possible the current to flow in only one way. Semiconductors are in between the conductors and insulators groups.

2.5.1 Fundamentals

Their valence and conduction bands are not in contact and, they do not have a large energy bandgap, enabling the flowing of electrons when they absorb smaller amounts of energy from photons. If the photon energy is higher than the bandgap energy it provokes excitation of electrons, and the extra energy is lost due thermalization. Photons with less energy than the bandgap can't be absorbed. Insulators, such as glass and other non-metals, have very high conductivity resistance. They have such a big energy gap between valence and conduction bands, that is physically almost impossible to electrons absorb the amount of energy needed to jump from the valence band to the conduction band. Conductors, mainly metals, present a high electrical conductivity, since both valence and conduction bands are in contact with each other. Semiconductors are in between the conductors and insulators groups. Figure 2.12 shows the different group of materials, the dashed line represents the Fermi level, which is a hypothetical energy level where an electron has 50% chance to occupy it and the holes represented are nothing more than the absence of electrons.

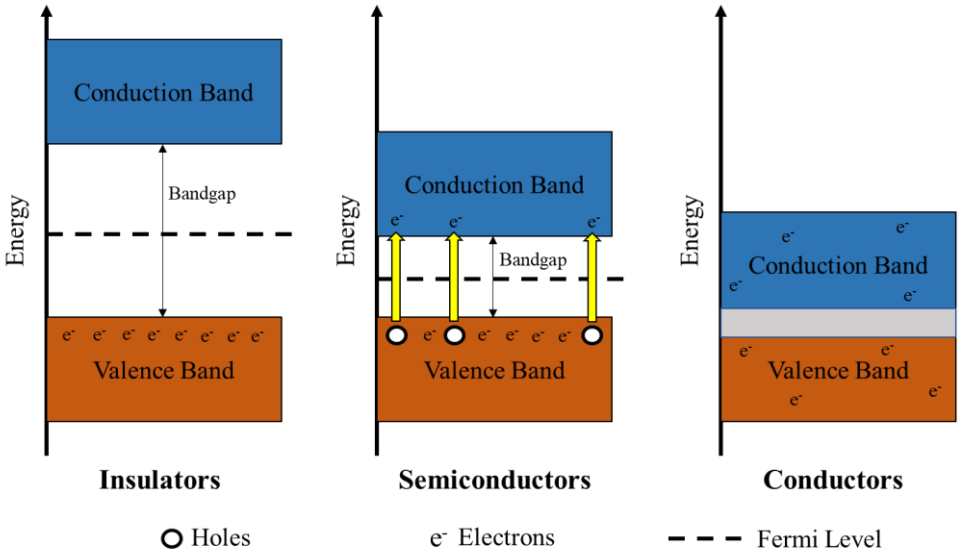

Figure 2.12. Representation of each different group of materials and its band schematic.

Even though semiconductors have less electrical conductivity than conductors, they are considered viable options in solar cells, as it is the case of silicon.

The process of doping is a way which we can increase the conductivity of a semiconductor and, consequentially, increase the efficiency of an entire solar cell. Doping, as a definition, is simply the addition of impurities to a semiconductor, resulting in a mutation of the wafer's atomic structure. In case of the atomic structure of silicon, a single atom has four valence electrons that participate in chemical reactions. Each silicon atom connects with other four by covalent bonds using each valence electron as the link. Doping atoms with three valence electrons such as aluminium or boron, into a silicon wafer, results in only three covalent bonds, leaving one nearby silicon atom unbonded due to the presence of a hole (Figure 2.13). We are now in a presence of a p-type semiconductor that conducts better the electricity than pure silicon, although the charge carriers are holes. In other words, is the movement of holes that is responsible to the conductivity of a p-type semiconductor. When atoms with five valence electrons are used as dopants, like phosphorus atoms, into a silicon wafer, the four covalent bonds with the nearby silicon atoms still exists, with the difference that there is one valence electron unbonded (pointed by a black arrow in Figure 2.13). The extra electron is free of movement in the conduction band, increasing the conductivity of the semiconductor. This is known as a n-type semiconductor and the charge carriers of this type are electrons.

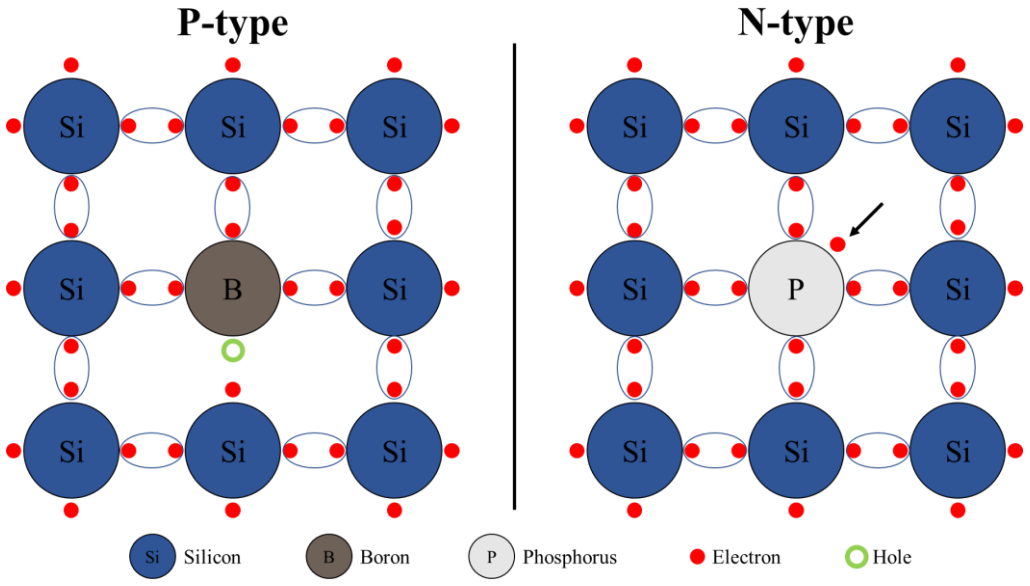

Figure 2.13. Atomic structure of a n-type semiconductor doped with boron atoms connected by only three covalent bonds. And the atomic structure of a p-type semiconductor doped with phosphorus atoms leaving the extra electron unbonded (pointed by arrow).

By connecting both types of semiconductors into each other there is an electrical tendency of the extra valence electrons on the n-type semiconductor to drift and fill the holes that are present on p-type semiconductor. The interface boundary between both silicon types is a p-n junction. In the course of time, the left side of the p-n junction will accumulate a big number of negative charges that came from n-type semiconductor, and positive charges on the right side since its now electron deficient due to the flow to p-type semiconductor. There is an electric field created at the p-n junction also there are new and leftover electrons on the n-doped area that still want to fill the holes at the p-doped area, creating a force to accelerate electrons (F_e). On the other hand, the negative charges at the depletion region, repel the new electron that come from the n-type semiconductor, creating a counter repelling force (F_R) against F_e. When both forces reach the state of equilibrium there is no more electron flux and result in a constant junction potential, being the basis behaviour of a solar cell.

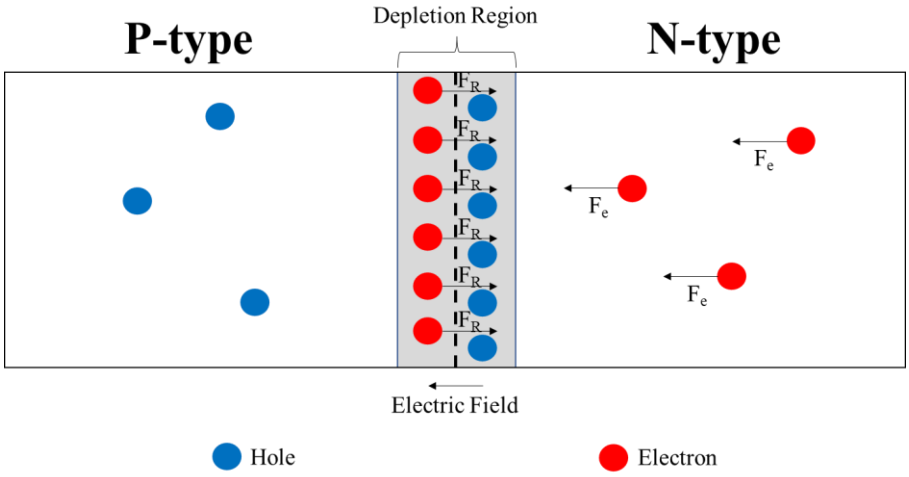

Figure 2.14. Example of a p-n junction behaviour.

In terms of electron excitement, depending on the semiconductor's doping type, there are different behaviours at the Fermi level. The Fermi level will have its location according to the dopant type. For the p-doped, the Fermi level tends to approximate the valence band. When the dopant is n-type, the Fermi level approach the conduction band. This will leave the p-n junction region with a small gap between the valence band at p-type semiconductor and the conduction band at n-type semiconductor (Figure 2.15), resulting in an easier flow of electrons from valence to conduction band of each semiconductor via photon energy absorption.

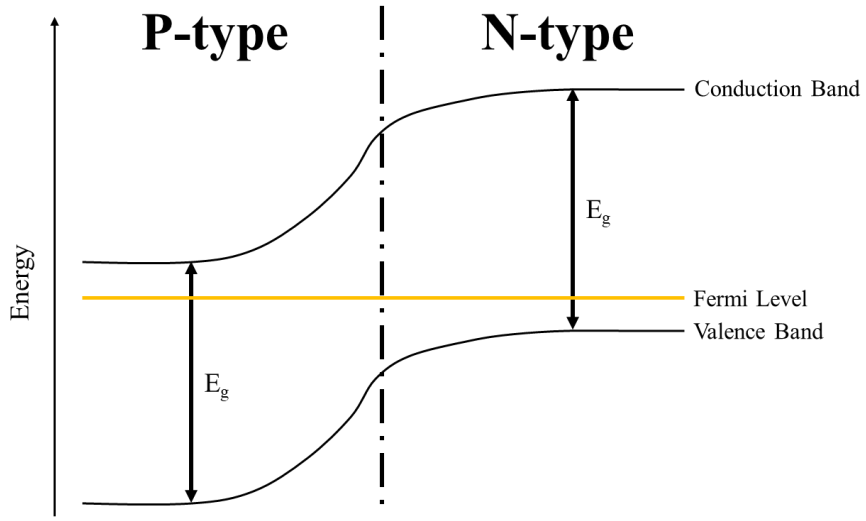

Figure 2.15. Band diagram at the p-n junction with both semiconductors separated with a dot-dashed line. The Fermi level represented with a yellow line.

2.5.2 Gas Immersion Laser Doping (GILD)

This technique relies on a laser as the heating source and a precursor gas as the dopant. Before the doping process a selection of wafers and its pre-treatment is usually performed. Monocrystalline Si wafers with ⟨100⟩ oriented crystallographic structure is the most viable for this process rather than ⟨110⟩ and ⟨111⟩, since it yields higher carrier mobility in PV solar cells due to its improved light trapping characteristic [**35**]. The wafer doping profile can vary according to the wanted layer formation (n^+/p or p^+/n). The pre-treatment performed consist in plunging the wafer into a solution of HF to remove the oxides at the surface, followed by a deionized water swilling [**36**]. After, the sample is placed inside a controlled atmosphere, which is purged with an inert gas to remove atmospheric gases, the dopant gas insertion is started. The low-pressure chamber is sealed with the desired amount of dopant concentration and the pulsed laser starts heating the sample, thought a window, at the desired location controlled by the wafer holder that can moved in two dimensions (x-y stage). The pulsed laser beams start melting the silicon surface and following with solidification in very narrow time intervals. The dopant gas will penetrate in depth the molten silicon and stays confined inside the sample when the solidification occurs (Figure 2.16 on the right) [**36**][**37**][**38**].

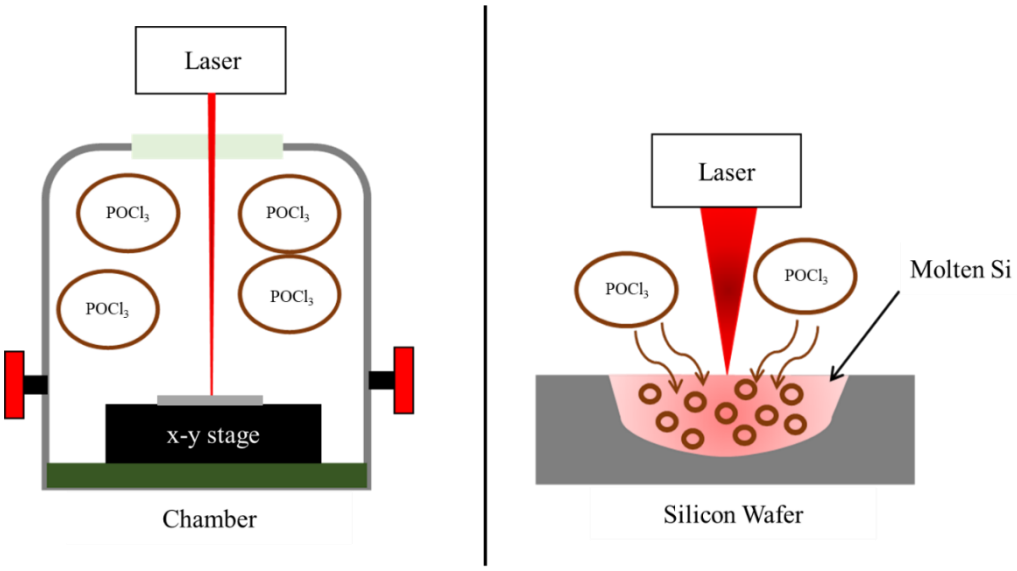

Figure 2.16. On the left is represented a silicon wafer (in grey) inside a controlled atmosphere with p-type dopant gas. On the right is the molten process induced by the laser and the penetration of the dopants in depth.

The dopant atoms that are commonly used in this technique are boron for a p-type wafer resorting on gas sources like BF_3, B_2H_6 or BCl_3, and phosphorus for a n-type using PCl_3 or $POCl_3$ as source [**39**]. The active dopants concentration composition and the depth of the doped layer on the sample is affected by the laser characteristics and surface treatment variables, like the power density, number of laser pulses, surface irradiation time and the saturated gas dopant concentration [**36**][**38**].

2.5.3 Laser Interaction with Silicon and Doping

The morphology and the homogeneity of the scanned silicon sample can vary according to pre-defined laser parameters. Testing variables such as laser's energy density, number of pulses per sample region (0,5 cm^2), laser pulse width, melting time, also setup variations like the chamber leakage rate according to its initial pressure, and window type, represent an analysis that influences the melting depth and the dopant concentration. Some studies have been made to measure the variation of some variables. Using a 1-dimensional simulation using a software called *LASERMELT*, it is possible to input constant values associated with silicon, like melting temperature, latent heat of melting, thermal capacity, thermal conductivity, reflectivity, absorption coefficient, among other of interest [35][36]. And different laser parameters, in order to get results that correspond to a sample post-laser treated and the correlation between the doping properties as an output. The main laser parameters that affect the melt depth are the laser's energy density and the period that the surface of the wafer is under the influence of the laser irradiation. The melt time and the melting depth are related in a direct function, if the sample is exposed to a laser beam for a longer period, it will receive a bigger energy flux from a given energy density. The data in Figure 2.17 is from two different works, but correspond to related works testifying it via LASERMELT, both using excimer lasers (XeCl – 308 nm wavelength) differing on the FWHM (Full Width at Half Maxium) temporal pulse, Figure 2.17.a with a 27.5 ns pulsed beam and Figure 2.17.b with 37 ns pulsed beam.

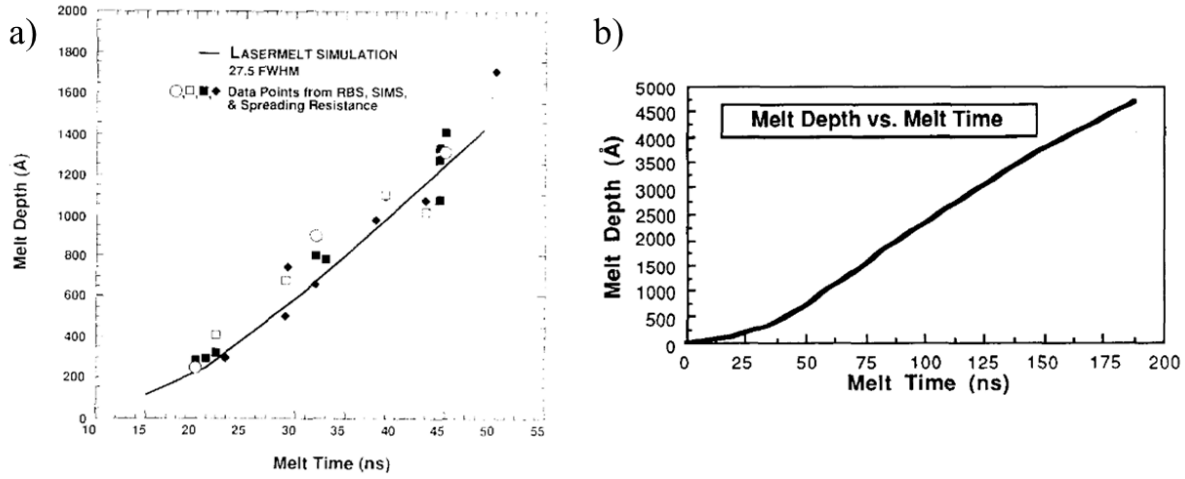

Figure 2.17. a) LASERMELT simulation and experimental data for silicon showing the melting depth variation for different melt time. From [35]. b) LASERMELT simulation showing how a longer melt time affect the melt depth. From [40].

Visualizing Figure 2.17.a, we can observe that in both works the melt time is associated with each consecutive pulse and with the melting depth. This relation is limited by the respective laser's energy density as the next group of images can confirm. The data on Figure 2.18 represent the relation between the energy fluence received by the sample and the melt depth, from respective works as in Figure 2.14. The minimum energy needed for silicon to melt is 0.6 J/cm^2, then the simulation starts at 0.65 J/cm^2 to overcome the limit. The laser pulse on both plots starts at t=0 but the melting time starts with a delay. For example, in the Figure 2.18.a with a 0.65 J/cm^2 the silicon begins to melt 20 ns after the first laser pulse, while using a pulse energy of 1.0 J/cm^2 the melting starts around 10 ns after the initial laser pulse, reaching a maximum melt depth of 0.14 μm at around *t*=31 ns. For the Figure 2.18.b the deepness is bigger since the energy fluence values are bigger.

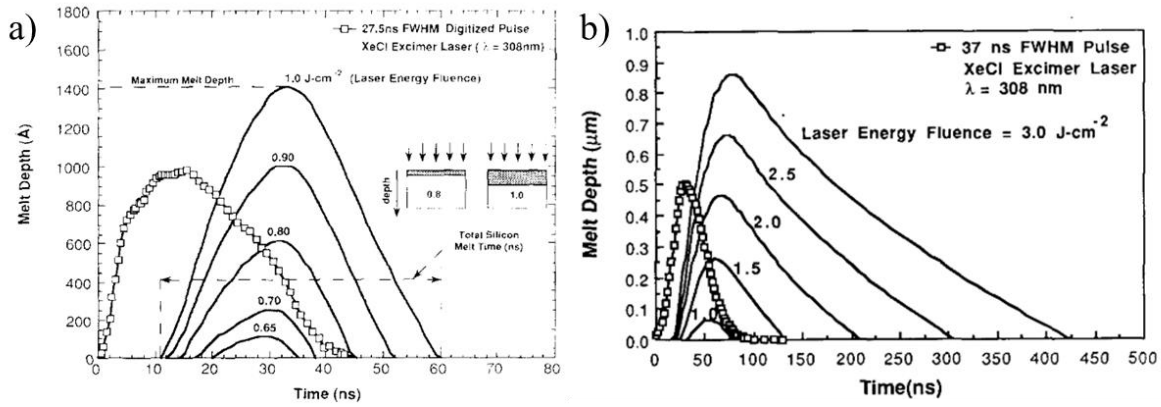

Figure 2.18. LASERMELT simulations from separated but similar works comparing the behaviour between sample's melt depth and melting duration when varying the energy fluence. a) Starting with a laser energy fluence of 0.65 J/cm^2 going to 1.0 J/cm^2 and reaching a maximum depth of 0.14 µm. From [36]. b) Starting with the maximum energy fluence from a a) and going to 3.0 J/cm^2, making possible to reach a maximum melting depth around 0.86 µm. From [40].

With information given by both graphs, it is possible to state that the sample starts to melt faster when the energy fluence is increased. In Figure 2.18.a, with 0.65 J/cm^2 the melting only starts 20 ns after the initial pulse, while with 1 J/cm^2 the time interval shortens, and the melting starts 10 ns after the first laser pulse. Also, both the melt depth and the duration that the sample remains melted lengthens as the energy fluence increases. The melting of silicon has the main objective to allow the penetration of dopant impurities residing in the surrounding controlled atmosphere. The longer the silicon is melted the higher number of dopant atoms are absorbed. However, the concentration distribution is not as homogenous as for a short process of melt/solidification, causing defect formation [**36**].

Other variable that depends on the laser's parameters and is directly accounted to a successful dopant penetration is the sheet resistance. The sample's sheet resistance, when varying energy fluence and when exposing the wafer to a longer period of radiation, consequentially, receiving a higher number of laser pulses, can decrease, causing an improvement in the electrical charge flux travelling across the layer. Analysing the two previous works referred in both last figures, it is possible to confirm the sheet resistance dependence with laser's energy density and number of pulses. In Figure 2.19.a is plotted an experiment, which using an ambient doping of 1% AsH_3, the laser is executed in two different melt times, 22 ns and 43 ns doping, with 1.25×10^{13} atoms/cm^2 and 3.0×10^{13} atoms/cm^2 per pulse, respectively, determined by Hall method. Also, a LASERMELT simulation is compared with both doping pulses. In figure 2.19.b is demonstrated a decrease of the sheet resistance on a B_2H_6 laser doped samples when both laser's energy fluence and number of pulses increase.

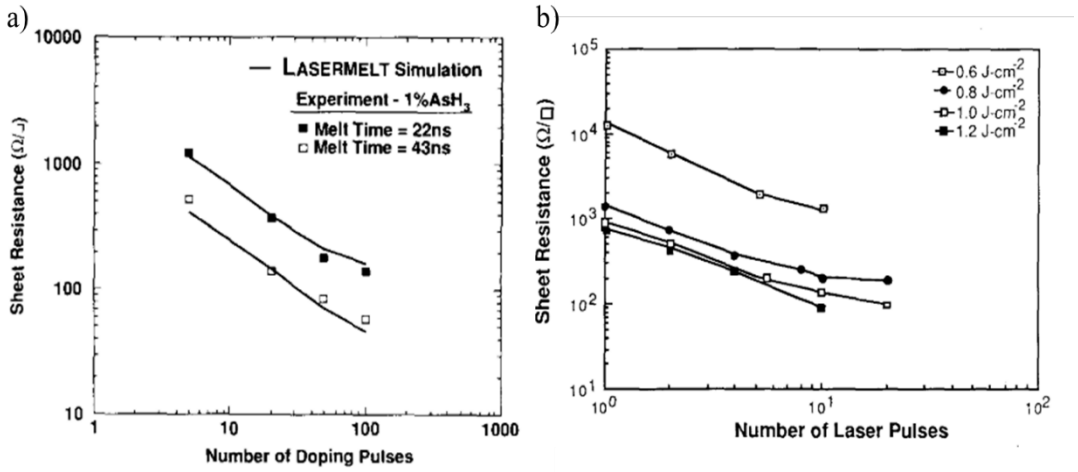

Figure 2.19. a) LASERMELT simulation and Hall method experiment measuring the sheet resistance of a sample with 1.0% A_s H_3 doping, while increasing the number of laser doping pulses. From [36]; b) Sheet resistance measurement of B_2 H_6 laser doped samples while varying both laser's energy fluence and number of pulses. From [40].

The simulations represented in Figure 2.19.a show a very accurate approximation to both experiments. Both works confirm the sheet resistance mitigation with each number of pulses. Also, the greater the energy fluence from the laser, the lower will be the sample's sheet resistance due to a higher dopant incorporation. However, the sheet resistance may find a minimum limit for each energy density associated, since above 200 pulses the mitigation of sheet resistance attenuates. It is even possible, with a right amount of number of laser pulses stimulate a doping process using a lower energy density than the silicon melting threshold [**37**].

For future developments of this dissertation, it is important to understand the relation between the dopant penetration, as well as the layer concentration, as we increase the number of laser pulses. In an experiment where samples are irradiated with three different sequencies of laser pulses and restoration of the dopant gas (BCl_3) in the controlled temperature (10, 50 and 200 pulses), the results demonstrate a deeper concentration of impurities (boron) as well as a higher maximum value of boron atoms that penetrates the layer, as shown in Figure 2.20.

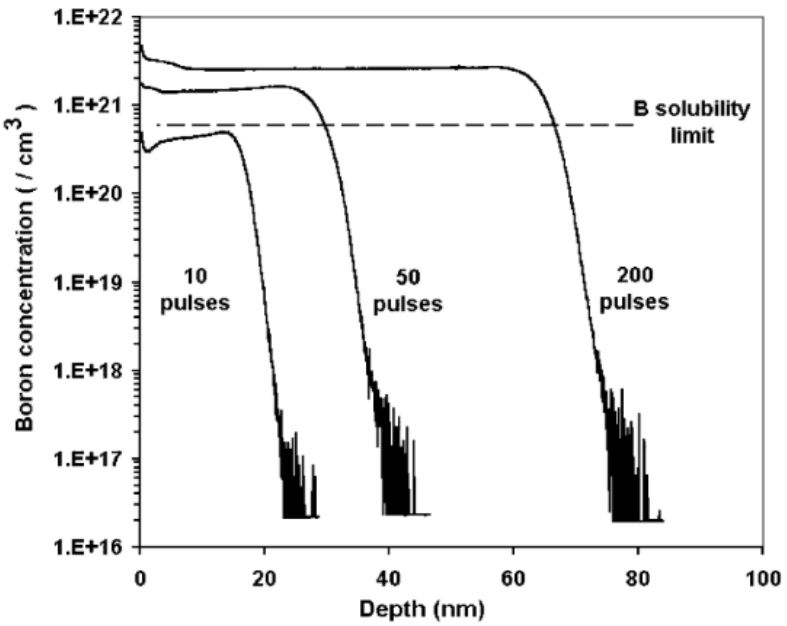

Figure 2.20. SIMS characterization of the in-depth boron-doped samples for different number of laser pulses. The boron solubility value is identified with a dashed line. From [38].

According to Figure 2.20, for 10 pulses is obtained a maximum boron concentration of 0.4×10^{21} cm^{-3}, penetrating as deep as 21 nm. Increasing the number of pulses for 50 pulses, the maximum boron concentration reaches 1.4×10^{21} cm^{-3} and 37 nm of deepness, for 200 pulses, the maximum concentration increases to 3.3×10^{21} cm^{-3} and the dopant penetration reaches 74 nm deep inside the sample [**38**].

2.6. Silicon Tunnel Junctions

For every tandem solar cells, especially silicon based, an important step to an efficient device, is to maximize, throughout the cell manufacturing process, the transport of the charge carries while travelling from one subcell to another. Creating a thin layer between both layers results in the formation of a tunnel junction, a connection where two different conductive materials meet.

2.6.1 Fundamentals

In the process of manufacturing p-n junctions in tandem cells, there is an important factor related to the connection between p-type and n-type layers. It is necessary a very thin sublayer with high optical transmissivity and low electrical resistivity. A tunnel junction, also known as Esaki diode, is a sublayer with a nanometre depth scale, created by the superposition of different heavily doped type layers. The tunnel junction is the interface that connects tandem cells monolithically fabricated in series working as a link passage, with residual losses, in one way direction [**33**][**34**]. When there is no voltage applied, the charge carriers, in this case electrons, cannot drift from the conduction band and fill the holes at valence band, because the electrons do not receive enough energy to be removed from its equilibrium state (Figure 2.21).

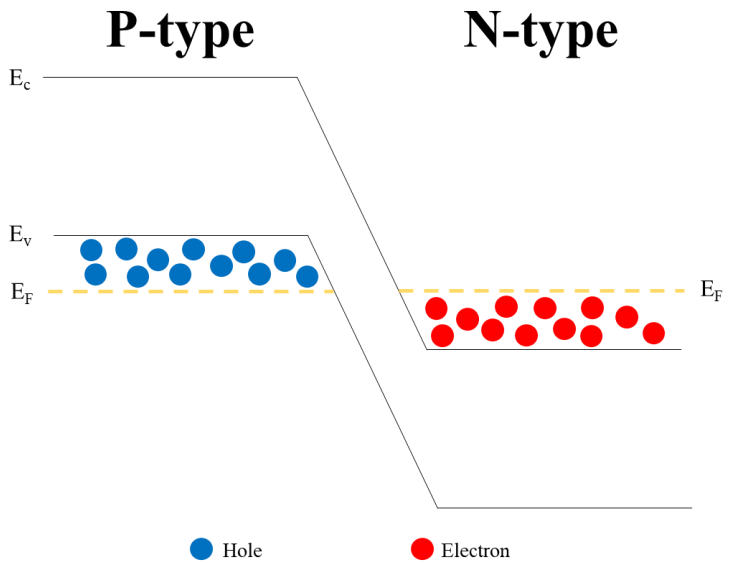

Figure 2.21. Tunnel junction without electric potential applied. E_c is the conduction band, E_v is the valence band and E_F is the Fermi level which is aligned in both doping types.

By having on both p-type and n-type high respective dopant concentrations separated by a depletion layer, creates an electric field. When the certain amount of voltage is applied, occurs the misalignment of the Fermi level resulting in a band diagram disruption. The conduction band on the n-type becomes aligned with the valence band on the p-type, and both remain on the same energy level where is now possible the flow of the current. The alignment of band provides the occurrence of a tunnelling effect. The tunnelling effect occurs when an electron from the n-type conduction band appears on the p-type valence band without any energy variation and ignoring the repellence of the depletion layer, Figure 2.22. This can be explained as a quantum phenomenon, where an electron presents a discontinuous movement, which is a motion based on the probability of a certain particle appear nearby its initial position, making it possible to go through the depletion layer and fill holes without having the need to absorb energy.

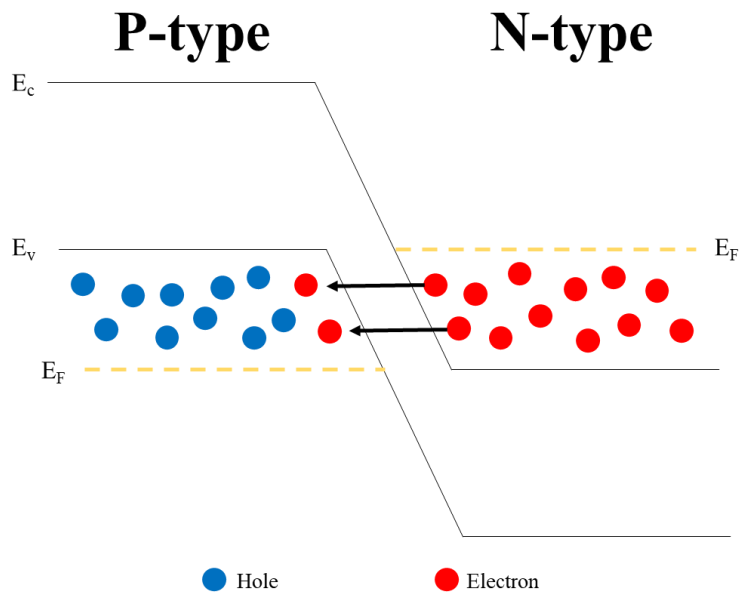

Figure 2.22. The alignment of bands caused by an induced electric potential resulting in a tunnelling effect. E_c is the conduction band, E_v is the valence band and E_F is the Fermi level which is misaligned on both doped areas.

Tunnel junction layers are fabricated as thin as possible to maximize the tunnelling effect and to minimize the parasitic losses.

2.6.2 Fabrication methods

There are many techniques used to develop a tunnel junction, each one with different methodologies and advantages associated. PECVD is a technique which deposits doped silicon thin films on a heterojunction silicon cell. Inside the reactor, the collisions between electrons and the source gas molecules enables the decomposition of the gas into the plasma, which penetrates the wafer. This technique presents a quick deposition rate, the possibility to prevent any damage to the amorphous silicon in the heterojunction cell, a homogeneous film quality while operates under low base temperature values, unlike the predecessor technique CVD (Chemical Vapor Deposition). The cons for PECVD is, mainly, the large investment in reactor and equipment and the dangerous gases and metal dust resulted from the coating process. Proximity Rapid Thermal Diffusion (P-RTD) is another technique used to fabricate tunnel junction, creating an ultra-shallow layer of dopant atoms inside a subcell. A spin-on-dopants layer is placed in between two layers of silicon films while a base and a top heating lamp irradiate heat under a N_2 ambient and at atmospheric pressure. The dopants travel from the top silicon layer to the base silicon layer resulting in an in-depth diffusion through the silicon [**26**]. This technique presents a controlled junction depth as the result.

The GILD technique prevents a big investment in equipment, maintains a controlled and closed environment for the dopant gases and, unlike P-RTD, avoid silicon deformation problems associated with the long heat flux focusing the substrate. The result is a heavily dopant concentrated, and ultra-shallow tunnel junction formed by consecutive laser pulses. These pulses transfer into the wafer a high energy density, creating a melting-solidification loop and enabling the penetration of the dopants that resides in the surrounding atmosphere.

2.6.3 Characterization methods

The main objective of this dissertation is to understand and evaluate the laser treatment interaction with the silicon samples. The characterization of the wafers before the doping process, varying the laser parameters and other variables previously mentioned, will dictate the optimal conditions and parameter values to execute the GILD technique. The laser doping using gaseous dopants enclosures with a silicon base wafer in a controlled atmosphere is the process that we aim to use for the final stages of the S-LoTTuSS project. Once the interaction between laser and silicon is optimized and after the doping is done, the characterization of the doping profiles and, consequentially, the tunnel junction will evaluate the doping effectiveness. Therefore, the characterization will be divided in two stages, the pre-doping, which corresponds to the laser/silicon interaction and the performance of the surface treatment, and the post-doping, corresponding to the doping profiles and the depth penetration of active dopant atoms.

2.6.3.1 Pre-doping studies for laser-silicon interaction

The intended for the doping is to have high dopant concentration values inside an ultra-shallow and homogeneous layer. In order to characterize the surface topographic homogeneity and the results from laser application, two processes denominated as Atomic Force Microscopy (AFM) and Scanning Electron Microscopy (SEM) can be used. AFM is a technique that uses a support with a mechanical nib at the end, like a low scale needle, which is in constant contact with the surface of the sample. It moves over the entire sample surface with the nib operating under successive touches with a pre-defined frequency. The support reflects a laser radiation to a photodiode which reads the position of the support according to the position of the nib when it touches the surface, charting the roughness of the sample. The result is a nanometre two or three-dimensional scale topographic image showing the irregularities on the surface of the sample. SEM is a technique that requires a primary electron beam source and an electron detector at the end. This method uses an electron beam, which is focused with the help of an electromagnetic refractor, that will strike the surface of the sample, generating the emission of secondary electron from the surface. These secondary electrons are filtered and detected by the detection system. The numbers and the position of emitted electron correlate the surface topographical variations of the sample.

2.6.3.2 Post-doping characterization

The detailed analysis of the sample after the GILD process, is the final characterization which results in the evaluation of the doping depth profile and its homogeneity. Secondary Ion Mass Spectroscopy (SIMS) is a surface microanalytical technique used on solid surfaces and thin films. The basic principle leans on the sputtering phenomenon, which a surface-directed energetic ion beam reaches the sample, resulting in the bombardment of the affected area and the constant ejection of microscopic particles from the sample. Resorting on a vacuum and analysing system the ejected particles, also called secondary ions, are collected and separated by mass, making possible to represent the amount and variety of substances incorporated by the wafer. SIMS has a particularity which is a disposable wafer analysis. Since the sputtering destroys a sample by creating craters it is not possible to fulfil more experiments with the same specimen. Another technique that has this disadvantage but is a cheaper and potentially viable to be built in the laboratory is the Electrochemical Capacitance Voltage (ECV).

The capacitance-voltage technique, or C-V profiling, is the base for the ECV, which uses a metal-semiconductor junction for measurements (Schottky barrier), while the ECV uses a semiconductor-electrolyte junction [**41**]. For the conventional C-V profiling, the principle is monitoring the Schottky barrier capacitance of the sample while is applied a certain voltage value. The improved technique, ECV, alternate the C-V measurements and uses the electrochemical etching to register the free charge carriers' concentrations in-depth. Like SIMS, the ECV technique when is executed the sample analysed is destroyed. Although, this technique is cheaper to assemble the required equipment in the laboratory.

3. Methodology

In this chapter, it will be described the experimental process, starting in the preparation of the atmosphere inside the chamber and finishing in the analysis of the processed samples using the microscope. Also, it will be presented the equipment used for the experiment, such as the laser, the chambers, the properties of used samples, the selection method for the sample's post-characterization techniques. It's going to be explained.

3.1. Setup details

The main equipment used to study the silicon behaviour under high energy density irradiation was the laser, as the source of power, and the chamber, to simulate a controlled atmosphere. The apparatus mentioned will be detailed described in the following subchapters.

3.1.1 Chambers

In parallel with the study of how different laser variables affect the quality of the scan, and, consequentially, the doping effectiveness, a consideration and evaluation of the chamber which confines the sample in a controlled atmosphere is also relevant. There are two different cylindrical chambers available at the laboratory that are viable for the experiments. One of the chambers, for now on referred as "old chamber" is represented as the left scheme on Figure 3.1. The old chamber's base has an external diameter of 16.0 cm, and the inside diameter is 13.0 cm, surrounded by 7.5 cm of height walls with 3.0 cm of thickness, made entirely of aluminium. It has one gas inlet and one outlet controlled by a one-way valve each. There are two types of lids available, one of them is an infrared transparent window made of quartz of optical quality at the centre of an aluminium frame, having a lower visibility to the interior. With an area around 53.8 cm^2, it has the minimum area necessary to perform the laser scan experiments without opening the hatch and adjusting the sample (centre scheme on Figure 3.1).

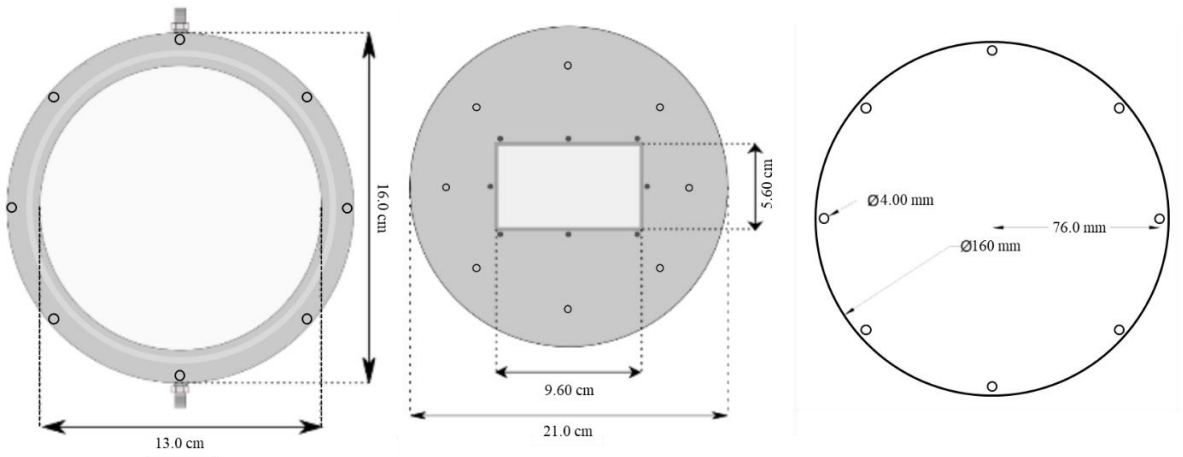

Figure 3.1. Top view representation of the old chamber such as the two lid options. On the left the chamber, on the centre the lid with the quartz as the infrared transparent window, and on the right the polycarbonate window.

The other lid has 100% visibility to the bottom of the chamber, and it's made entirely of polycarbonate which permits the usage of screws on the window to close the hatch since it does not crack as easy as quartz (right scheme on Figure 3.1). It has a frame to insert an o-ring on the back side of the central image in Figure 3.1, providing more sealing power.

The equidistant circular array of eight holes, represented on the Figure 3.1, have positions that correspond to each other which is where the screws are tightened. The circle represented in light grey on the chamber scheme, is a pit where an O-ring is used to avoid leakage from inside gas and potential contaminations from the outside atmosphere. The eight holes represented in the middle scheme, closer to the rectangle where the quartz is placed, is where the sealing of the window takes place. This chamber has the capability of enabling a fluid circulation throughout the experiments, that not being necessary, there is no need to be represented.

The other chamber, for now on being referred as "new chamber", was recently designed and developed at the laboratory. This chamber is more complex when it comes to its versatility and gas sealing capabilities and is more robust than the old chamber. It is also made of aluminium with an external diameter of 18.0 cm and an interior diameter of 14.5 cm, surrounded by walls with 6.95 cm of height and 3.5 cm of thickness forming the base structure. The window is placed in the middle of the two lids, pressured by two o-rings on the top lid and two o-rings on the bottom lid inserted on the 3 mm cavities (Figure 3.2).

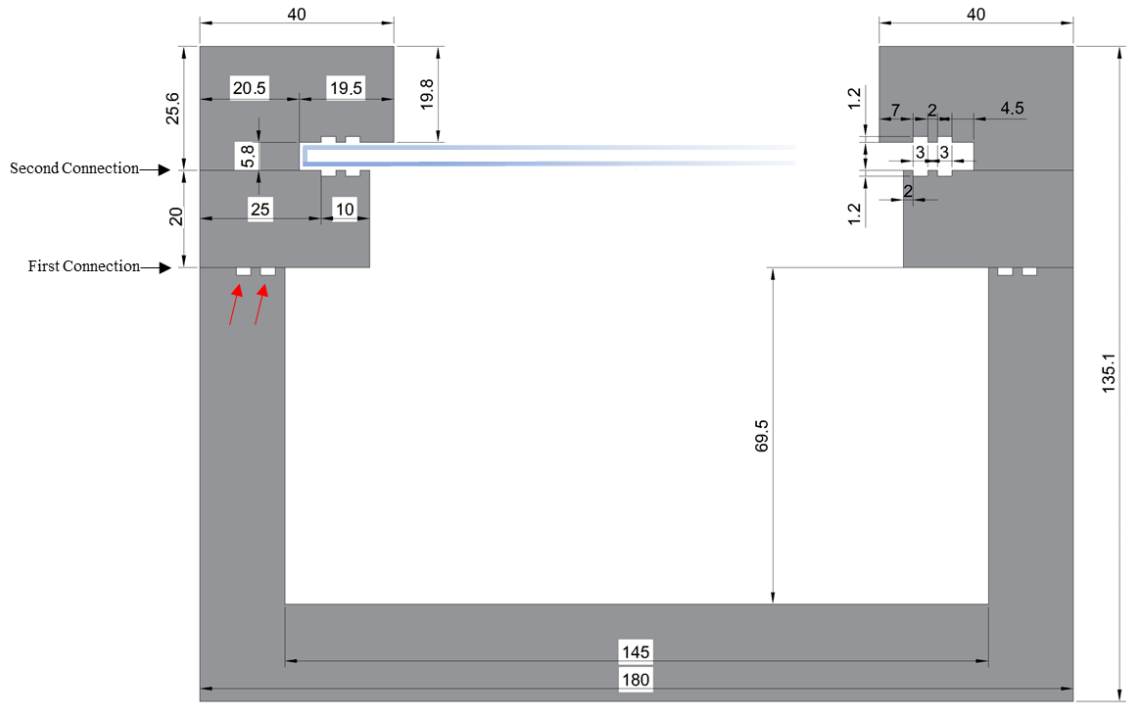

Figure 3.2. Cross section scheme of the new chamber. The units are in millimetres.

The lids remain always connected, if there is a need to place or remove a sample from inside, both are taken together with the windows sandwiched in-between. the inferior is connected to the walls of the base structure, identified in Figure 3.2 as the first connection, which remains connected unless it's necessary a deeper cleaning of the chamber. The upper lid connects to the lower lid and confines the window in between (second connection in Figure 3.2. Every connection is made with screws and the

first connection between base structure and lower lid, uses two O-rings to enhance the total enclosure, located in the pits where the two red arrows in Figure 3.2 are pointed. The window can be in quartz or in polycarbonate. This chamber has 4 connections to the exterior and is also capable of fluid circulation. Further detail on the chamber assembled can be found in the leakage test protocol (**Chapter 3.3.1**).

It is clear that the new chamber has a much more complex design than the old chamber. The gas inlet and outlets have similar pipping and intermediate junction in both chambers. Although the old chamber presents similarity on its connections, the number of valves that can be connected is half (2 connections) than in the new chamber. This will result in the partition of the vacuum, exhaust, pressure gauge and future dopant gas inlet connection for only two chamber connections. The new chamber has four connections, each for a specific process and equipment. Furthermore, the new chamber has a better sealing associated with the number of o-rings and the screws to connect each part. All these reasons will affect the leak rate during future experiments.

Both chambers will be experimentally submitted to low pressure conditions, via a vacuum pump to evaluate its sealing effectiveness. In that way, during the procedure, there is no contamination on the inside since the gas flux would flow from the interior of the chamber to the environmental surrounding if occurs a leakage. To quantify the leak rate of the chambers, both will be submitted to tests, where the tested chamber will be assembled and correctly closed, and the atmospheric gases will be extracted from the interior of the chamber using a vacuum pump through one of the valves. The desired pressure is the maximum low pressure that the chamber can reach, closing the valve after the stabilization is completed. A leakage test for both chambers will be presented in the results chapter.

The laser experiments will be executed with the chamber filled with argon and the sample inside, to prevent surface oxidation or oxide penetration when the melting occurs. It is also to simulate the future project's experiment which the atmosphere will be saturated with the dopant gas ($POCl_3$). The interior of the chamber is purged with Argon (or nitrogen) using another valve, then, after the chamber is fully filled with gas, it is closed. The whole process is repeated at least two more times, finishing with the extraction of the gases from the interior of the chamber, and keeping negative pressure inside without atmospheric gases.

Window details:

The influence of two different windows placed between laser and sample will be studied, to understand the impact of window characteristics on the shallow melting of silicon wafer's surface. There will be used two types of windows from different materials, with similar thickness (5 mm) and transparency (transmittance). A comparison between a quartz window and a polycarbonate window will be made.

Polycarbonate is a thermoplastic material with high temperature resistance and high optical transparency in the infrared. Being a plastic-type material makes it difficult to crack when is submitted to pressure variations. It is chemically resistant, specifically to $POCl_3$. Quartz is a crystalline material with also high temperature stability and resistant to future chemicals used. Quartz has better optical properties than polycarbonate, especially the transmission of light in infrared wavelength.

3.1.2 Laser

The laser used for the experiments is different from the GILD processes presented in the previous section which are related with this work. Those experiments resort on excimer lasers with ultraviolet emission around 308 nm, having a pulse duration between 20 and 60 ns and a low frequency beam rate from 1 to 10 Hz [**36**][**38**][**40**]. This work uses an infrared *Nd:YAG* laser with 1064 nm of wavelength, having a pulse duration from 10 ns up to 220 ns and a beam frequency between 20 and 500 kHz. The brand and the model of the laser are SPI Lasers and G3.1 SM Series Pulsed Fibre Lasers, respectively.

After a detailed analysis of the three scientific articles mentioned above, some laser parameters can be chosen for initial experiments, based on conclusions stated in Chapter 2.6, to maximize the interaction between sample and laser. A shallow melting depth and deepness/surface homogeneity in a sample after laser scattering is the desired goal. According to Figure 2.19.b above 60 or 70 pulses, the sheet resistance starts reaching a limit, since its decrease is less and less relevant. In Figure 2.20, the increase in the number of pulses has a big impact on the melting depth of the sample. In Figure 2.17, a graphical analysis of the energy fluence can give an idea for the initial energy density. For a low melting depth, energy fluence value around 700 mJ/cm^2 could be a starting value for experiments.

Unlike other works, the laser setup in our laboratory does not have a moving sample holder that shifts to different positions where the laser focusses the desired spot, designated as x-y stage. Instead, the laser is equipped with a f-theta lens and a galvanometer which, regarding the incidence laser beam angle, can vertically maintain the focal point on the desired sample plane. It can focus in a squared area up to 100 cm^2, in a concentrated beam, mitigating the dissipated energy. This way, when the laser beam drifts away from the centre of the sample, the focal point will be formed on the surface of the sample, maintaining the energy density constant in the whole process of laser scattering and future doping.

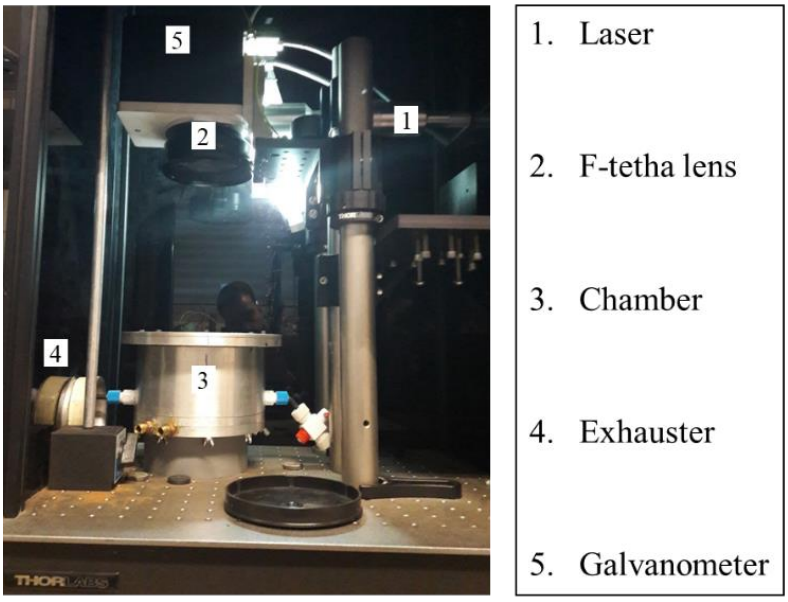

Figure 3.3. Laser compartment with the identification of the main components.

The laser works with ScanMaster software (version ScanMasterTM Designer V2.2) where the variables and the beam form are set. It was defined as the only beam fill movement as Figure 3.4 shows, which represents the beam velocity vector starting at the one of the lower corners and finishing at one of the top corners.

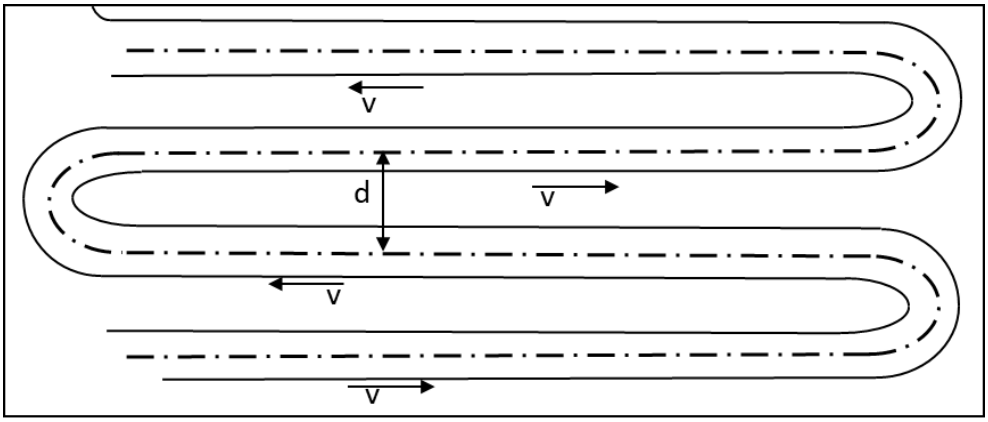

Figure 3.4. Exemplification of the laser beam scatter movement upon the sample's surface.

Due to the beam movement and consecutive beam circular spot, horizontal paths are created which can distanced by an input variable (*d*). Then, d corresponds to the distance between the centre of two consecutive horizontal paths created by the "worm-like" beam movement.

Remembering that the laser used has a pulsed laser beam, it is considerable to refer the consecutive pulsed beam can overlap the previous one, exemplified in Figure 3.5. The distance between successive focal spots can be determined and is related to the pulse frequency (i.e., 500 kHz) and the rastering speed of the laser beam, i.e., for 1000 mm/s the distance corresponds to 2 µm while for 2000 mm/s it is 4 µm. Other related parameters associated with the laser are presented in Table 3-1.

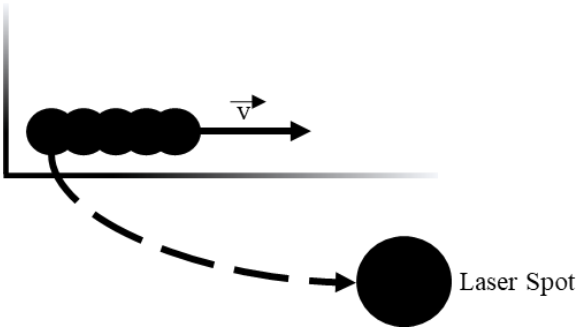

Figure 3.5. Exemplification of consecutive overlapping of the pulsed beams.

Table 3-1. Laser's parameters.

Parameter	Value	Unit
Frequency	500	kHz
Power	20	W
Laser spot area	$1{,}26 \times 10^{-5}$	cm^2
Pulse energy density	3,18	J/cm^2

3.2. Sample details

A comparison between two different types of samples will be under experiments. The first samples have a diameter of 5,1 centimetres, is a p-type ⟨100⟩-oriented Czochralski Si wafers, polished on both sides, with an average resistivity and thickness of 5 Ω.cm and 275 μm, respectively, described for now on as standard wafers. It has a low boron concentration, which, consequentially, means it presents a high resistivity. The second sample specimen has a diameter around 10 centimetres, is a p-type ⟨100⟩-oriented Czochralski Si wafers, polished only on one side (side used to interact with laser) and, for now on, will be referred as emitter. It has a low resistivity, resulted by a high dopant concentration. Its top layer has a higher dopant concentration than the base layer, meaning that it's a p++/p+ stack. The emitter depth is around 0,4 μm and has nearly 10^{20} cm^{-3} of surface dopant concentration, obtained by thermal diffusion of boron. Emitter samples were previous submitted to an HF treatment which removes any oxide layers on the surface of wafers and were cut in wafer quarters with the laser to ensure it easily fits inside the chambers.

Several 10×5 mm^2 rectangles within the wafer samples will be scanned by the laser to minimize the number of wafers used.

3.3. Experimental procedure

The sample processing starts by picking up the wafer type that will be used, removing any dust that lays on its surface using a compressed air pistol and placing it inside the chamber's. The next step is the closing of the chamber and then the start of the purging process. The purging process consists in expelling all the atmospheric gases that rests inside the chamber. Using a vacuum pump and connecting it to one of the chamber's connections to the exterior, a low-pressure state will be induced in the interior, reaching as close as -975 mbar relative pressure value measuring with a manometer. Once the pressure stabilizes, the connection to the vacuum pump is sealed and is opened another connection to a bottle containing argon, enabling the gas inlet inside the chamber. Argon is denser than air, so it can dispense any remaining atmospheric gases since it is a confined space. When chamber is filled with argon, and the pressure reaches the pressure set point defined by a regulator installed outside the argon bottle (approximately 1.05 bar), the connection to the bottle is closed and it's opened the valve connected to the vacuum pump, which will evacuate the chamber and thus extract all the gas inside. This whole purging process is repeated, at least two more times to ensure a vacuum atmosphere in the interior of the chamber. The last step is to leave the chamber filled with argon for further processing.

The next step is to place the chamber inside the laser's compartment and adjust it so that the sample is aligned to the laser. Several rectangles will be scanned on the same sample's surface, representing our laser treated area. These rectangles will be drawn based on different sets of parameters, mainly differing in the laser's scan speed (v), in mm/s, the number of scans (n) and the distance between the centre of two consecutive horizontal laser paths (d), in µm. The first rectangle parameters are set in the ScanMaster software environment, and thus laser-silicon interaction experiments can start. Figure 3.6 represents a scheme of the distribution of the sample areas and in Table 3-2 shows each individual treated area parameters for the sample type described as standard wafers. The sample areas are numbered from 1 to 13, with the parameters hereafter identified as [v,d,n]. From 10 to 13 two different set of parameters are used, and separated by an arrow, meaning that the first set of parameters is executed and after is executed the second set having a time interval of 30 seconds between them.

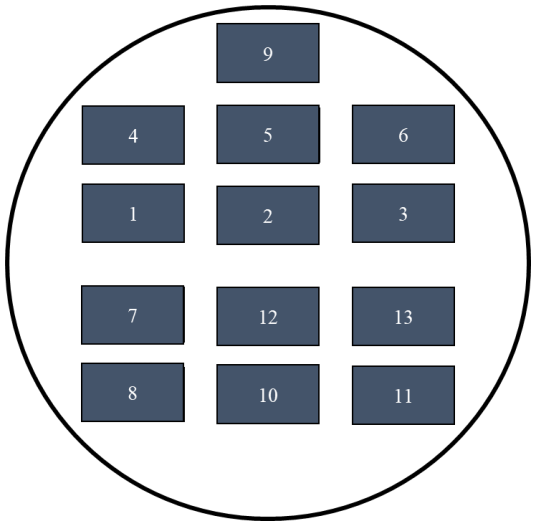

Figure 3.6. Sample areas distribution in standard wafers.

Table 3-2. Parameters associated with each sample area.

Sample Area	v [mm/s]	d [µm]	n [times]		v [mm/s]	d [µm]	n [times]
1	1000	10	1				
2	1000	10	2				
3	1000	10	3				
4	2000	10	1				
5	2000	10	2				
6	2000	10	3				
7	1000	20	1				
8	1000	20	2				
9	1750	10	1				
10	1000	10	2	→	2000	10	2
11	2000	10	2	→	1000	10	2
12	1000	10	1	→	2000	10	1
13	2000	10	1	→	1000	10	1

Over the process, the track of time on each consecutive sample area is important, since this is a temperature dependant experiment. When the laser scans one area, the nearby that were not treated are pre-heated due to the heat the nearest neighbours. Figure 3.7 represents the temporal progression of the total process. The arrows represent the subsequent rectangle area scanned by the laser. It takes around 15 seconds in order to stop the laser, chose the starting position for the next rectangle and switch it on again. Each area from 1 to 9 takes between 2.5 to 15 seconds to have the scan process completed. The total time needed to complete the whole experiment is approximately 6 minutes and 40 seconds. On the right side of the figure when is referred to t_k, with k representing a certain sample area identification, is the time instant before the laser scanned that area.

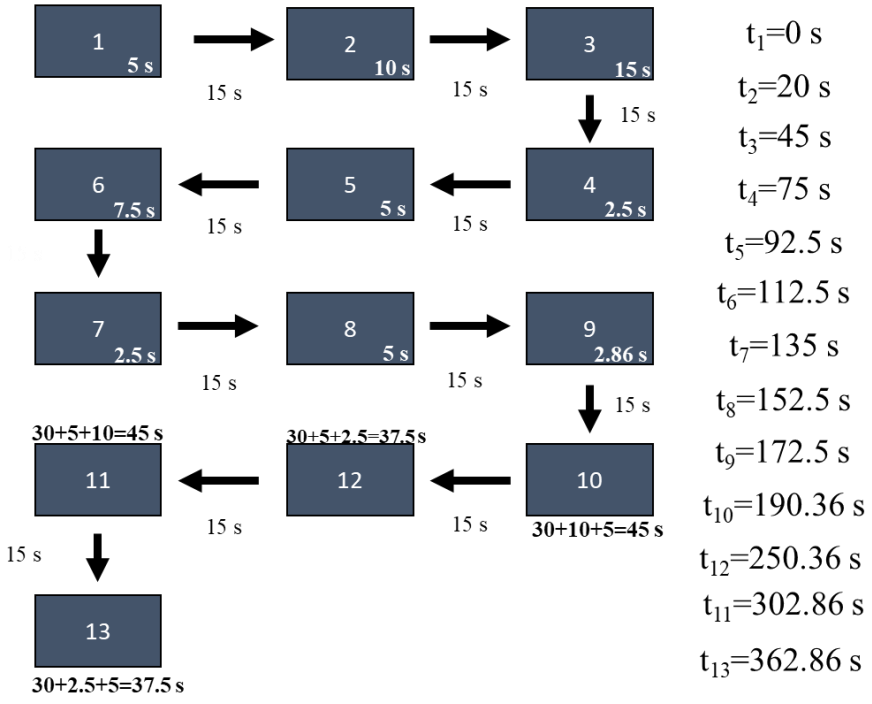

Figure 3.7. Laser scan sequence.

When using the emitter as our test sample the sequence process is the same, although the sample areas that will be treated are on different positions. Due to low visibility while using quartz window which affects the full visibility on emitter samples. These are previously cut in half, only using one hemisphere, as Figure 3.8 shows.

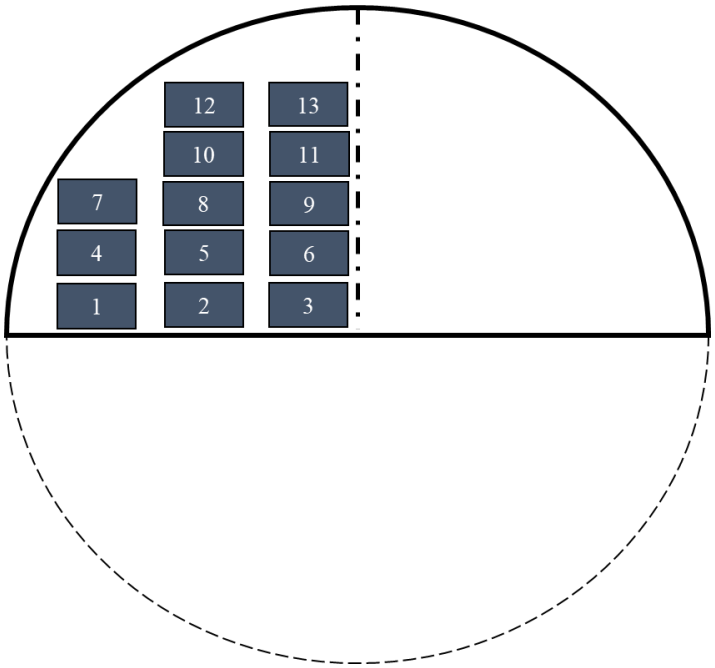

Figure 3.8. Sample areas distribution on emitters.

After the entire laser-silicon interaction process, the chamber is removed from the laser's compartment, the sample is carefully removed from inside the chamber using a tweezer and taken to an optical microscope for observation. Using a Dino-Lite USB camera lens connected to one of the microscope's oculars, the results of the melting process can thus be registered.

3.3.1 Leakage tests

All the components of the new chamber need to be assembled. All the components are stored in the laboratory where took place all the experiments, such as the actual chamber with the valves, first and second ring, O-rings, window, the screws, the screwdriver, the pressure gauge and the vacuum pump. The Figure 3.9 shows all the components needed.

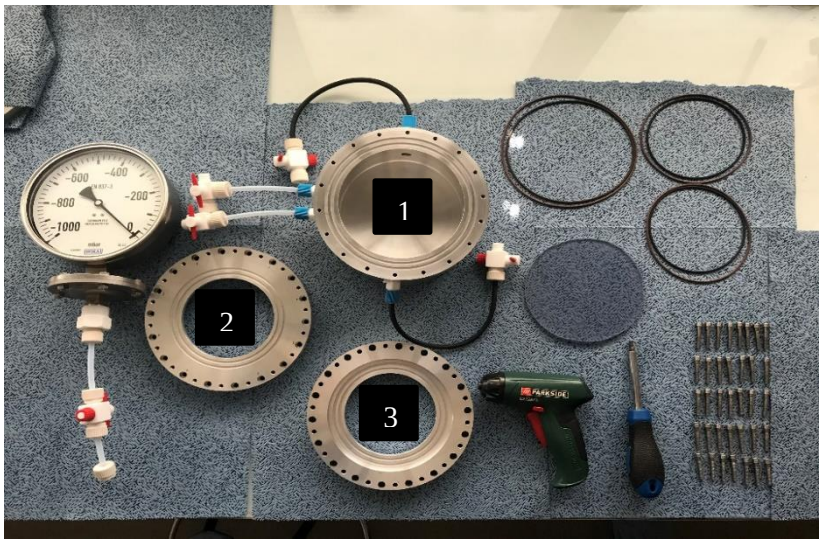

Figure 3.9. New chamber disassembled showing every component and utility that is required to set it up. The number 1 is the base structure where is placed the sample. The number 2 is the lower lid that connects. The number 3 is the upper lid that connects 2. A manometer is also included to control the pressure during the assemblance.

Before starting the steps it's mandatory to check the valve connections (inlet and outlet gas valves) and align the zero marks represented in all 3 components (chamber, 1st and 2nd rings) as Figure 3.10 shows.

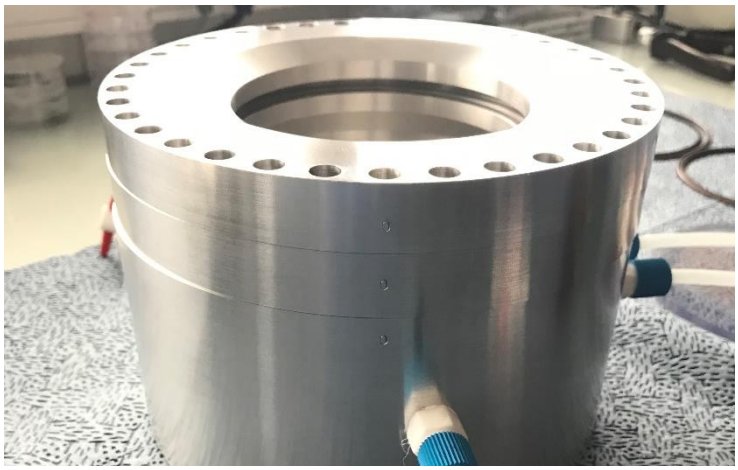

Figure 3.10. Reference mark for the setup.

The first part is tightening between first ring and the chamber. The O-rings are placed inside the chamber cavities before aligning and placing the 1st ring above the chamber (without forgetting the zero-mark alignment with the chamber). The next step is to place the screws on the holes marked by number one and begin tightening. In this step, the top of the screw shall not surpass the top of the hole and the tightening must be crossed.

The process is repeated for the screws now placed on holes marked by number two and then for the remaining bigger holes (the smaller holes must be empty in order to connect 1st and 2nd rings). After, the O-rings and the window are placed on the first ring. The valves to the pressure gauge and to the vacuum pump are connected and closed, as well as the outlet valve identified as exhaust (Figure 3.11). The rigid connections to the valves are placed on objects for support, so they won't be left hanging, as you can see under the three-way valve connected to the pressure gauge.

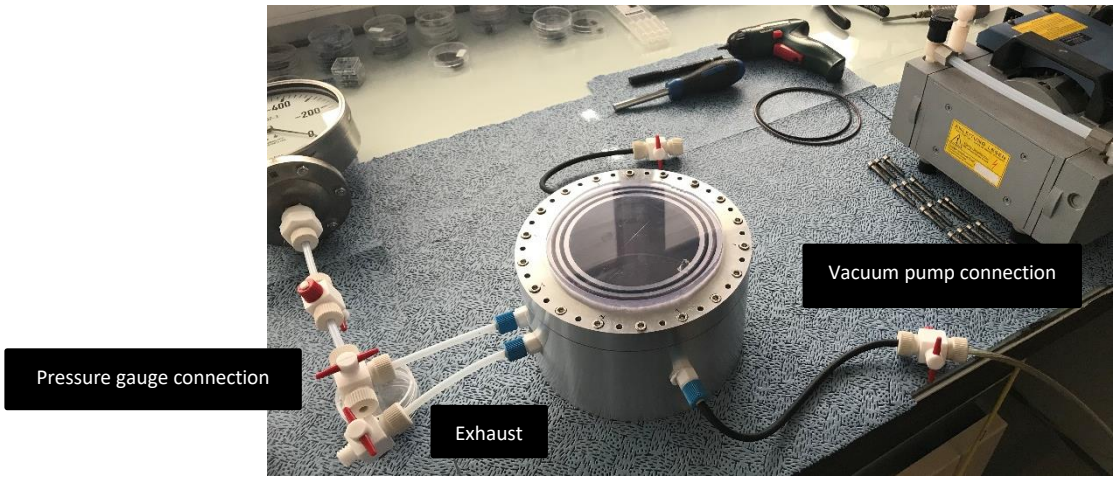

Figure 3.11. Valve connections with the chamber.

The next step is to start the vacuum pump and slowly open the valve connected to the chamber. While the pressure stabilizes, the tightening of all the screws is completed in crossed order, to distribute the applied force. The screws shall not be forced down with too much strength because it can damage the aluminium. When using an electric screwdriver, the grip must be soft so when it's really tightened the screwdriver will draw out. When the pressure stabilizes (about -975 mbar) repeat the last step until the screws are tight and the aluminium surfaces have a minimized space contact.

The second part is tightening between first ring and second ring. First, the exhaust valve is slowly opened until the pressure gauge reaches the atmospheric pressure. The four O-rings are placed in each cavity (top of the 1st ring and bottom of 2nd ring) and the window under the 2nd ring (Figure 3.12).

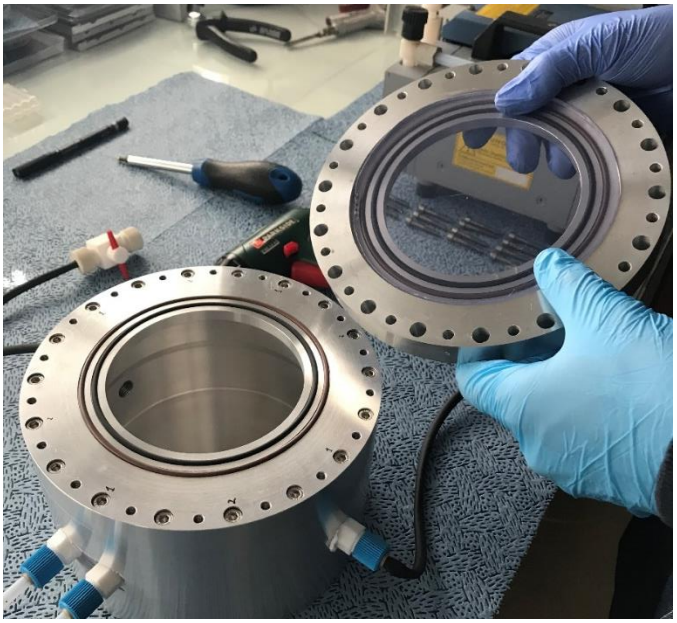

Figure 3.12. Setup for the connection between 1st and 2nd ring.

The bottom of the 2nd ring is placed on the top of the 1st ring and dragged, carefully, in order to match the screw holes of both rings (always alligning with the zero marks).

The screws are inserted inside the holes that have connections with 1st ring holes and begin tightening using the same procedure and having the same cautions as in the first part, until having the chamber assembled (Figure 3.13).

Figure 3.13. Chamber connected with 1st and 2nd rings.

Finally, the vaccum process described in the first part for the screws tithgning is repeated.

The third part is the leakage test, where the valve connection between vacuum pump is closed while the chamber is under minimum pressure values. The time begins to be clocked and the valve connected to the pressure gauge remains opened. Within certain time intervals, the pressure presented in the pressure gauge is registered. The process is repeated long as wanted.

3.3.2 Laser–silicon interaction tests

The first step for creation and cutting of samples is turning the necessary equipment on, like the PC, the Camera Adapter, and the monitor, which allows the observation of the laser path during the procedure, the 'ScanMaster 1000' and the circuit board plugged in to the power source, necessary to start the laser scan in cutting or melting process. In this work, the creation of samples, or the melting process, was the main goal. The sample cutting was also an important step, which allows us to separate the different sample areas individually and send the chosen ones for future characterization analysis.

The second step is in the PC, where the laser program ('Laser-HyperTerminal') is opened, and the following codes are written to set up with the conditions that will be used (Described in Annex G):

For cutting of samples ('SR 350000'), the first step is open the file 'Cutting of Samples' which is in the S-LoTTuSS group project shared drive. The file can be used to cut new frames and to cut samples. It has 2 circles already, which can be used to put a standard wafer or the emitter in place (smaller and larger circle, respectively), a quarter of circle frame (to hold ¼ of the emitter, Figure 3.14) and a larger circle, to cut the edges of a *c-Si* either for frames or just to put on the base of the chamber. There are also dots, text, and lines already, the last of these can be freely dimensioned and are pre-programmed with the variables to cut, which are:

- Speed of 200 mm/s;
- 10 number of repetitions;
- Wobble thickness of 0.1 mm;
- Wobble overlap of 80%.

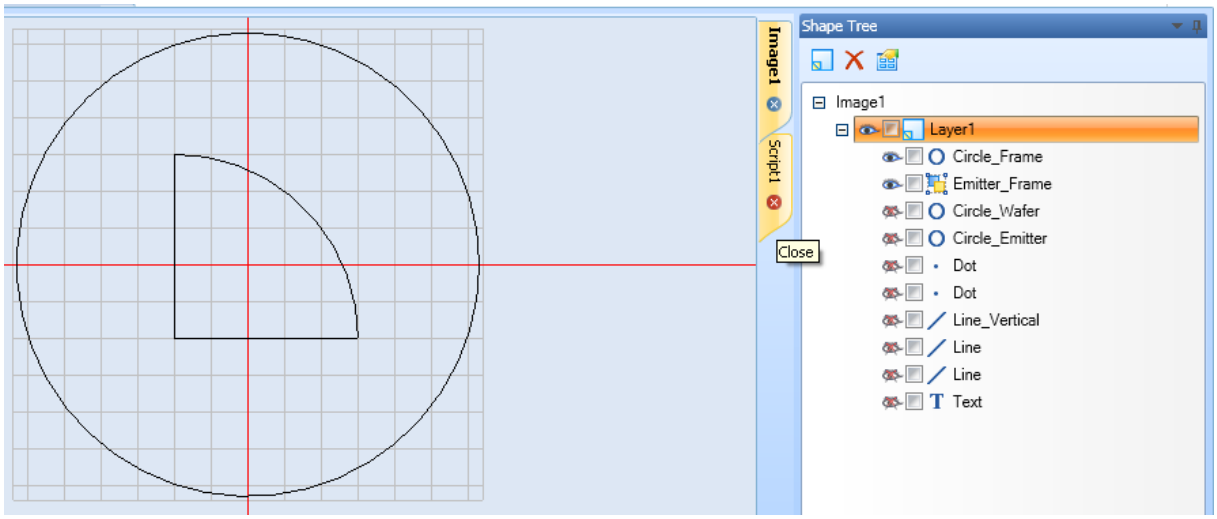

Figure 3.14. 1/4 circle frame, to hold the emitter.

The third step is to place the sample on a Microscope slide. If the microscope slide is not new (or if it does not look clean), a cleaning is done as it follows:

- Using a cotton prepping ball and clean with isopropanol;
- Using another cotton prepping ball and clean with ethanol;
- A last cotton prepping ball is required to dry the slide.
- The argon pressure pistol is used to finish the drying process and remove some cotton fibers.

The fourth step is to align the lines of the laser with the sample, on the spots where the cutting will be done. For this, a circle command for standard wafer or emitter, depending on the sample used, is selected and the play button is pressed. This process is repeated until the sample is in the right spot.

Once the sample is on right spot, the laser door is closed, the 'play' button is pressed and, at the same time, the needle of the circuit board is moved to the pins located at "5+ Voltage", closing the circuit. Only now the laser beam is on.

After the laser has done all the desired repetitions, the needle returns to its initial position, out of the zone of the rectangle (+5 Voltage). Finally, the wafer is removed carefully, placed in a paper towel, covering the sample, and gently applied force on the opposite side of the cut, until it cracks. The argon pressure pistol is used to clean the final wafer.

To cut a standard wafer, 3 repetitions should be enough, for an emitter, at least 5 repetitions are necessary.

To cut samples for AFM, SEM, SIMS: The areas for this type of analysis must be small. So, the hatch sample must be cut in half.

To procedure for the laser-silicon interaction or creating samples the 'SR 500000' command is used. The first step is to open the respective files, inside the S-LoTTuSS group project, "Creation of Samples - Emitter" (Figure 3.15 and 3.16) or "Creation of Samples – Standard Wafer" (Figure 3.17), if the sample is an emitter or a standard wafer, respectively.

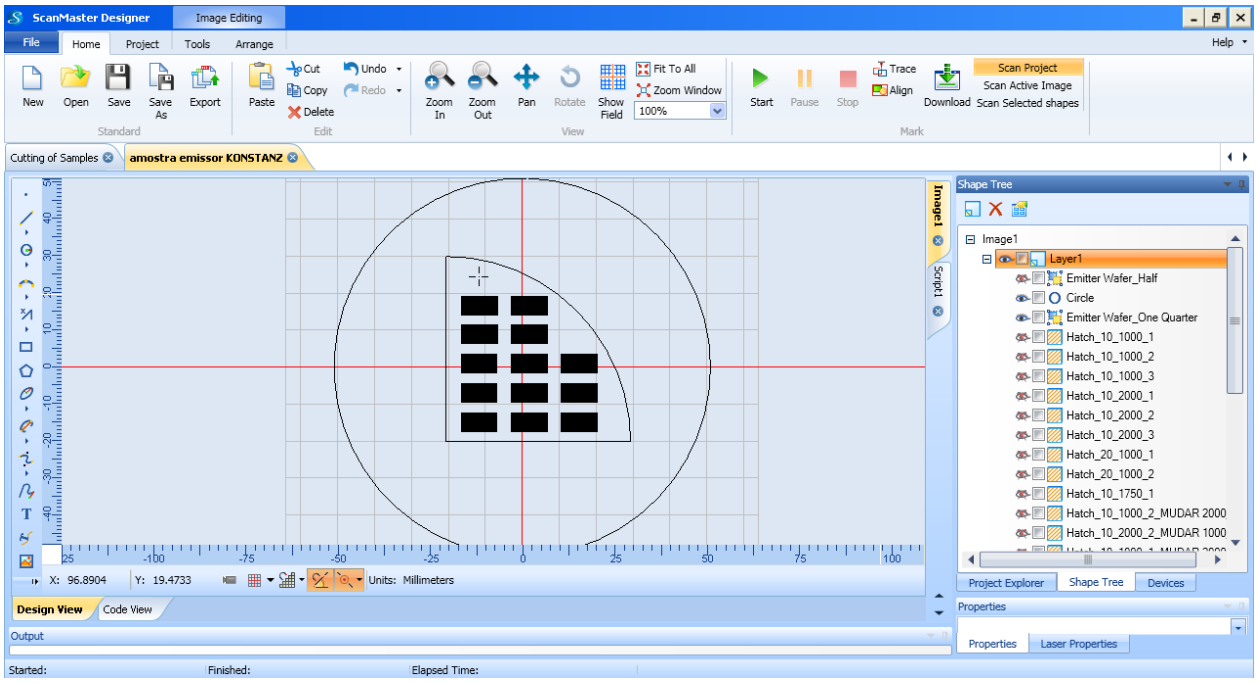

Figure 3.15. Layout of the file "Creation of Samples – Emitter", set to create a sample on a 1/4 emitter, with the hatches.

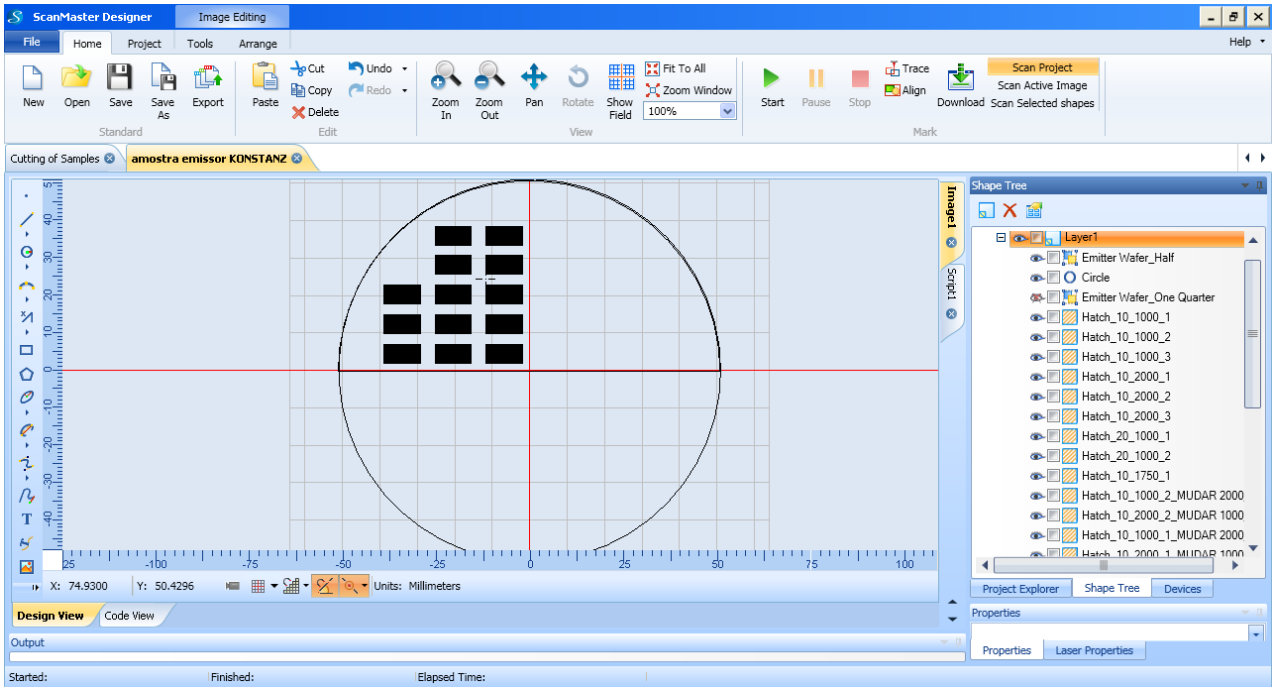

Figure 3.16. Layout of the file 'Creation of Samples – Emitter', set to create a sample on a semi-circle emitter, with the respective hatches. the other hatches to create a 1/4 circle sample are hidden.

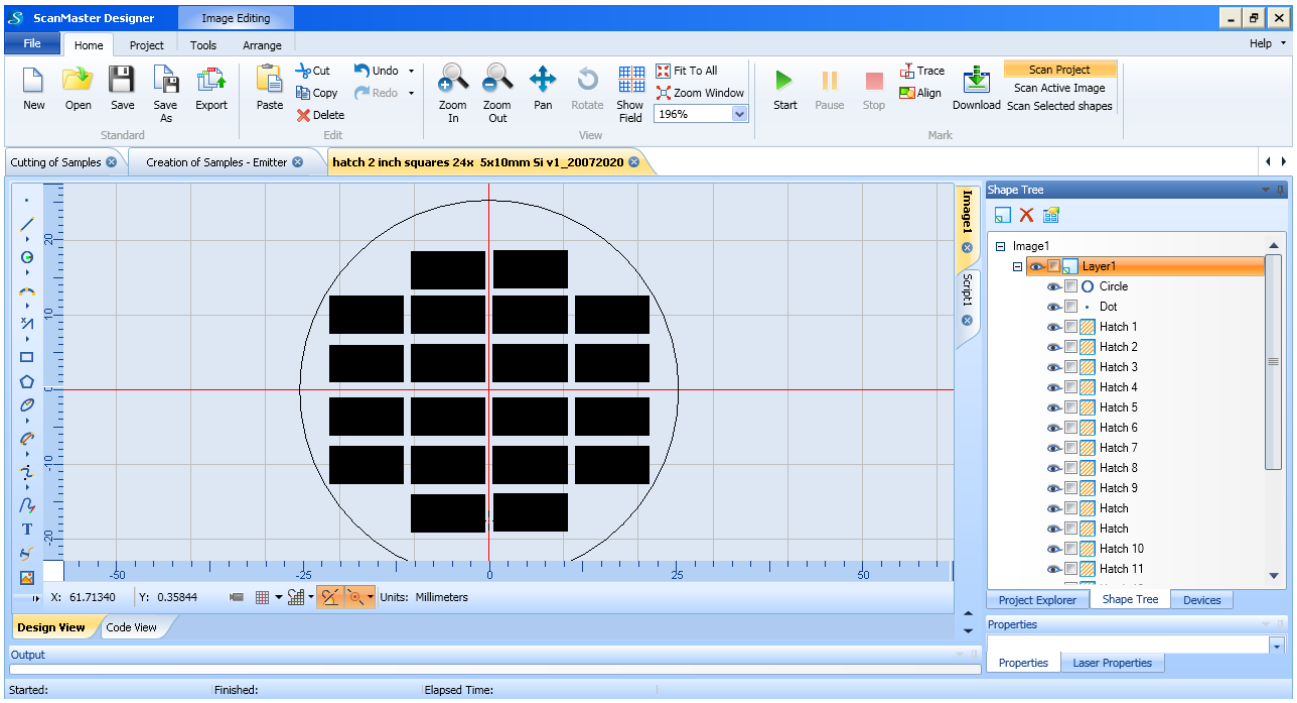

Figure 3.17. Layout of the file 'Creation of Samples – Standard Wafer', with hatches pre-programmed for the entire wafer.

Each file has a circle (semi-circle or ¼ circle for the emitter), which can be used to put a standard wafer or the emitter in place. There are also hatches in place, that can be changed to meet the requirements, like speed, repetitions, and distance between lines.

The third step is the same as the fourth step for cutting the sample. In this case, since there are many sample areas inside the wafer area, for each area processed, it's necessary to place a dot near the sample area that will be scanned, and press play to confirm its position. This is important because it prevents the laser beam to drag over the sample areas already created.

The fourth step is to set the parameters laser beam speed, the distance between the centre of two consecutive horizontal paths and the number of laser scans. After, the laser door is closed and the play button is pressed at the same time, as the needle of the circuit board is moved to the pins on the right (5+ Voltage, Figure 3.24). When the laser has done all the desired repetitions, the needle returns to its initial position.

After the procedure is completed, the sample is removed carefully from the laser's chamber and placed inside a Petri dish to prevent the accumulation of atmospheric particles.

3.4. Samples characterization

The samples areas produced within the wafer's surface, will be submitted to a detailed analysis. The interaction (melting) homogeneity and the topographic smoothness of the surface will be characterized by optical microscopy and SEM technique, respectively.

3.4.1 Optical Microscopy

There are different approaches for the optimal wafer selection, according to the variables and parameters used. A detailed analysis via microscope is an initial step to the assortment of the total scan effectiveness, related to the optics on the chamber (types of window material) and the effect of chamber and sample purging. For this microscope analysis, the *Dino-Lite Digital Microscope Software* presents microscale imaging comparison which allow us to evaluate the optimal parameters and select the samples for the topographical surface characterization.

After the laser scans the sample areas, the wafer is removed from the chamber and placed on the microscope's base holder to be visualized. With the help of a digital microscope USB camera (Dino-Lite) and replacing one of the two microscope ocular eyepiece, it is possible to take pictures from the melting results in a computer.

The microscope digital lens cannot capture the entire sample treated area with minimum zoom, so there will be taken several pictures from relevant portions of specific areas. The maximum zoom will be used to register detailed phenomena of the laser's path. All images have the same dimensions (3.4×4.67 cm), on the bottom left corner is identified the position in the surface of the sample area treated, and on the bottom right corner is identified the scale. The relative positions on the group of pictures are identified on Figure 3.18. It is important to say that the images registered from the sample areas near the wafer border have more incident luminosity, due to the light source included on both sides of the microscope, than the centre sample areas, which are darker. To highlight the difference between treated areas and non-treated areas all the images were enhanced 40% in its luminosity, so that the areas successfully treated by the laser be as bright as possible and the non-treated areas or the outside of the sample areas rectangle be as dark as possible.

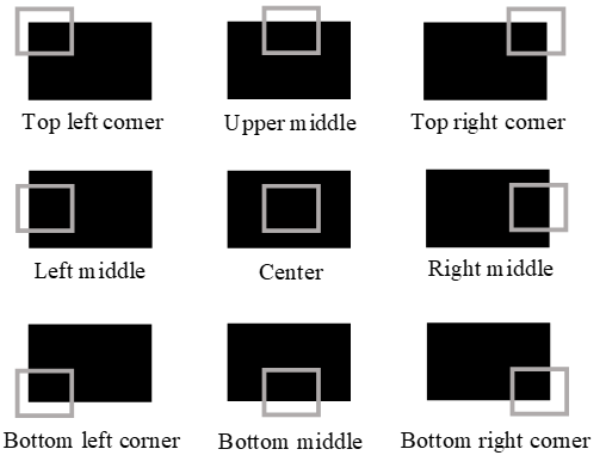

Figure 3.18. Relative position of the microscope pictures registered.

3.4.2 SEM

The topographical characterization of the samples results will be analysed using SEM technique. The sample areas were sent to be processed in the MicroLab – Electron Microscopy Laboratory (*ICEMS/IST- Institute of Materials and Surfaces Science and Engineering*) at University of Lisbon, Instituto Superior Técnico. The results will be used to complement the analysis using optical microscopy. Unfortunately, the results from the SEM analysis are only for certain sample areas using the standard wafer (p+) and the polycarbonate window. For the emitter (p++/p+) there was only one area analysed via SEM [*v*,*d*,*n*]=[1000,10,1]. The other results were obtained but had other parameter values, which weren't studied during this dissertation work.

4. Results and analysis

4.1. Chamber leakage

The old chamber was submitted to a leakage experiment prior to this dissertation. It was used a quartz window with the aluminium frame as the top lid. During the experiments, the valve between the chamber and the pressure manometer was kept always opened (i.e. during evacuation and further pressure reading), and then the pressure values registered over time after the evacuation step. In case of the new chamber, one of the tasks of this dissertation was to develop a protocol to successfully close the whole chamber's setup and register the measurement using the same conditions and window as the old chamber. Both results are registered in the graphic of Figure 4.1. The minimum pressure value that the old chamber can reach is -950 mbar which is relatively good as the new chamber can achieve -975 mbar. Although the minimum pressure on both chambers is considerably optimal, there is a huge discrepancy over time. The new chamber can maintain its minimum value over 11 minutes, while the old chamber has a drastic pressure stabilization, and after 11 minutes reaches -340 mbar.

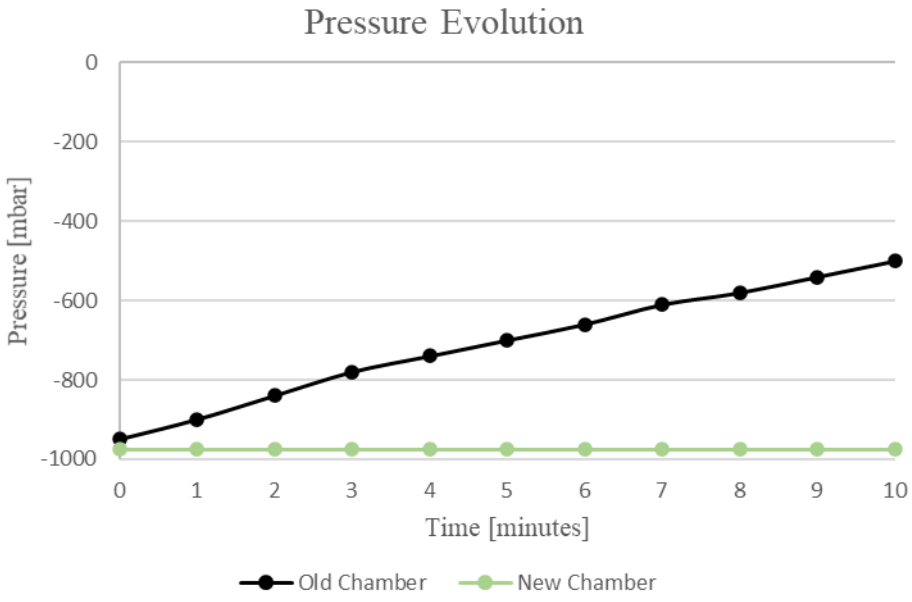

Figure 4.1. The evolution of pressure conditions inside both chambers.

To observe a pressure stabilization on the new chamber, it was left sealed over a longer period. It was registered the pressure after 2 hours, maintaining a value of -975 mbar. The value of -950 mbar was observed after two days of experiment. The leak rate is the pressure lost (increased inside the chamber) per unit of volume in a certain amount of time. For the old chamber the leak rate is around 0,75 mbar/L/s, while for the new chamber extrapolated to two days, the leak rate reaches $1{,}45 \times 10^{-4}$ mbar/L/s.

It is possible to state that the new chamber has a higher sealing capability, presenting a lower minimum pressure value and a superior pressure retention over time. The old chamber has an easier handling and setup assemblance, but it presents a higher leak rate over time. Since the laser experiments takes around 7 minutes, the pressure values are still considerably low. Plus, at this phase of the project there is no dopant gas utilization or high levels of toxicity, however leakage from inside to the outside

and vice-versa was the main concern to this experiment. That said, the new chamber won't be used for silicon and laser interactions, it will be reserved to the future doping experiments.

4.2. Laser – Silicon interaction

In this section it will be presented and analysed the results associated with the melting effectiveness when varying three groups of variables while using the old chamber. The effect of the window type, the laser parameters mentioned before [*v*,*d*,*n*], and the difference between emitter and standard wafer, when scanned by the laser. In the **Annex A, B** and **C** is presented, as a group of images, the results from different experiments:

- In the **Annex A** are presented the results from the laser interaction using a standard wafer and the polycarbonate window.
- In the **Annex B** are presented the results from the laser interaction using a standard wafer and a quartz window.
- In the **Annex C** are presented the results from the laser interaction using the p-doped emitter as our sample and a polycarbonate window.

In the three annexes mentioned above are presented the sample areas treated by the laser as a group of images, each group is divided by several portions of the same sample. For each group is also identified the relative position of the sample area within the whole wafer, and a black rectangle with values associated with the parameters used, where the first represents the scan speed of the laser beam (*v*), the second is the distance between the centre of two consecutive horizontal paths (*d*) and the third is the number of scans (*n*). For the following analysis, the comparisons between different sample areas, will be referenced to the respective figures, with some portions included throughout the text. Every sample area presented along the text of this chapter as its correspondent image group with the scale bar associated.

Figure 4.2 is an example of an area, processed with laser where the melting of the sample surface may have occurred. The dark regions, between lines and on the side, are the areas where the laser didn't irradiate, while the brighter zones, horizontal paths and curves associated with the worm-like movement represented in Figure 3.4, are the zones affected by the laser, which is the path that the laser beam made during the scanning process. Then, the brighter areas (paths) are the zones where there a clear interaction between the laser beam and the silicon sample surface.

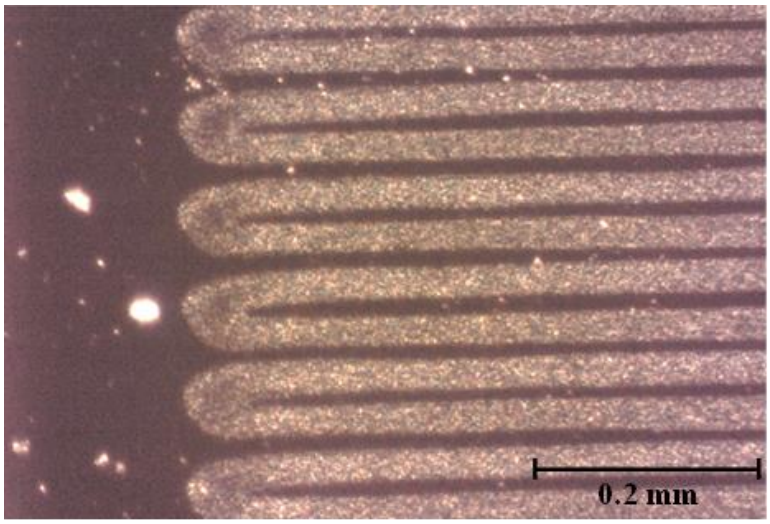

Figure 4.2. Exemplification of the successful interaction (bright path) and non-treated area by laser.

4.2.1 Window Effect

The first analysis that will be made is on the effect of the window type on the beam interaction with silicon, where the main the potential reasons are going to be further explained. As stated in the previous chapter, a crystal material as quartz has better optical properties, mainly transmittance, than a plastic material as polycarbonate.

The sample areas comparisons will be inserted alongside the analysis, others will be complementary referenced and compared between **Annex A** the ones in **Annex B**, the results, according to the energy deposition values, were as expected. In every portion of surface irradiated by the laser, using the quartz window (**Annex B**), may occur the melting, material ablation or even a mix of both, on the wafer's surface, meaning that laser beam effectively interacts within the sample area. On the other hand, using the polycarbonate window, there are samples areas that does not interact with the laser when it scans. The laser's parameters which were expected to have low interaction with silicon were sample areas under high scan speed and using single scans, such as in Figure 7.7 (polycarbonate window) and in Figure 7.20 (quartz window), that inputs [*v*,*d*,*n*]=[2000,10,1]. And, as Figure 4.3 exemplifies, even with parameters with low expectations of interaction, using quartz window the interaction is completed on the whole surface, while with polycarbonate the interaction is deficient.

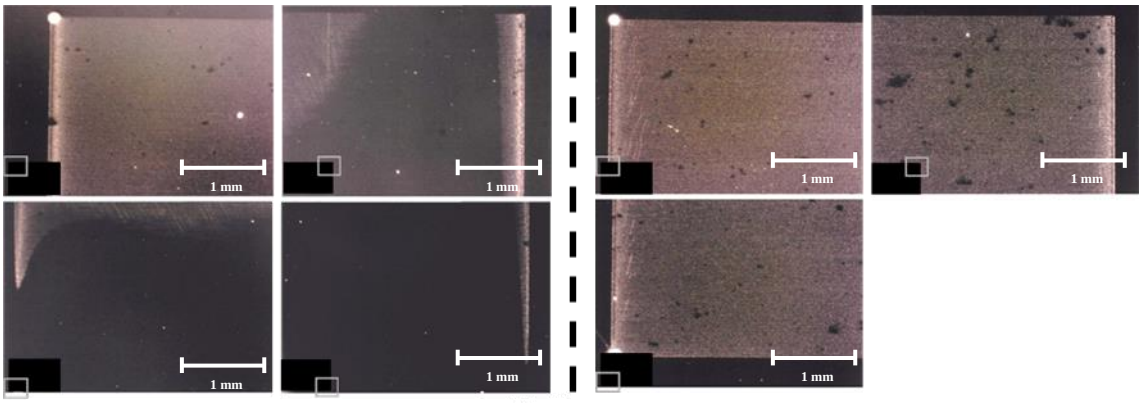

Figure 4.3. Laser-Silicon interaction when varying the window material. On the left, sample area 4 using polycarbonate window. On the right, sample area 4 using quartz window.

When we scan the sample area just one time, it's noticed that the bottom half have a big zone with no laser interaction. The initial laser beam when the scan starts may not be completely transmitted through the polycarbonate window, seems that it takes time to fully transmit the beam and focus on the surface (Figure 4.4). The optical capability of polycarbonate is not as good as quartz, that could be one reason we have these pitch-black areas when only one scan is executed. Another reason could be the wafer temperature. When sample area 7 is scanned we get heat from the previous areas already scanned by the laser. This could interfere in a way that the laser will scan an area that has a higher temperature when compared to the previous one, explaining the reason why sample area 7 has an overall better treatment than sample area 1.

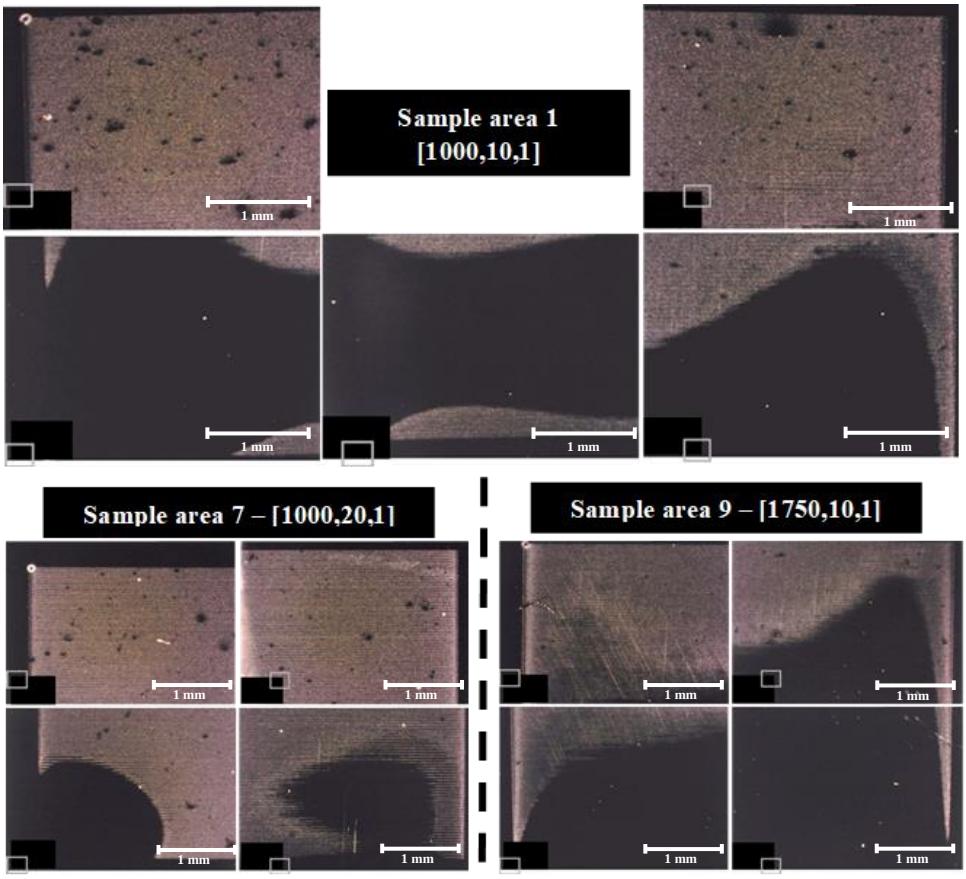

Figure 4.4. Appearance of dark regions using polycarbonate window.

On the other hand, every sample area that was submitted to laser melting using the quartz window has a successful homogenous interaction throughout the beam path. So, to study and analyse the impact of different set of parameters, it will be visualized the melting effectiveness mainly on the standard wafer with the polycarbonate window.

4.2.2 Influence of parameters

Considering the scan speed of the laser beam (v) as a start, it was expected to obtain a more efficient and shallow homogenous melting results for a lower scan speed, since the longer the laser remains irradiating the sample surface, the larger the amount of energy delivered on the wafer. This can also be directly related to the distance between the centre of two consecutive horizontal laser paths (d). The lower the distance, more horizontal paths are created throughout the height of the sample area. This means that more energy is deposited since the pulsed beams occur during a larger period. All these predicted results were calculated accordingly to the sample area, the pulse frequency, the laser's power and the set of parameters. The delivered energy relation between different single sets used are presented in Table 4-1. The number of pulses per row was calculated with the quotient from the width of the sample and the distance between successive beam focal points. The number of rows is calculated as the quotient between the sample height and d. Finally, to calculate the energy deposited in one scan, is required the energy per laser pulse, given by the Equation 4.1:

$$Energy\ per\ pulse = \frac{Laser\ power}{Laser\ frequency} = \frac{20\ W}{500\ kHz} = 4.0 \times 10^{-5}\ J \tag{4.1}$$

The energy pulse must be normalized according to the laser spot area to obtain the value of energy density per pulse (Table 3-1).

Then, the total energy per scan is the product of energy per pulse, number of rows and the number of pulses per row. Note that this are approximated values. In addition, there is also losses due to optical effects (window losses).

Table 4-1. Energy deposition on different parameter's sets.

Variables	**Values**				**Units**
v	1000	1000	1750	2000	[mm/s]
d	10	20	10	10	[µm]
The distance between successive focal spots	2	2	3.5	4	[µm]
Number of pulses per row	5000	5000	2857	2500	[pulses]
Number of horizontal rows	500	250	500	500	[rows]
Energy per scan	**100**	**50**	**57**	**50**	**[J]**

When the laser sweeps the area with 1000 mm/s pulsed beam velocity, the sample gets a total approximated value of around 100 J, which is twice the energy deposited when setting the speed to 2000 mm/s as the number of pulses is twice in the first case (for the same d).

The results associated with the variation of the laser velocity were consistent with those expected. Figure 4.5 demonstrates the decrease on laser-silicon interaction as the laser beam velocity increases. Analysing the group of images, sample area 1 has better and homogenous surface melting, while sample areas 4 and 9 has equivalent interaction since the energy deposition is approximately the same. The group of images are from Figures 7.1, 7.4 and 7.9 in **Annex A**.

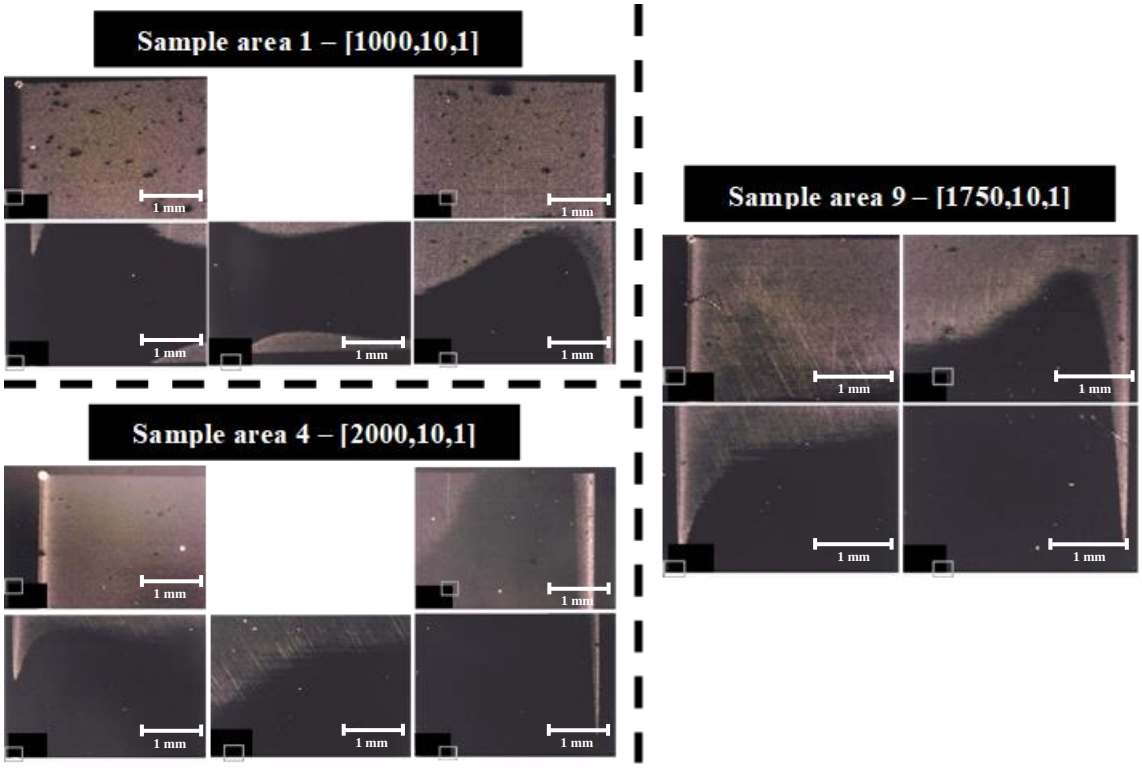

Figure 4.5. Melting effectiveness when increasing laser beam velocity. Polycarbonate window.

For the next analysis, we take into consideration *d* as the variable. For the same laser beam speed, when the distance between horizontal paths (*d*) doubles, it is expected sample areas to have lower melting effectiveness or poor interaction, since the energy deposition is halved. Figure 4.6 compares the melting effectiveness when we double the *d*. The results were not as expected, since area 7, overall, shows a bigger area where the laser successfully interacted than sample area 1. One of the reasons that may explain the unexpected results was the experimental sequence of each consecutive sample areas and the temperature increase on the entire wafer. Considering that the wafer is already heated by previous sample areas, the region 7 starts the scan at a higher temperature than area number 1, even though sample area 7 has half of energy implemented than sample area 1. It is also important to consider that, in this case, if sample area 7 was the first area to be process, the interaction could have been worse because there was no previous laser irradiation and, consequentially, no wafer heating. Following the scan order 1→2→3→4→5→6→7 of the processed areas inside the same silicon wafer, if sample area 1 was swapped with sample area 5, probably the result would be better since the wafer was already heated when the previous areas was scanned.

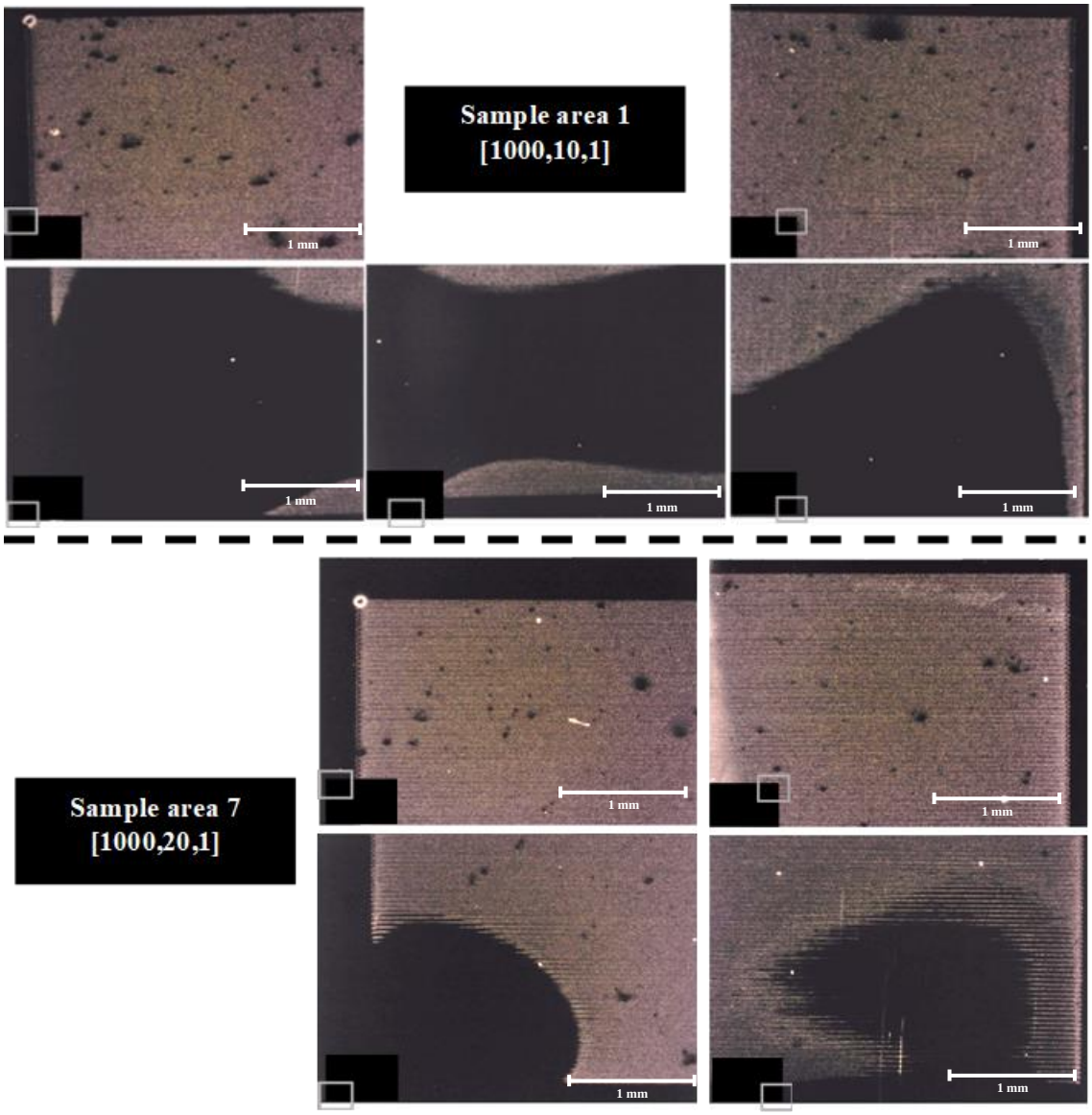

Figure 4.6. Melting effectiveness when increasing the distance between the centre of two consecutive horizontal paths. Polycarbonate window.

The third variable that can be studied is the number of complete scans carrier out by the laser over a single area. While maintaining the other two variables constant, it is predictable that for each successive complete scan, the entire area gets melted or, in other words, the probability to have the entire sample area fully bright (successful interaction with the laser) is increased. It is proven that with each consecutive completed scan, the regions that the laser did not successfully interact inside the sample area with the previous scan sequence, are corrected and melted with the next scan. Figure 4.7 exemplifies the correction by successive laser scans, where the left image presents a round black spot in the bottom left corner, and the right image demonstrates that the area was still with black appearance but was corrected by the second scan. This behaviour can also be seen on Figures 7.4, 7.5, 7.6, for lower beam speed, and Figures 7.7, 7.8, 7.9, for higher beam velocity, in the **Annex A**.

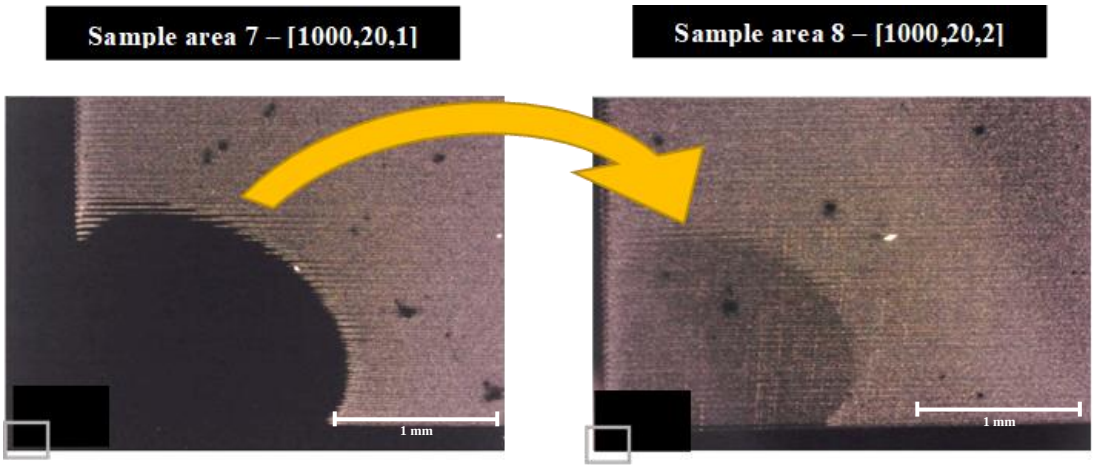

Figure 4.7. Example of the successive laser correction on dark spots. Polycarbonate window.

At last, due to highly temperature dependence for the initial stages of the scan, it was implemented another type of scan set. The idea was to separate two different scan sets by a 30 second interval and varying the laser beam velocity. Sample areas 10 and 12 started with low laser scan speed (1000 mm/s) and, after the interval time, it is finished with a high scan speed step. In sample areas 11 and 13, the opposite sequence is carried out, where it starts with high speed (2000 mm/s) and end with a lower speed (1000 mm/s) in separated scans. The idea of starting with a slower speed laser scan (v) was to get an initial melt and end with two faster scans. The first set at a lower speed begins the melting and treats the area, the last set of scans is a faster process, making surface more homogenous. This type of laser irradiation will be considered as superficial melting and homogenous melting. Starting with higher scan rates, the area should not be as well treated as if it was with slower scans, instead this first set would pre-heat the sample area. The last set would hard process a previously heated area increasing the interaction. This method of separated laser scans will be expected to realize an in-depth melting.

In the 7.40, a comparison between a single scan and both melting methods is represented. Sample area 12 seems to mitigate the unsuccessfully treated area equivalent to 1. In sample area 10 it's observed a higher brightness in the regions that 1 and 12 were pitch-black. So, the performance of the laser is enhanced in the last set of parameters at the previously dark spots rather than the successfully treated regions.

An overall energy related, and the respective melting effectiveness comparison is made on Figure 7.41. Comparing sample areas 1 and 2 there is a noticeable difference for each consecutive laser scan. The first scan with a lower speed seems not only to treat most of the sample area but also heats it. So, the next scan increases the interaction on the treated area and corrects by fulfilling the pitch-black areas. Comparing 4 and 5 there is not much of a improve, the sample areas are similar, and even with one scan seems to get a bigger treated area (which hypothetically should be the contrary). Analysing 1 and 2 with 4 and 5, respectively, we can notice a considerable difference on the surface treatment by lowering the laser scan velocity, the result is a more homogenous, well treated and less dark sample area. Comparing 11 and 13 we get a similar behaviour when we are comparing 1 and 2, i.e., the second consecutive scan makes a large difference for the treatment of the entire sample area. When we use 2 scan sets, we get better interaction results, not only because the total amount of energy deposited is proportional to the number of scans, but also the pre-heating process gives us a better laser-Si interaction. Another interesting behaviour is the results associated with Figures 7.6, 7.12, 7.13, where the total energy deposited is approximately the same (150 J) and, while on the two separated laser sets the result is similar, in the sample wafer 6 (Figure 7.6) the surface melting profile is different by using 3 consecutive scans at a higher velocity (2000 mm/s).

4.3. Curious interactions and phenomena

During the experimental process and, later, in the microscopic observations, it was noticed some unpredictable interactions. When analysing the results, it was observed that most sample areas have black dots, randomly distributed across the surface (Figure 4.8). By just a microscopic observation, it's not possible do determine exactly the cause of this. Some hypotheses were taken into consideration, such as the window condition, which may present some scratches or micro-cracks. This laser experiment is a highly temperature dependent and extremely precise optical process, which also include a possible nano interaction that takes place on both surfaces of the window. Any presence of minimal dirtiness that lays on the window will affect the laser scan. If the laser, while scanning the sample, is optically obstructed with some minimal dust that is on the surface of the window or even the sample, it automatically heats up, melts and attaches where it lays, compromising the direct laser radiation to reach the surface of the wafer.

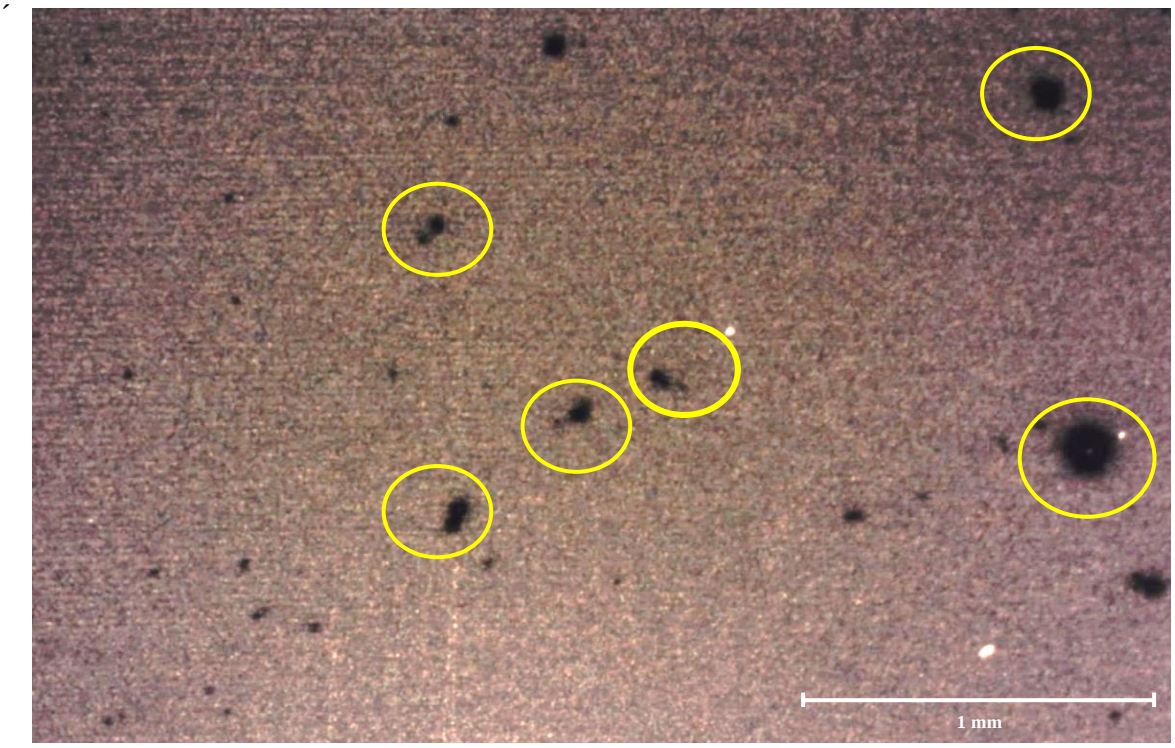

Figure 4.8. Small black dots across sample areas.

While observing the different wafers, it was seen that the height of the horizontal paths created by the laser and the distance between them weren't constant across the entire width. Then, a new experiment where the distance between the centre of two consecutive horizontal paths was increased to verify this statement. With a set of parameters equals to [*v*,*d*,*n*]=[1000,40,1], using a standard wafer and a polycarbonate window. The scanning process was executed, where it was registered several maximum zoomed images across the width of the sample area, to group and create a horizontal profile. Note that the right corner doesn't show the beam curve, due to damage on the wafer. The result shows that the distance between the edged of the horizontal laser paths increases as we it moves closer to the border, while on the middle is minimal. This is due to the neighbourhood heat, which increases the performance of the interaction between laser and silicon.

The movement of the laser is a worm-like movement, where it progresses horizontally across the sample area, curves on the border and moves in the opposite direction. But, when the laser approximates the curve, it deaccelerates, curves and then begins to accelerate again. Then, the time it takes to move from A to B, in Figure 4.9, is longer on the borders than in the centre. When the laser speed is lower (on the borders), the more residual temperature is left from the previous position, resulting in the better melting on the spot and in the surroundings. The full horizontal sample profile, can be seen in the **Annex F**.

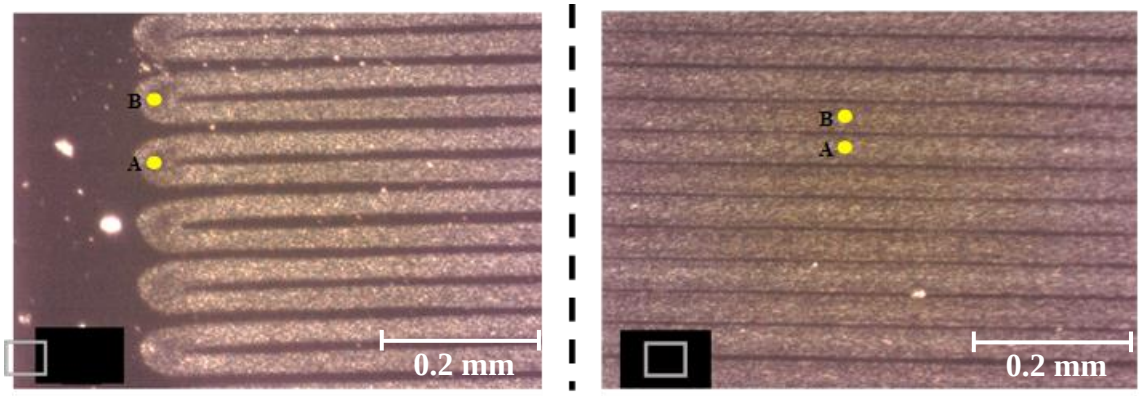

Figure 4.9. Exemplification of the neighbourhood heat phenomenon.

The last phenomenon took place exclusively using the quartz window and is presented in Figure 4.10. While analysing the sample areas, it was observed that under low-speed laser scans (1000 mm/s), there was a high circular interaction on the borders that often spread to the centre. Those borders interactions, since they are brighter than the centre of the sample, shows that in those regions the melting process was enhanced, and the laser interaction was maximized. A possible explanation could be the deacceleration during the curve of the laser on the borders. With the optical capability of quartz, the interaction between laser and silicon is facilitated due to optimal transmittance, and it is known that when the laser decreases its beam speed during the curve, it increases the time it resides on those regions. When the laser-silicon interaction is augmented, it occurs an over-melting that spreads to its surroundings. This only appears on sample areas that are affected to low speed laser scans, due to the proportionality between the beam speed and the residence time at the curves. Notice that in Figure 4.10, the sample area 11 has the bigger interaction on the borders, since is under an in-depth melting, which consists in a high-speed scan set (2000 mm/s) first that has less interaction but pre-heats the surface for the second scan set have a maximized interaction.

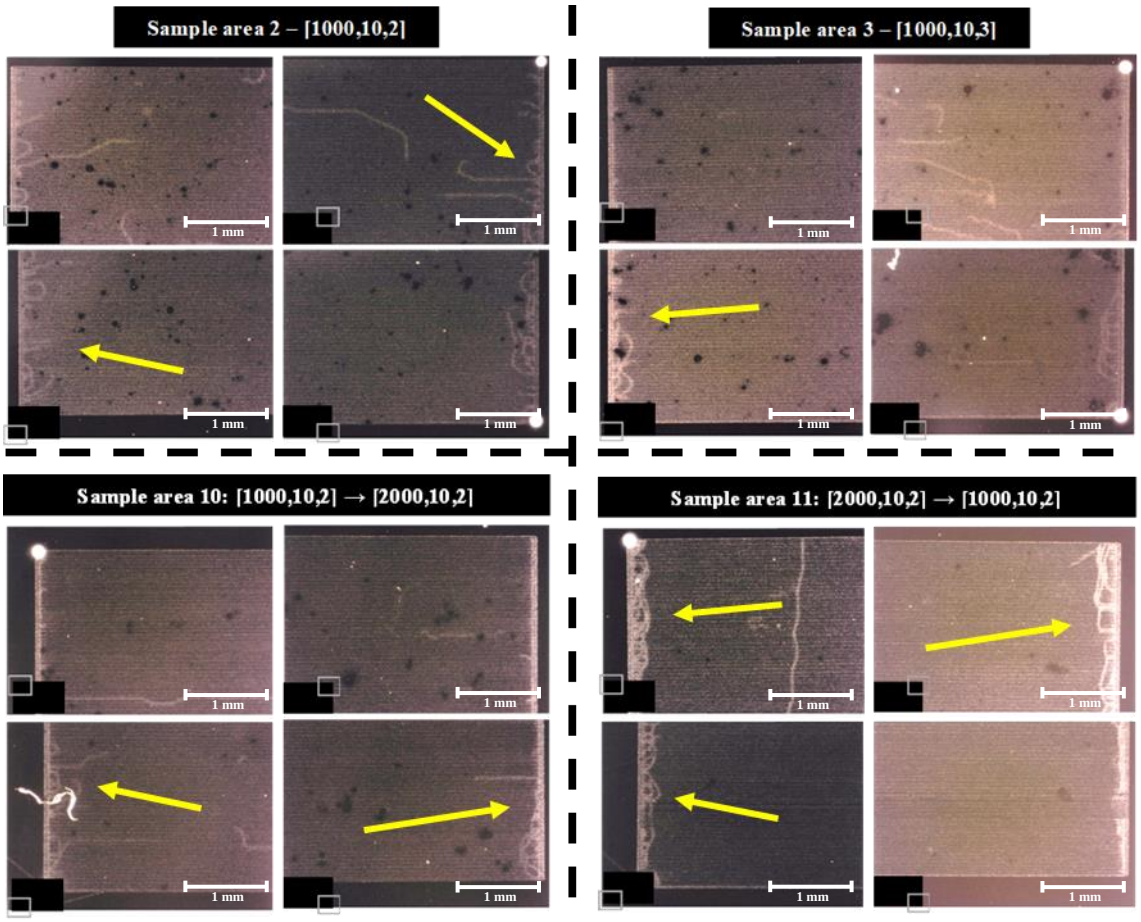

Figure 4.10. Enhanced micro-interaction on the border on the sample areas, when using quartz window.

4.4. Emitter

Using the p++/p+ wafer, the goal is to compare its melting profile with the standard wafer. As a heavily p-doped (p++) sample, the emitter is used to form a p-n junction in a solar cell structure. Since it is part of the goals of S-LoTTuSS project to form a n++/p++ tunnel junction directly on the silicon sub-cell in a solar cell tandem structure, it is of importance to understand how the laser interacts with a wafer with such a highly doped layer on top.

Analysing the results, we can see that the influence of the successive laser scan still affects the effectiveness of the laser interaction. Figure 4.11 shows the improvement of the second scan, which is represented by the blue two-edged arrows, representing the difference in the melted area, and by the red circles, showing the decrease in the poorly laser treated regions.

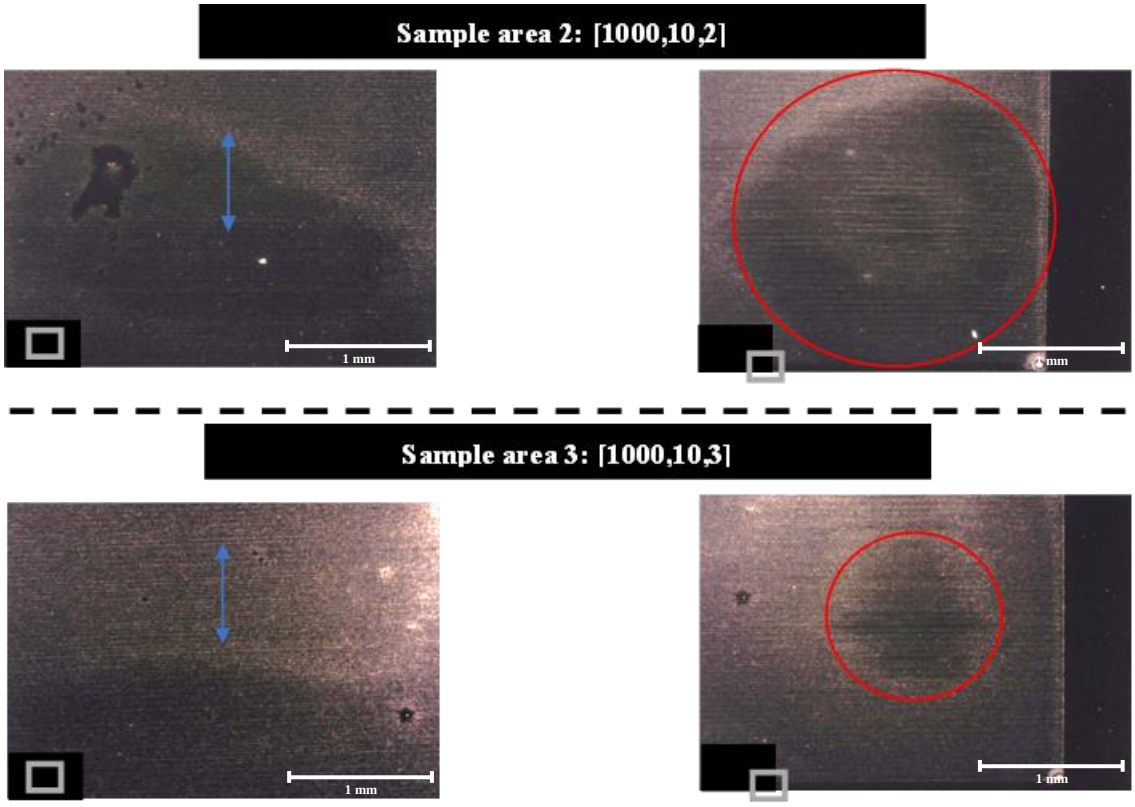

Figure 4.11. Improvement of successive scans on the emitter wafer.

It's also possible to state that all the sample areas on the emitter wafer have lower interaction than standard wafers. The result is a deficient melting profile, with dark regions and zones that successfully melted having low brightness, meaning that the interaction was very shallow. Comparing with the standard wafer while under the same set of parameters the difference in the melting homogeneity and effectiveness is notary. Even the region that was successful affected by the laser, presents lower brightness, which may indicate that the melting was not effective as in standard wafer (Figure 4.12).

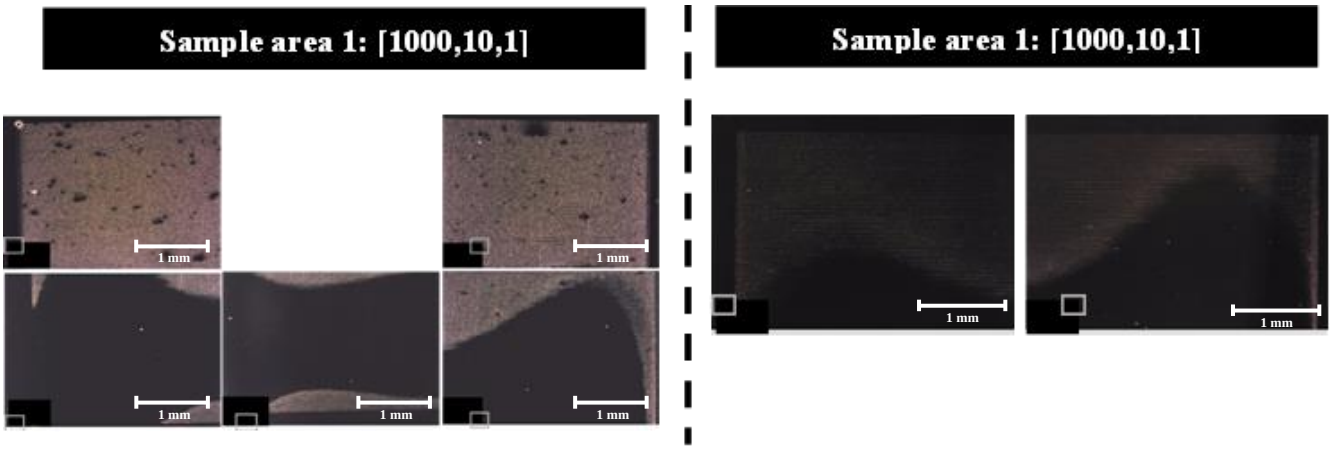

Figure 4.12. Comparison between a standard wafer (sample area on the left) and an emitter (sample area on the right) in laser-silicon interaction.

The other emitter sample areas show that for the set of parameters that presented deficient surface melting for the standard wafer, the laser interaction effectiveness. This information can be seen in the **Annex C**, where is the remaining results for the emitter wafer.

After comparing and analysing the results for the different types of wafers used (standard wafer and emitter), the lower laser interaction on the emitter was as expect. The reasons behind, could be associated with some factors, such has the high heat loss by conductivity due to its greater thickness. The high dopant levels (boron) in the p++ layer of the emitter, negatively affect the laser interaction. The reflectivity of the emitter wafer may also be an optical factor that affects the melting effectiveness.

4.5. SEM results

A topographic analysis of the wafer surface can demonstrate the melting homogeneity after the laser and silicon interaction. SEM results complements the previous optical microscopy results, which may help to understand the influence of the different parameters in a micron scale. For the standard wafer, it's easily identified the spacing between successive pulses (Figure 4.13). At lower scan speed (1000 mm/s) the distance between successive pulses is reduced, as presented in Table 4-1. Comparing with a faster scan speed, which is also associated with a longer distance between successive laser pulses, it's possible to verify that slower speed scans deposit more energy in the wafer since the bigger overlap frequency of the beam augments the laser interaction on the wafer surface. Observing Figure 4.13, it's verified that melting homogeneity is dependent to the laser scan speed.

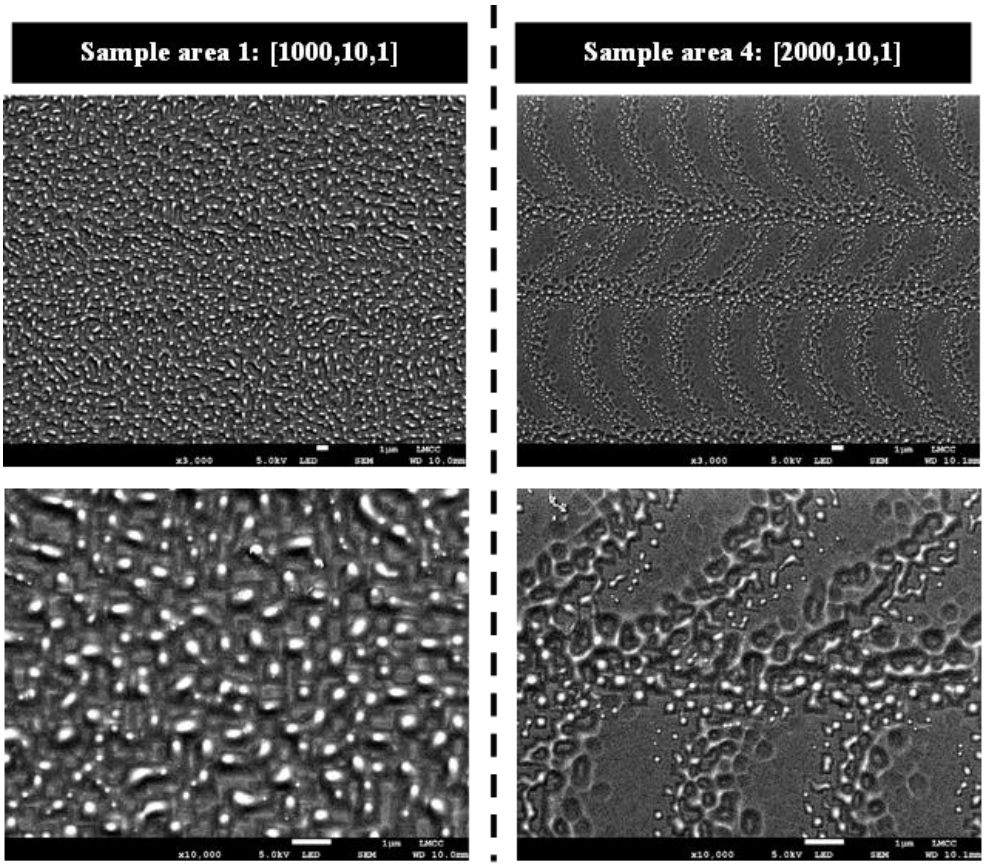

Figure 4.13. SEM results for the identified sample areas comparing the laser scan speed variations in different magnifications. Scale is identified with a white bar at the bottom of each image.

Even when increasing the number of laser scans, it's still observed the absence of laser interaction in between successive pulses. Observing Figure 4.13 and 4.14, it's verified that melting homogeneity is dependent to the laser scan speed.

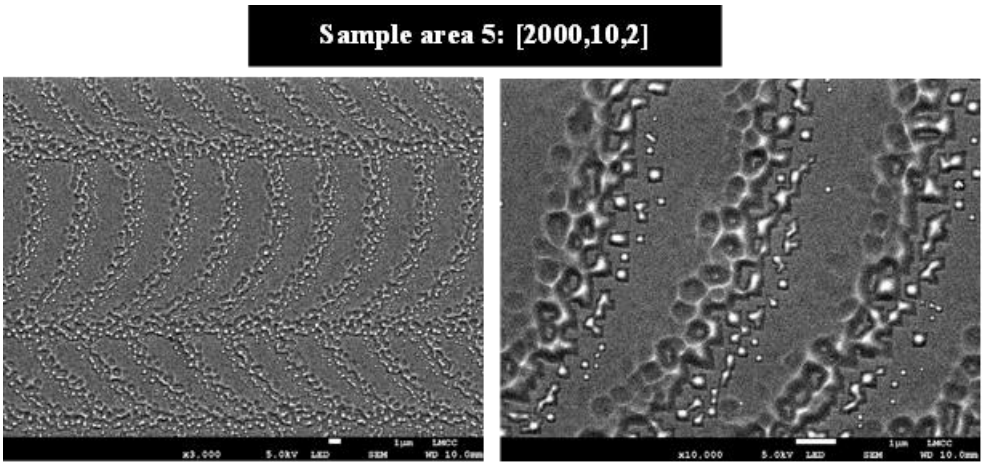

Figure 4.14. SEM results associated with the ineffective laser-silicon interaction, at an increased laser scan speed (2000 mm/s) and two scans.

Comparing the SEM results between standard wafer and emitter, it's perceivable that there is a big difference in each laser interaction. Seems that the surface of the emitter after the laser scan, maintains some of its surface smoothness. The melting occurs but in a very shallow heterogenous form (Figure 4.15). Supporting the statement said before, which indicates that the standard wafer displays a higher effectiveness when scattered by a pulsed laser.

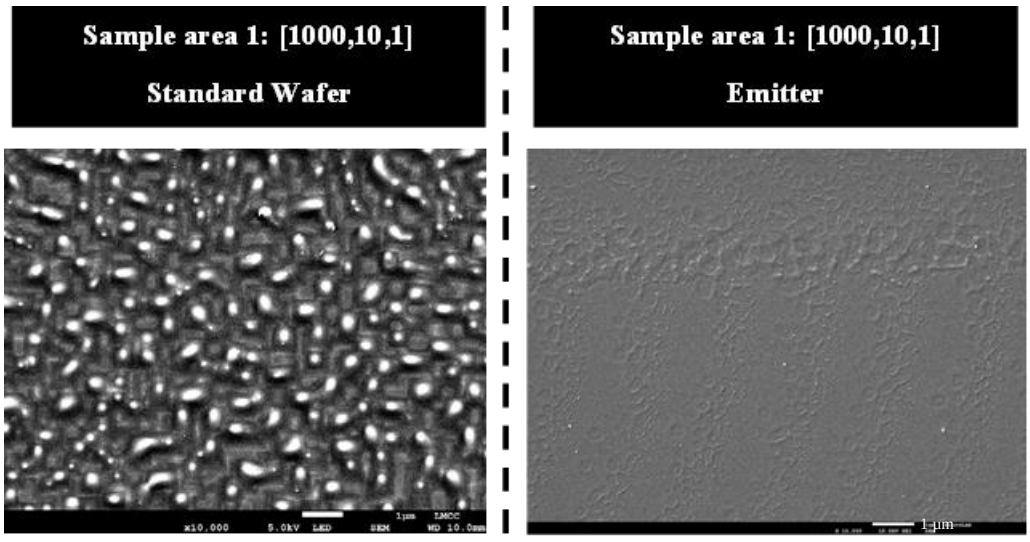

Figure 4.15. SEM results comparing the laser interaction between both types of wafers used.

5. Conclusions

The laser and silicon interaction when varying the setup details, the sample specimen and the parameters used in the scanning process were the indicators studied for this dissertation. The goal was to obtain sample areas with a fully homogenous interaction which is associated with an effective surface melting, material ablation or a mixture of both.

The new chamber presented better conditions to confine the sample since its leak rate was minimum when compared to the old chamber. It's complex design, robustness and sealing power provides a more controllable atmosphere for the experiments. The choice of using the old chamber was to preserve the new one for the future laser doping process using $POCl_3$. It is conclusive that the quartz window foments a better laser-silicon interaction than the polycarbonate window, contributing to a more homogenous surface treatment. The lower transmittance on the polycarbonate window delays the initial laser pulsed beam to focus directly on the sample surface.

The standard wafer (p-type Czochralski-Silicon wafer) is the sample specimen that has shown to have a better laser interaction than the emitter (p++/p+ Czochralski-Silicon wafer). In this wafer, every sample area presents a good and homogenous interaction, without dark regions or non-treated zones. These results are mostly related with the low heat loss by conductivity due to the standard wafer lower thickness and the low p-dopant concentration (10^{15} cm^{-3}).

After analysing the different parameters set combinations, it is possible to state that the effectiveness of the laser interaction is related with a slower laser scan, a smaller distance between the centre of two consecutive horizontal paths (*d*) and more laser scan consecutive repetitions. The variable that most influents the homogeneity of the surface melting is the number of laser scans. Even for a low-speed beam process of the laser, stills appear the dark regions that are associated with no interaction, which are only corrected with the successive laser scans. Then, increasing the number of scans will mitigate the unsuccessful interacted regions. Also, it is important to avoid the over-processing of the sample, since it is aimed to estimate the parameters combination that can lead to laser doping if a gas containing dopant is involved. The dopant atoms should be incorporated in the molten silicon at a shallow depth (the first tens of nanometres). The parameter *d* is the variable that less affects the overall melting of the sample surface. A lower distance (10 µm) is more impactful for a nanometre scale melting homogeneity since the distance between the rows created by the laser paths are smaller. Thus, it increases the total area that suffers interaction.

The SEM results has shown complementary conclusions to the optical microscope analysis. It clearly shows the impact of the laser scan speed, which proves that laser interaction homogeneity is affected by slower scans. Also, in SEM we can observe that it indicates the potential laser ablation of the samples surface.

To finalize, the experiments that were made are considered highly temperature dependant, especially the initial temperature of the sample, and highly optical precision, since there are nano-interactions that take place between the laser beam and the impurities that lays on the window surface or upon the sample. For future studies, the pre-heating of the surface, for example, heating with an elevated temperature air recirculation, or with an oven to increase the temperature of the wafer before starting the experiment could maximize the initial interaction. To minimize the impurities on the surfaces, an etching with HF could minimize the oxides and impurities that lays on the surfaces of the sample and the window.

6. Bibliography

[**1**] "What is the source of the electricity we consume?" [Online] Available:https://ec.europa.eu/eurostat/cache/infographs/energy/bloc-3b.html Source: Eurostat, [visited 19/01/2020]

[**2**] Šúri, M., Huld, T. A., Dunlop, E. D., & Ossenbrink, H. A. (2007). Potential of solar electricity generation in the European Union member states and candidate countries. *Solar Energy*, *81*(10), 1295–1305. https://doi.org/10.1016/j.solener.2006.12.007

[**3**] Wronski, C. R., Pearce, J. M., Deng, J., Vlahos, V., & Collins, R. W. (2004). Intrinsic and light induced gap states in a-Si:H materials and solar cells - Effects of microstructure. *Thin Solid Films*, *451–452*, 470–475. https://doi.org/10.1016/j.tsf.2003.10.129

[**4**] Hegedus, S. (2003). Photovoltaic Science. In *Energy*.

[**5**] Bailie, C. D., & McGehee, M. D. (2015). High-efficiency tandem perovskite solar cells. *MRS Bulletin*, *40*(8), 681–685. https://doi.org/10.1557/mrs.2015.167

[**6**] Köhnen, E., Jošt, M., Morales-Vilches, A. B., Tockhorn, P., Al-Ashouri, A., Macco, B., Kegelmann, L., Korte, L., Rech, B., Schlatmann, R., Stannowski, B., & Albrecht, S. (2019). Highly efficient monolithic perovskite silicon tandem solar cells: Analyzing the influence of current mismatch on device performance. *Sustainable Energy and Fuels*, *3*(8), 1995–2005. https://doi.org/10.1039/c9se00120d

[**7**] Zaidi, B. (2018). Introductory Chapter: Introduction to Photovoltaic Effect. *Solar Panels and Photovoltaic Materials*, 1–8. https://doi.org/10.5772/intechopen.74389

[**8**] Gueymard, C. A. (2004). The sun's total and spectral irradiance for solar energy applications and solar radiation models. *Solar Energy*, *76*(4), 423–453. https://doi.org/10.1016/j.solener.2003.08.039

[**9**] Bikaneria, J., Prakash Joshi, S., Joshi, A., Service Manager, A., & trucking, K. (2013). Modeling and Simulation of PV Cell using One-diode model. *International Journal of Scientific and Research Publications*, *3*(10), 2250–3153. www.ijsrp.org

[**10**] Rodrigues, E. M. G., Melício, R., Mendes, V. M. F., & Catalão, J. P. S. (2011). Simulation of a solar cell considering single-diode equivalent circuit model. *Renewable Energy and Power Quality Journal*, *1*(9), 369–373. https://doi.org/10.24084/repqj09.339

[**11**] Zaidi, B., Saouane, I., & Shekhar, C. (2018). *Simulation of Single-Diode Equivalent Model of Polycrystalline Silicon Solar Cells*. *7*(January), 8–10. https://doi.org/10.11648/j.ijmsa.s.2018070101.12

[**12**] Shockley, W., & Queisser, H. J. (1961). Detailed balance limit of efficiency of p-n junction solar cells. *Journal of Applied Physics*, *32*(3), 510–519. https://doi.org/10.1063/1.1736034

[**13**] GREEN, M., EMERY, K., HISHIKAWA, Y., WARTA, W., DUNLOP, E., BARKHOUSE, D., GUNAWAN, O., GOKMEN, T., TODOROV, T., & MITZI, D. (2012). Solar cell efficiency tables (version 40). *Ieee Trans Fuzzy Syst*, *20*(6), 1114–1129. https://doi.org/10.1002/pip

[**14**] Alajlani, Y., Alaswad, A., Placido, F., Gibson, D., & Diyaf, A. (2018). Inorganic Thin Film Materials for Solar Cell Applications. In *Reference Module in Materials Science and Materials Engineering* (Vol. 7). Elsevier Ltd. https://doi.org/10.1016/b978-0-12-803581-8.10355-8

[**15**] Tmoco, T., Quintero, M., & Sanchez, G. (1991). *Phase Diagram and Optical Energy Gaps for CuIn,Ga, - ,Se, Alloys*. *427*.

[**16**] Fan, Z., Sun, K., & Wang, J. (2015). Perovskites for photovoltaics: a combined review of organic-inorganic halide perovskites and ferroelectric oxide perovskites. *Journal of Materials Chemistry A*, *3*(37), 18809–18828. https://doi.org/10.1039/c5ta04235f

[**17**] Qiu, L., Ono, L. K., & Qi, Y. (2018). Advances and challenges to the commercialization of organic–inorganic halide perovskite solar cell technology. *Materials Today Energy*, *7*, 169–189. https://doi.org/10.1016/j.mtener.2017.09.008

[**18**] Rühle, S. (2016). Tabulated values of the Shockley-Queisser limit for single junction solar cells. *Solar Energy*, *130*, 139–147. https://doi.org/10.1016/j.solener.2016.02.015

[**19**] ISE, P. R. I. F. O. R. S. E. S. *Photovoltaics Report*. *July 2021*.

[**20**] Kerr, M. J., Cuevas, A., & Campbell, P. (2003). Limiting efficiency of crystalline silicon solar cells due to Coulomb-enhanced Auger recombination. *Progress in Photovoltaics: Research and Applications*, *11*(2), 97–104. https://doi.org/10.1002/pip.464

[**21**] Richter, A., Hermle, M., & Glunz, S. W. (2013). Reassessment of the limiting efficiency for crystalline silicon solar cells. *IEEE Journal of Photovoltaics*, *3*(4), 1184–1191. https://doi.org/10.1109/JPHOTOV.2013.2270351

[**22**] Zheng, J., Mehrvarz, H., Ma, F. J., Lau, C. F. J., Green, M. A., Huang, S., & Ho-Baillie, A. W. Y. (2018). 21.8% Efficient Monolithic Perovskite/Homo-Junction-Silicon Tandem Solar Cell on 16 cm2. *ACS Energy Letters*, *3*(9), 2299–2300. https://doi.org/10.1021/acsenergylett.8b01382

[**23**] Mueller, T., Schwertheiml, S., Muellerl, N., Meusinger, K., Wdowiakl, B., Grewel, O., & Fahrner, W. (2010). High efficiency silicon heterojunction solar cell using novel structure. *Conference Record of the IEEE Photovoltaic Specialists Conference*, 683–688. https://doi.org/10.1109/PVSC.2010.5616901

[**24**] Mueller, T., Schwertheiml, S., Muellerl, N., Meusinger, K., Wdowiakl, B., Grewel, O., & Fahrner, W. (2010). High efficiency silicon heterojunction solar cell using novel structure. *Conference Record of the IEEE Photovoltaic Specialists Conference*, 683–688. https://doi.org/10.1109/PVSC.2010.5616901

[**25**] Gaspar G, Guerra A, Cardoso JC, Costa I, Vilhena D, Pera D, Silva J, Serra JM, Vallêra AM, & Lobato K. (2020). Interconexão entre células solares de perovskita e silício em dispositivos monolíticos tandem de 2 terminais: Estado da arte e desenvolvimentos futuros. *CIES2020 - XVII Congresso Ibérico e XIII Congresso Ibero-Americano de Energia Solar*, 413–419. https://doi.org/10.34637/cies2020.1.2047

[**26**] Fave, A., Lelièvre, J. F., Gallet, T., Su, Q., & Lemiti, M. (2017). Fabrication of Si tunnel diodes for c-Si based tandem solar cells using proximity rapid thermal diffusion. *Energy Procedia*, *124*, 577–583. https://doi.org/10.1016/j.egypro.2017.09.281

[**27**] Gaspar, G., Guerra, A., Serra, F. C., Viana, A. S., Arumughan, J., Costa, I., Pêra, D. M., Silva, J. A., Vines, L., Serra, J. M., Lobato, K. (2021). Tunnel Juction Formation On Silicon p++ emitters by gas immersion laser doping. https://doi.org/10.4229/EUPVSEC20212021-3BV.2.68

[**28**] Werner, J., Barraud, L., Walter, A., Bräuninger, M., Sahli, F., Sacchetto, D., Tétreault, N., Paviet-Salomon, B., Moon, S. J., Allebé, C.,Despeisse, M., Nicolay, S., De Wolf, S., Niesen, B., & Ballif, C. (2016). Efficient Near-Infrared-Transparent Perovskite Solar Cells Enabling Direct Comparison of 4-Terminal and Monolithic Perovskite/Silicon Tandem Cells. *ACS Energy Letters*, *1*(2), 474–480. https://doi.org/10.1021/acsenergylett.6b00254

[**29**] De Bastiani, M., Subbiah, A. S., Aydin, E., Isikgor, F. H., Allen, T. G., & De Wolf, S. (2020). Recombination junctions for efficient monolithic perovskite-based tandem solar cells: Physical principles, properties, processing and prospects. *Materials Horizons*, *7*(11), 2791–2809. https://doi.org/10.1039/d0mh00990c

[30] Yamaguchi, M., Lee, K. H., Araki, K., & Kojima, N. (2018). A review of recent progress in heterogeneous silicon tandem solar cells. *Journal of Physics D: Applied Physics*, *51*(13). https://doi.org/10.1088/1361-6463/aaaf08

[**31**] De Vos, A. (1980). Detailed balance limit of the efficiency of tandem solar cells. *Journal of Physics D: Applied Physics*, *13*(5), 839–846. https://doi.org/10.1088/0022-3727/13/5/018

[**32**] Hossain, M. I., Qarony, W., Ma, S., Zeng, L., Knipp, D., & Tsang, Y. H. (2019). Perovskite/Silicon Tandem Solar Cells: From Detailed Balance Limit Calculations to Photon Management. *Nano-Micro Letters*, *11*(1), 1–24. https://doi.org/10.1007/s40820-019-0287-8

[**33**] Esaki, L. (1958). New phenomenon in narrow germanium p-n junctions. *Physical Review*, *109*(2), 603–604. https://doi.org/10.1103/PhysRev.109.603

[**34**] Erol Sağol, B., Seidel, U., Szabó, N., Schwarzburg, K., & Hannappel, T. (2007). Basic concepts and interfacial aspects of high-efficiency III-V multijunction solar cells. *Chimia*, *61*(12), 775–779. https://doi.org/10.2533/chimia.2007.775

[**35**] Zhang, X., Gong, L., Wu, B., Zhou, M., & Dai, B. (2015). Characteristics and value enhancement of cast silicon ingots. *Solar Energy Materials and Solar Cells*, *139*, 27–33. https://doi.org/10.1016/j.solmat.2015.03.007

[**36**] Laboratories, S. E., P.G.Carey, & T.W.Sigmon. (1989). *In-Situ Doping of Silicon Using The Gas Immersion Laser Doping (GILD) Process*. *43*, 325–332

[**37**] Cammilleri, D., Fossard, F., Débarre, D., Tran Manh, C., Dubois, C., Bustarret, E., Marcenat, C., Achatz, P., Bouchier, D., & Boulmer, J. (2008). Highly doped Si and Ge formed by GILD (gas immersion laser doping); from GILD to superconducting silicon. *Thin Solid Films*, *517*(1), 75–79. https://doi.org/10.1016/j.tsf.2008.08.073

[**38**] Kerrien, G., Boulmer, J., Débarre, D., Bouchier, D., Grouillet, A., & Lenoble, D. (2002). Ultra-shallow, super-doped and box-like junctions realized by laser-induced doping. *Applied Surface Science*, *186*(1–4), 45–51. https://doi.org/10.1016/S0169-4332(01)00623-7

[**39**] Geográfica, D. D. E. E., Energia, G. E., & Guerra, A. (2020). *Fabrico de junções de túnel para células solares de dupla junção de alto rendimento Afonso Filipe Diogo Guerra*

[**40**] Landi, E., Carey, P. G., & Sigmon, T. W. (1988). Numerical Simulation of the Gas Immersion Laser Doping (GILD) Process in Silicon. *IEEE Transactions on Computer-Aided Design of Integrated Circuits and Systems*, *7*(2), 205–214. https://doi.org/10.1109/43.3150

[**41**] Vareiro, R. M. C. S. (2020). *Development of a sample holder for electrochemical capacitance-voltage dopant profiling in silicon wafers*.

[**42**] Micha, D. N., Penello, G. M., Kawabata, R. M. S., & Camarotti, T. (2011). "Vendo o invisível". Experimentos de visualização do infravermelho feitos com materiais simples e de baixo custo. *Revista Brasileira de Ensino de Fisica*, *33*(1), 1–6. https://doi.org/10.1590/S1806-11172011000100015

[**43**] Kamath, G. S., Ewan, J., & Knechtli, R. C. (1977). Large-Area High-Efficiency (AlGa)As—GaAs Solar Cells. *IEEE Transactions on Electron Devices*, *ED-24*(4), 473–475. https://doi.org/10.1109/T-ED.1977.18761

7. Annex

7.1. Annex A – Standard wafer using polycarbonate window (2020-12-21)

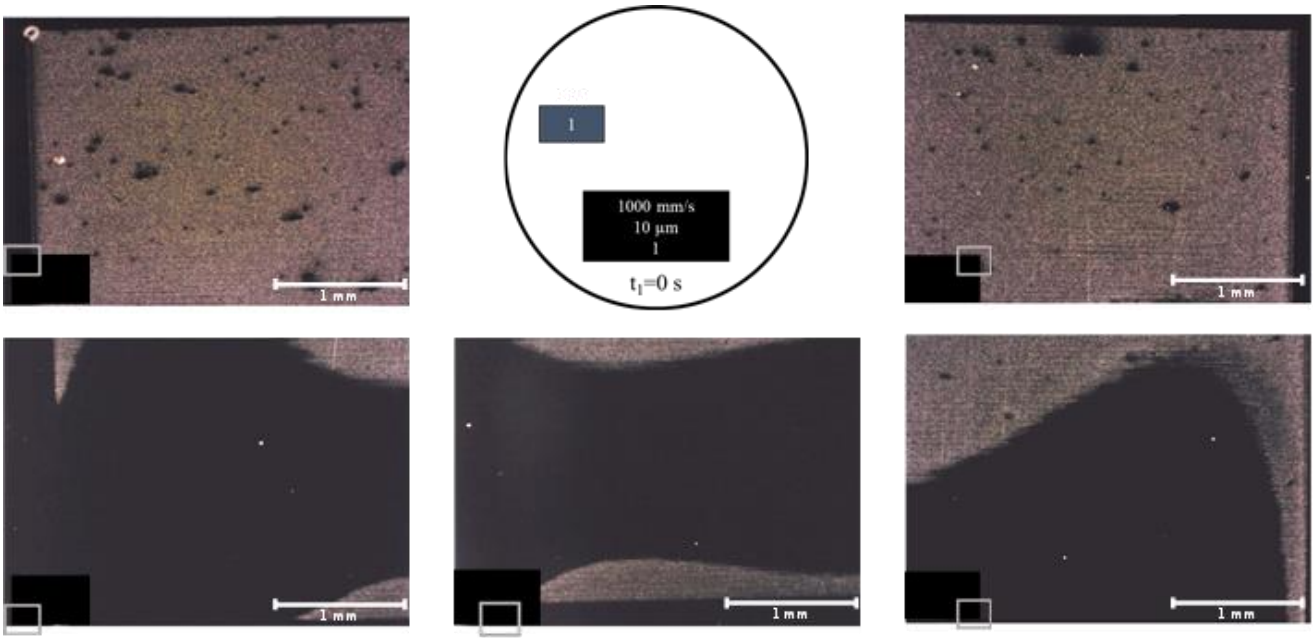

Figure 7.1. Sample area 1.

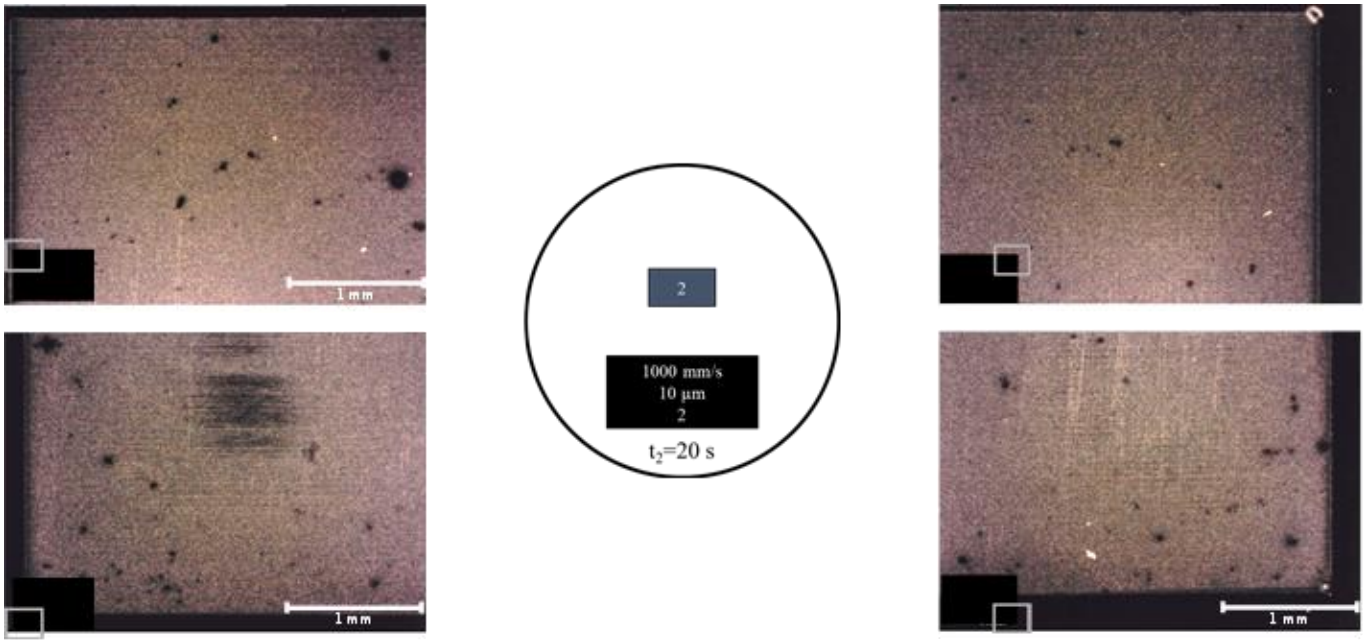

Figure 7.2. Sample area 2.

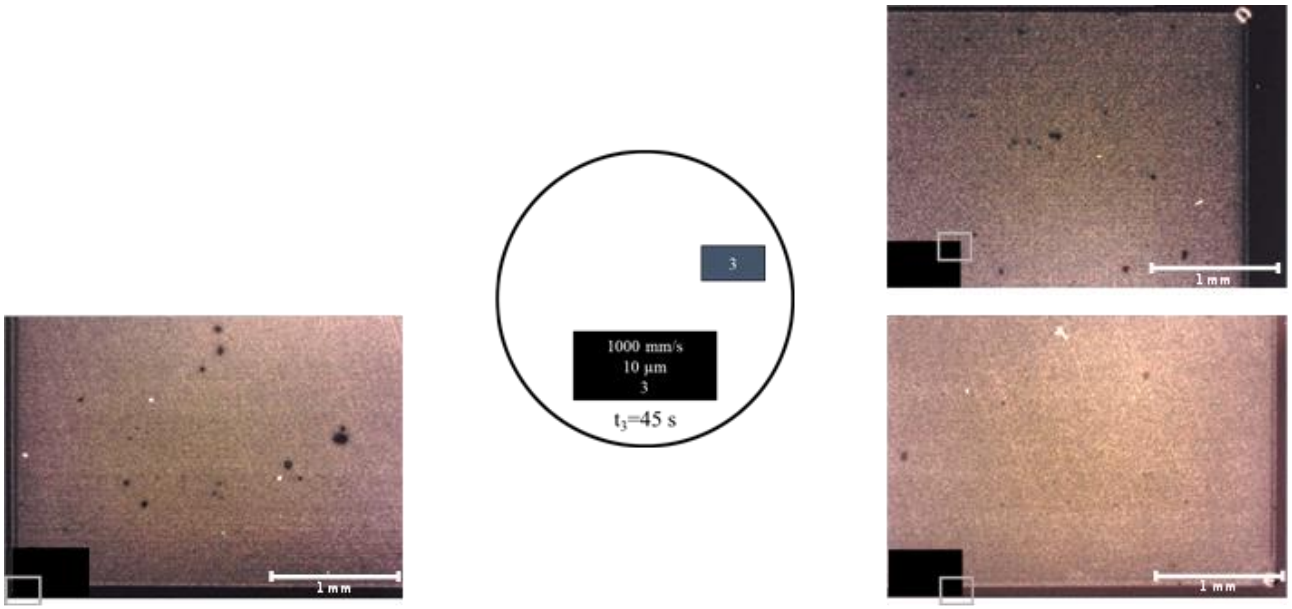

Figure 7.3. Sample area 3. The top left corner was not registered.

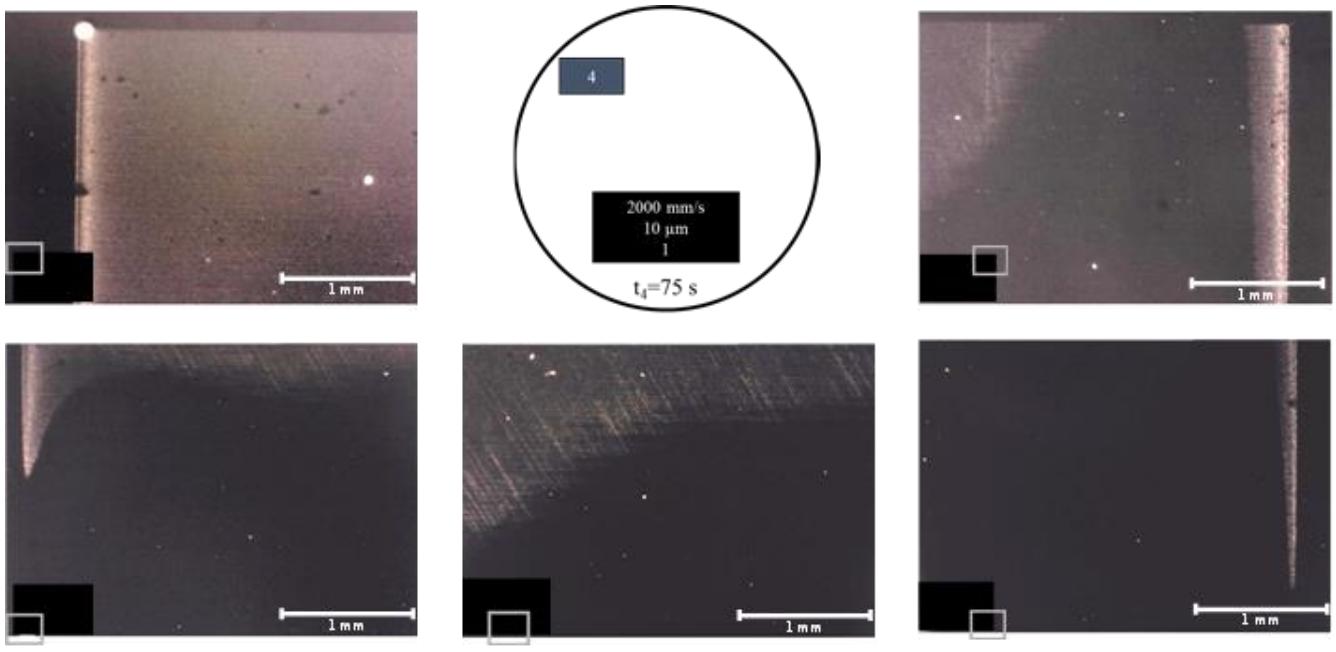

Figure 7.4. Sample area 4.

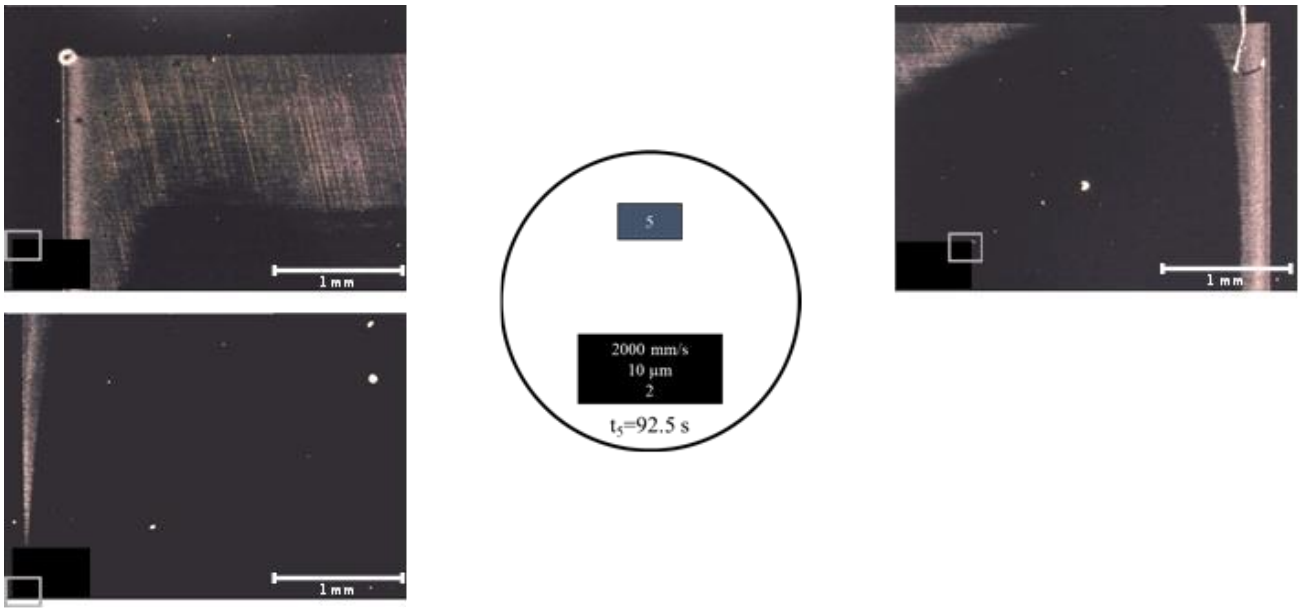

Figure 7.5. Sample area 5. The bottom right corner was not registered.

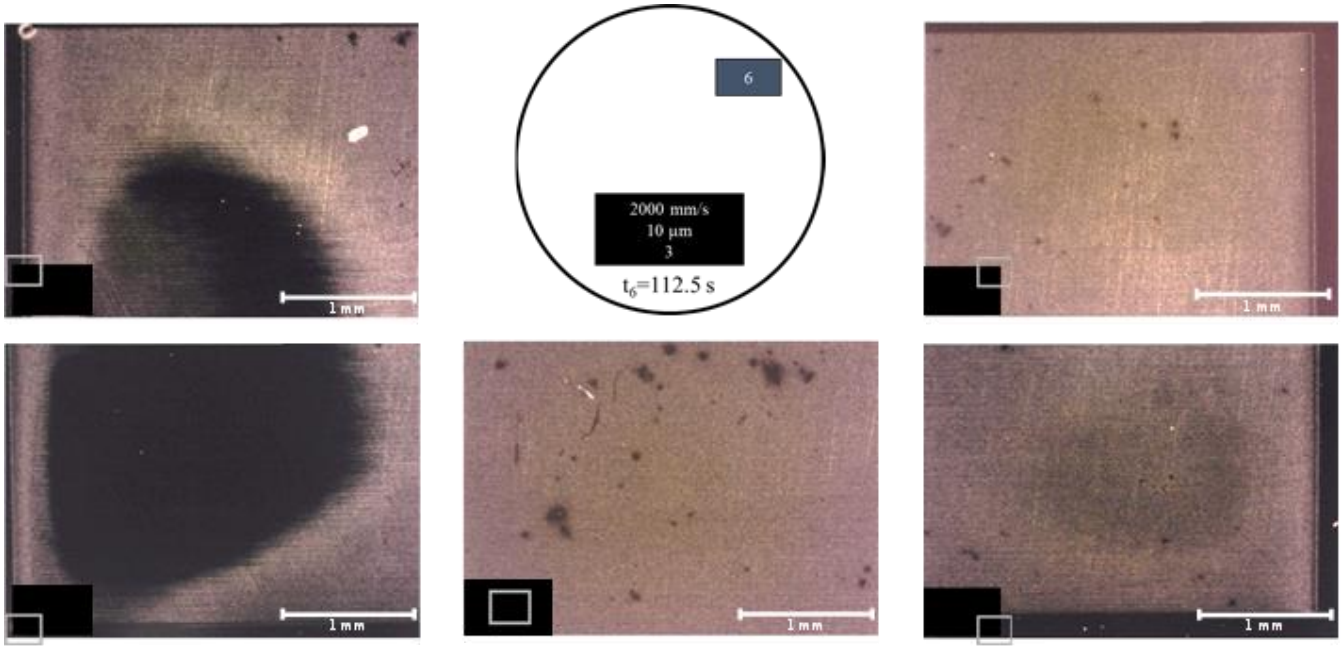

Figure 7.6. Sample area 6.

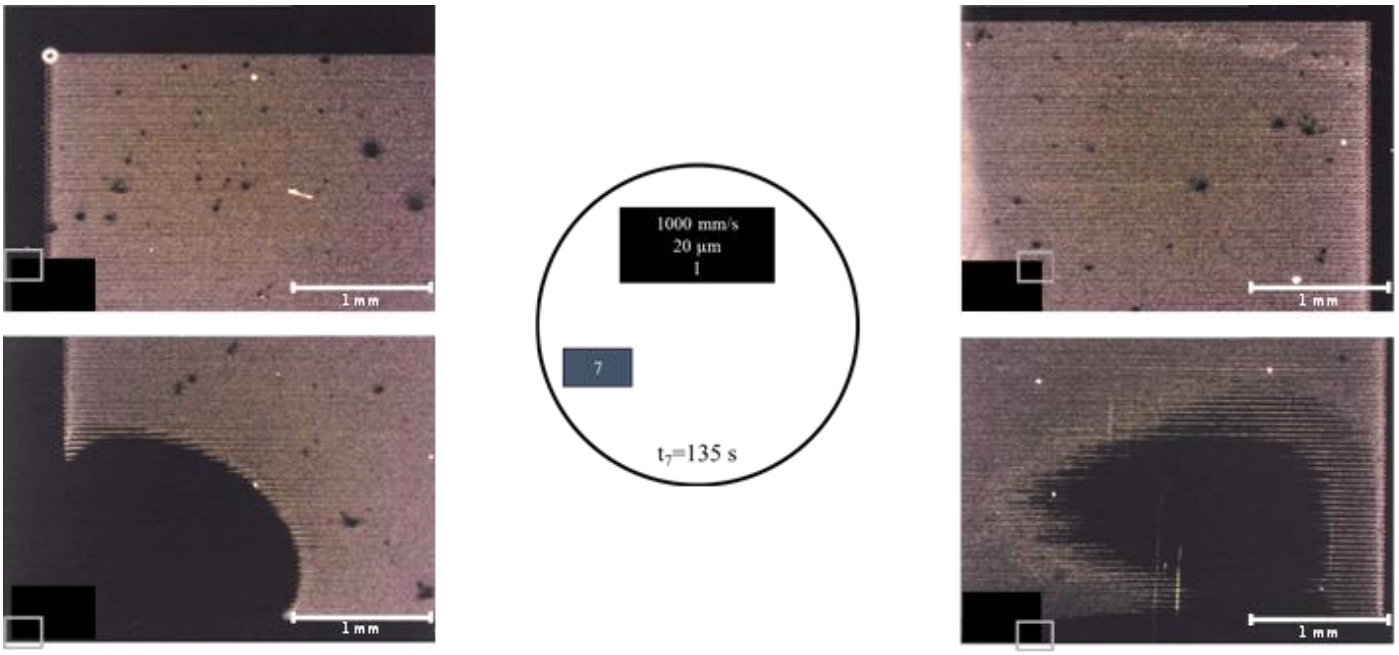

Figure 7.7. Sample area 7.

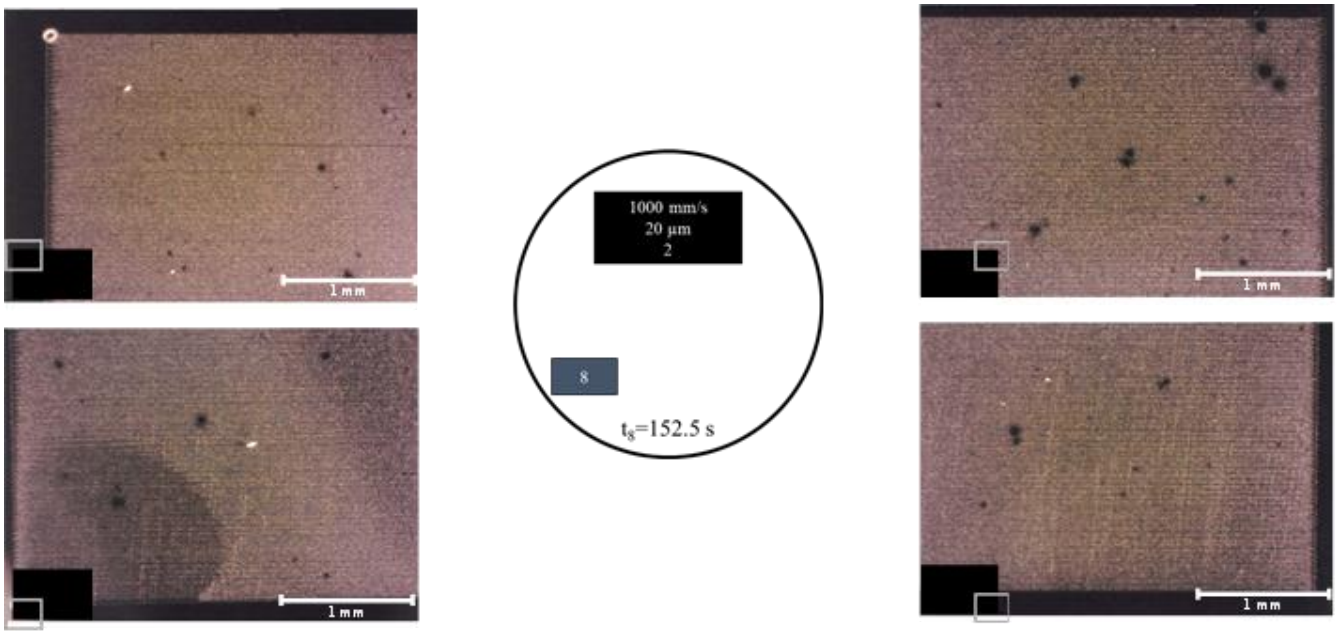

Figure 7.8. Sample area 8.

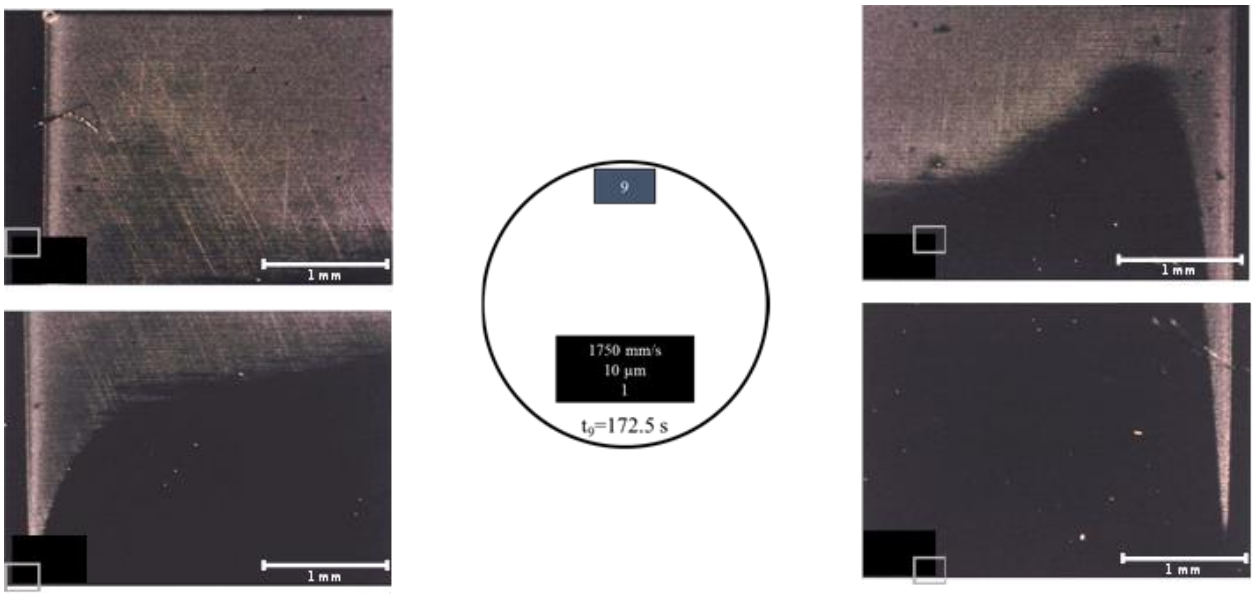

Figure 7.9. Sample area 9.

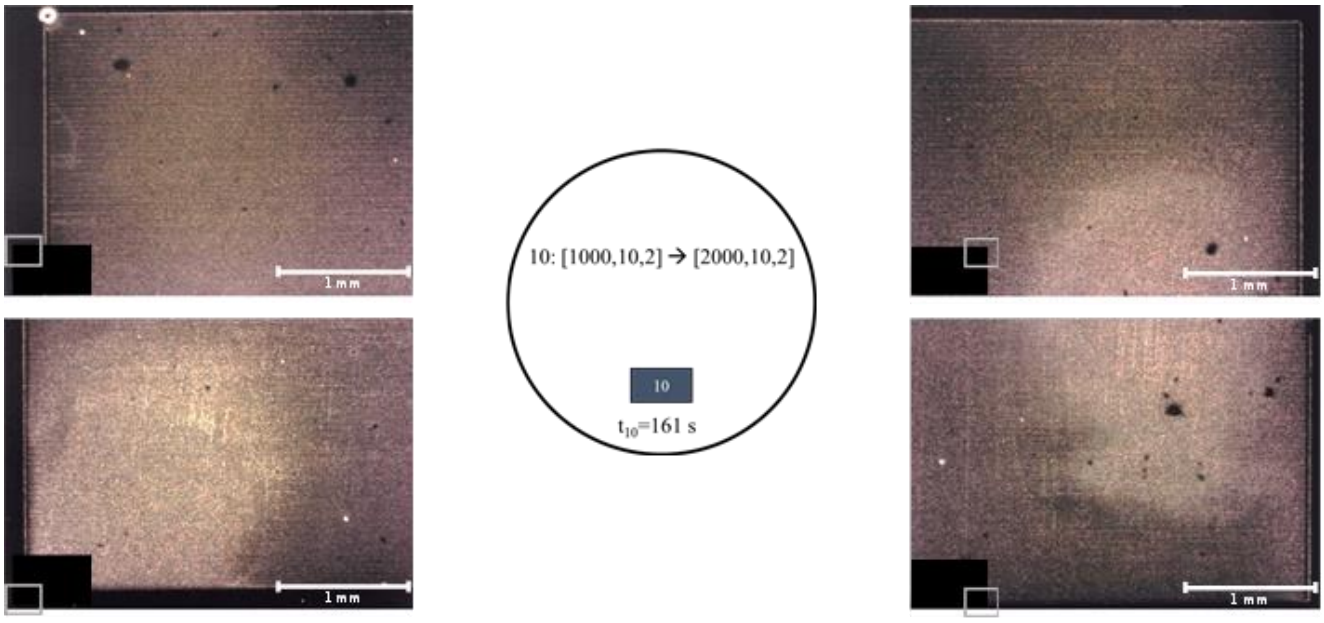

Figure 7.10. Sample area 10.

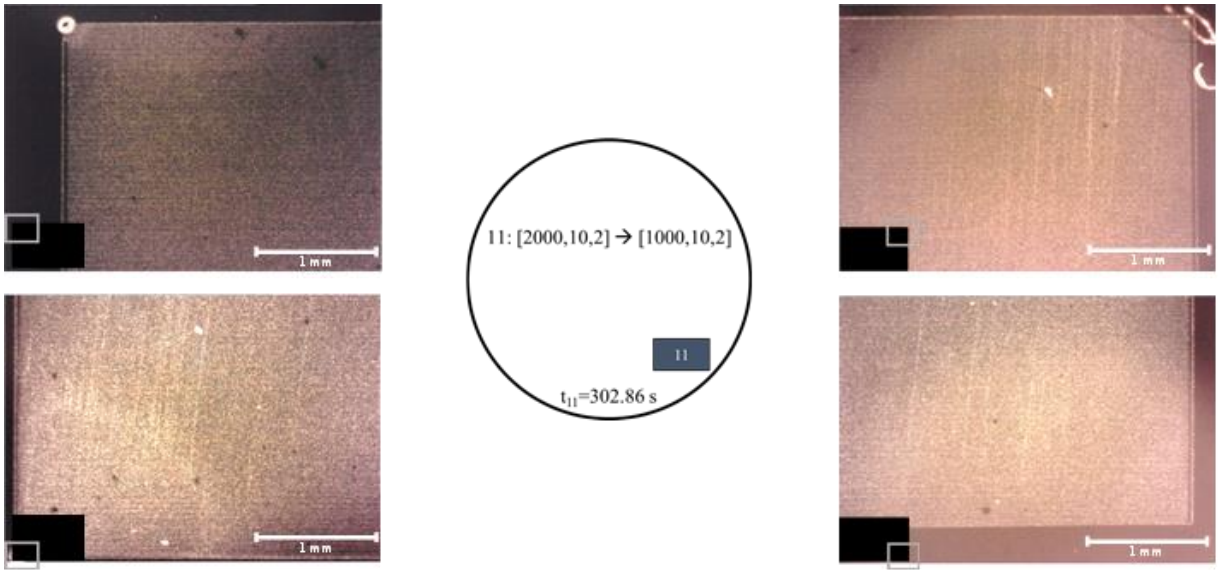

Figure 7.11. Sample area 11.

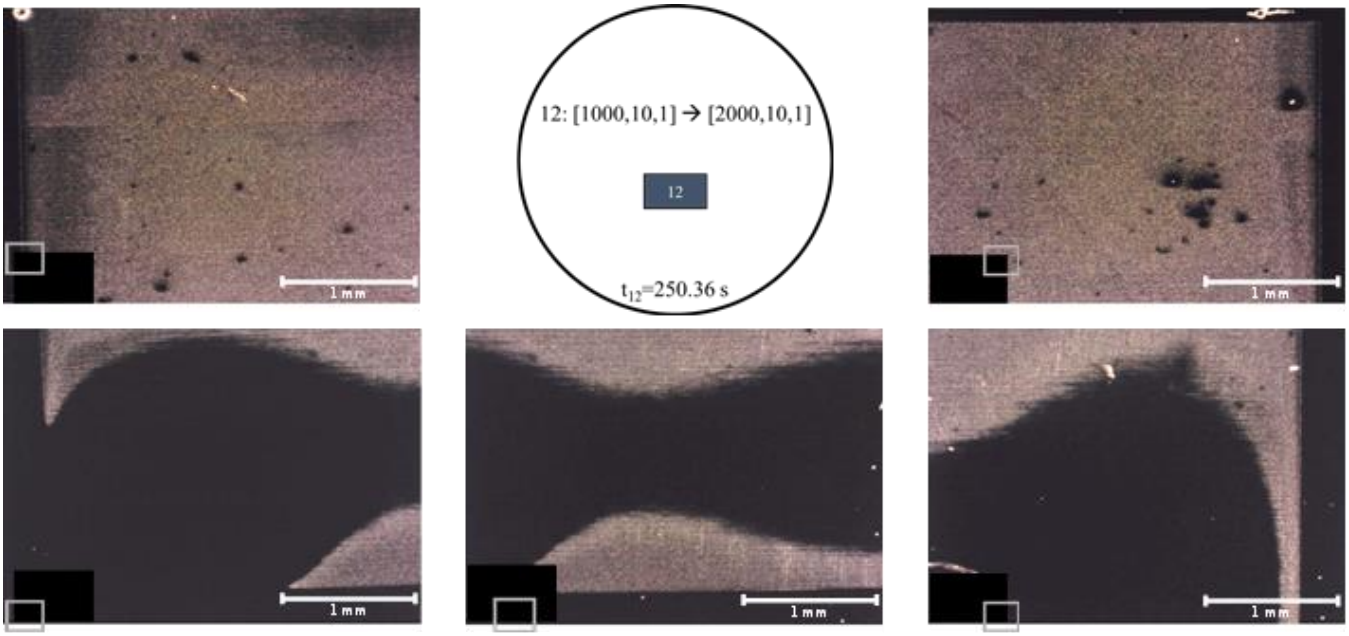

Figure 7.12. Sample area 12.

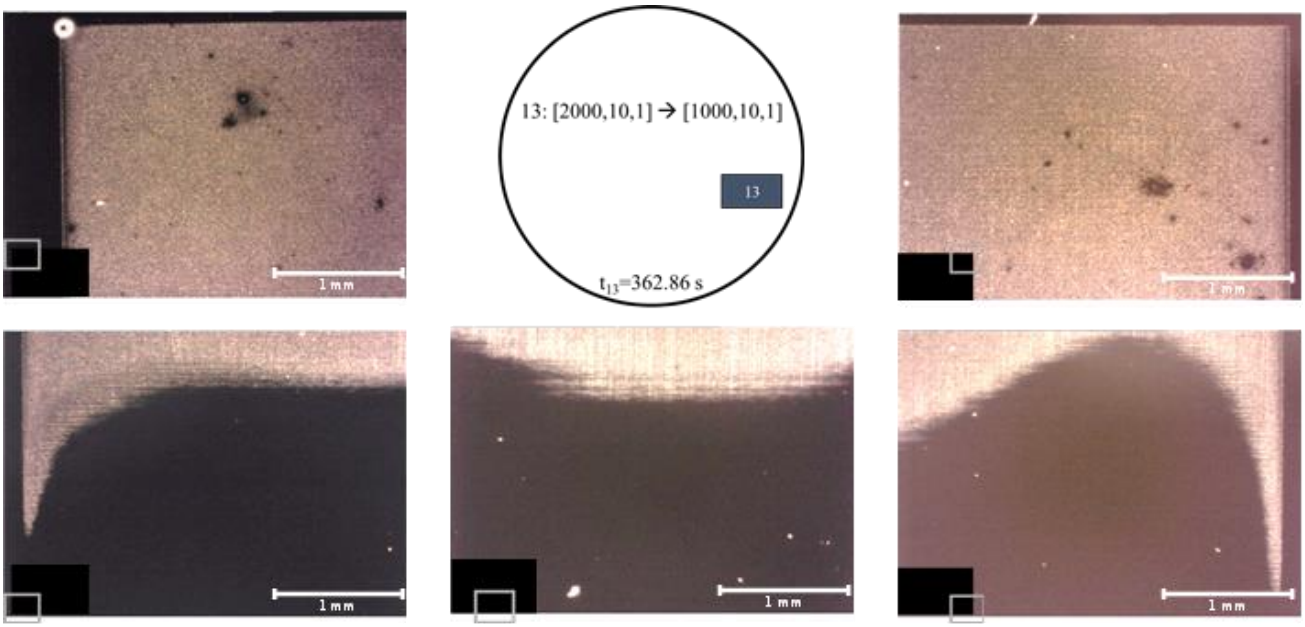

Figure 7.13. Sample area 13.

7.2. Annex B – Standard wafer using Quartz window

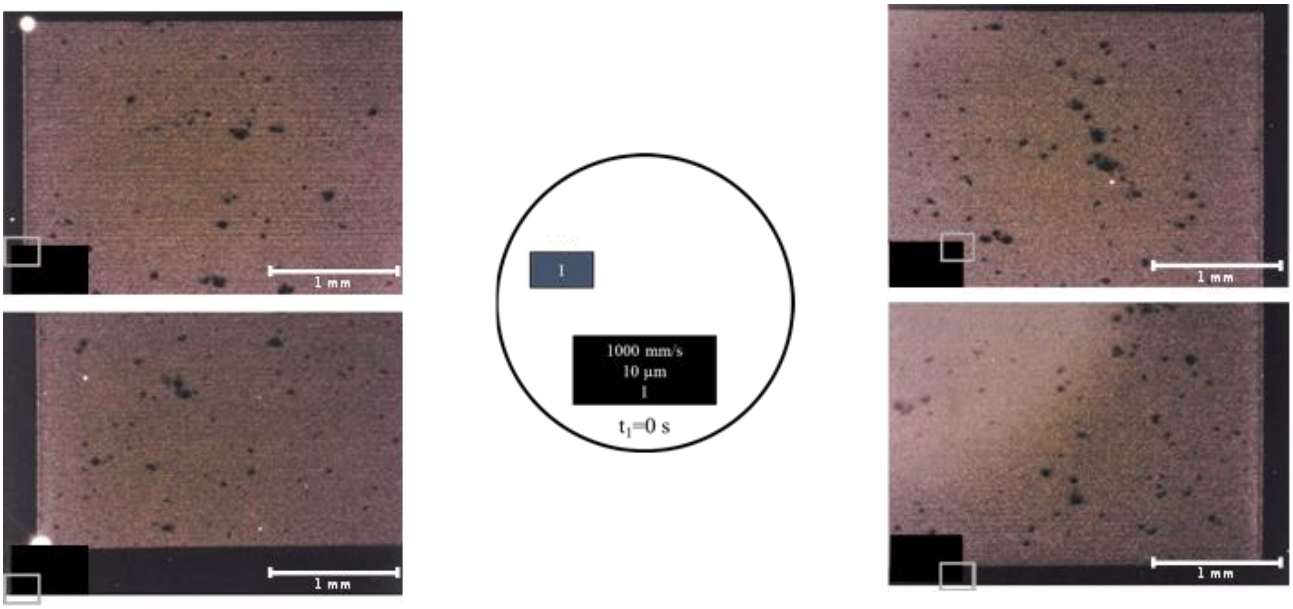

Figure 7.14. Sample area 1.

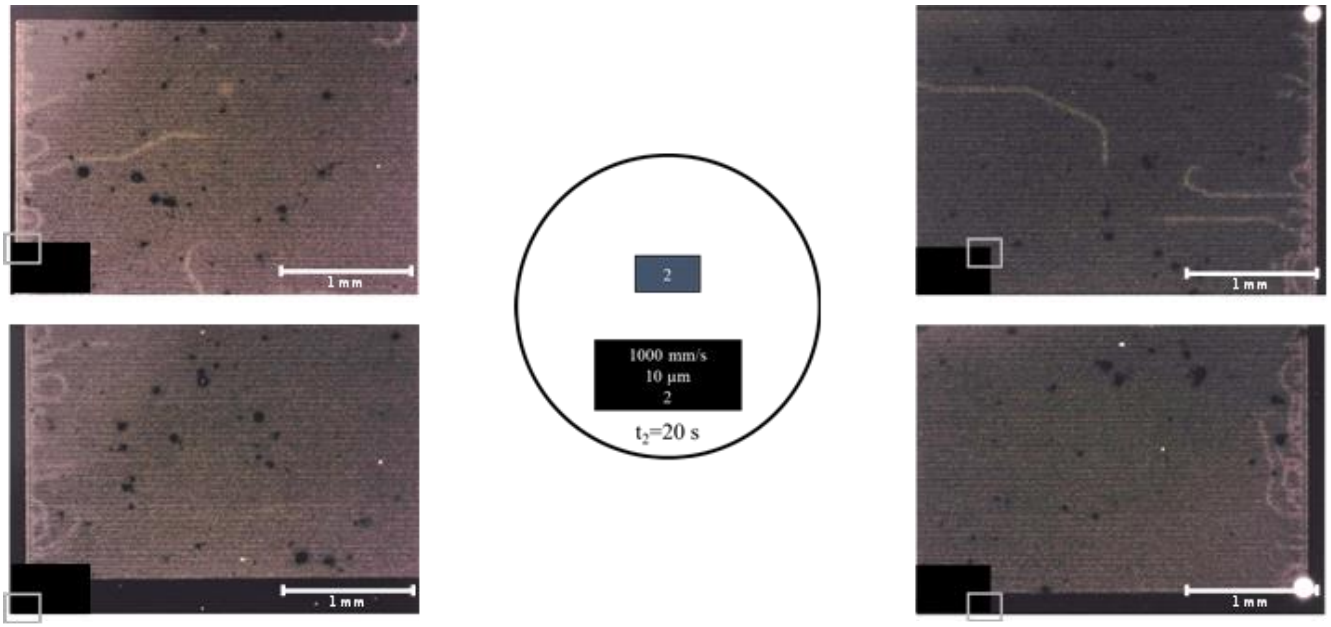

Figure 7.15. Sample area 2.

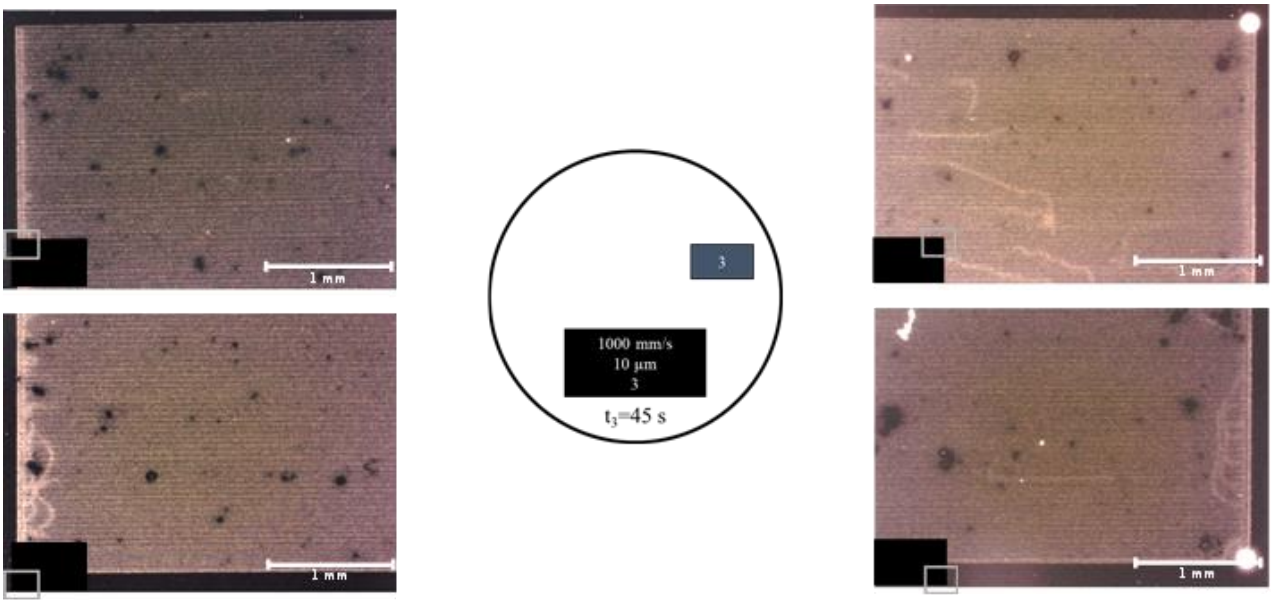

Figure 7.16. Sample area 3.

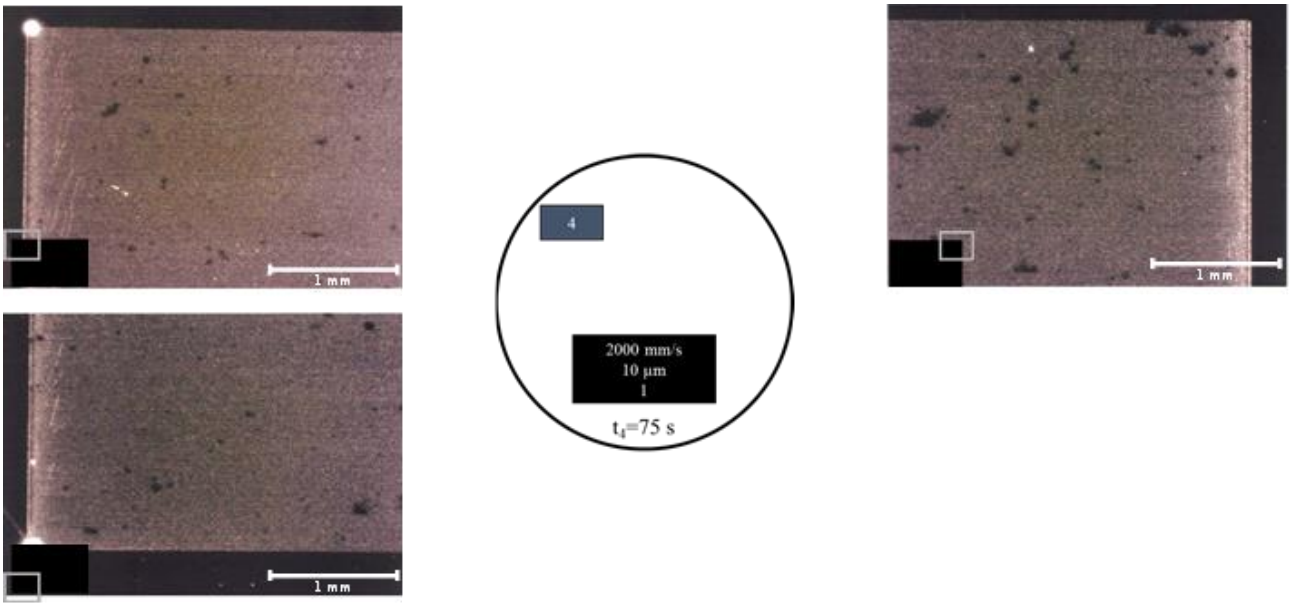

Figure 7.17. Sample area 4. The bottom right corner was not registered.

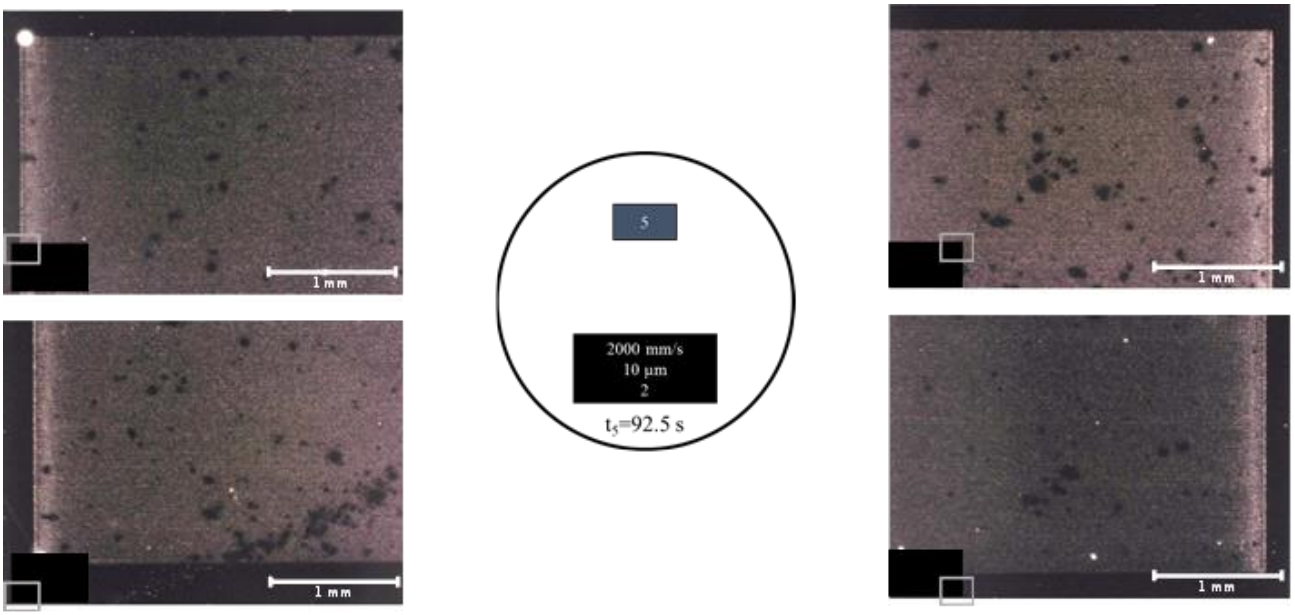

Figure 7.18. Sample area 5.

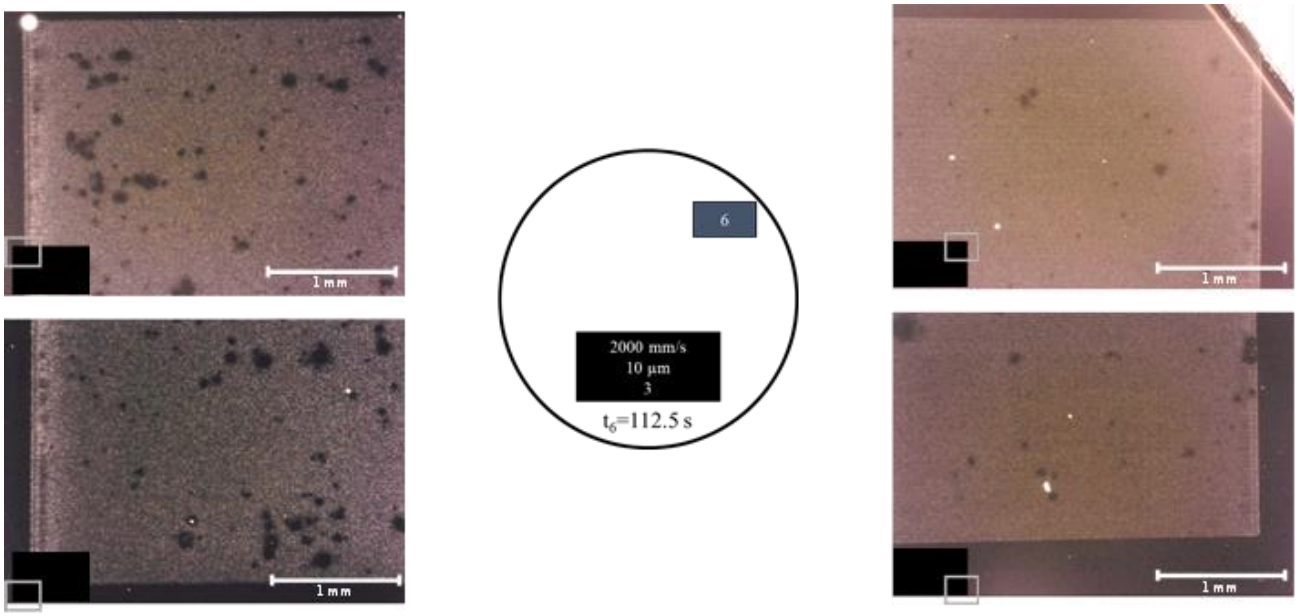

Figure 7.19. Sample area 6.

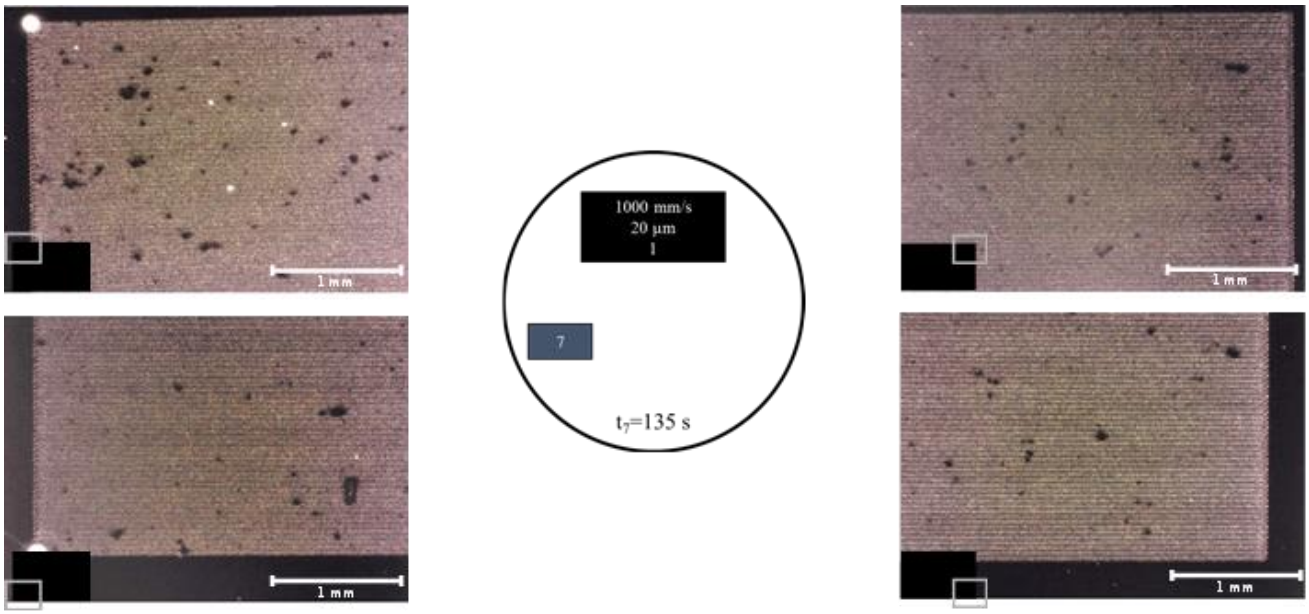

Figure 7.20. Sample area 7.

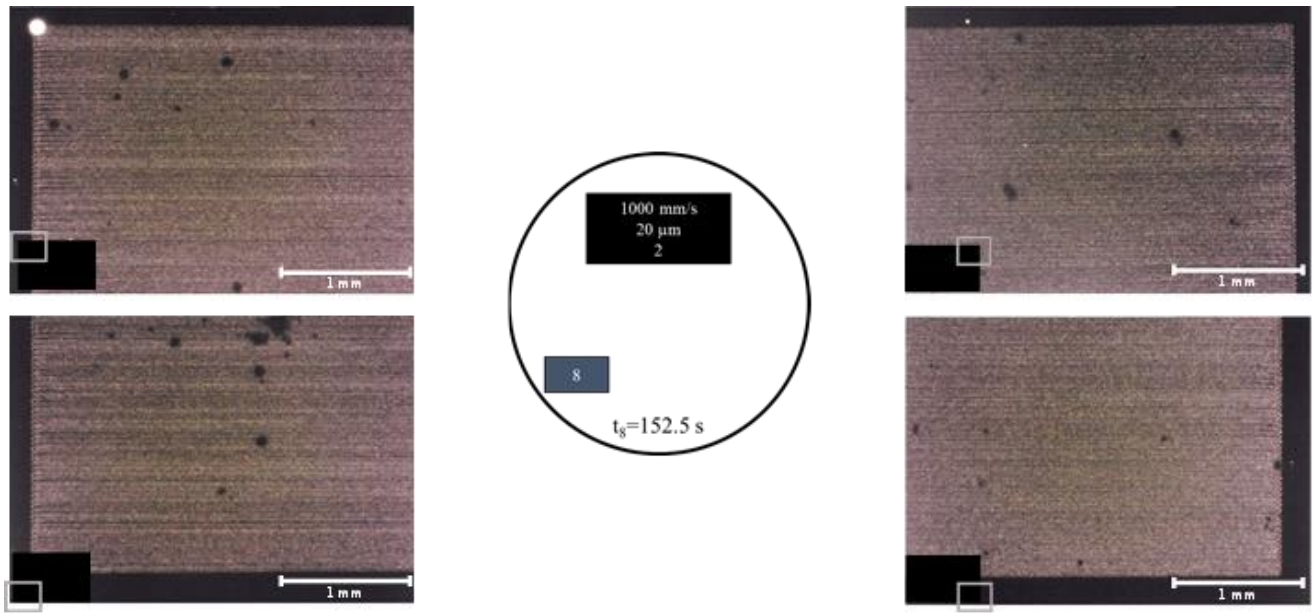

Figure 7.21. Sample area 8.

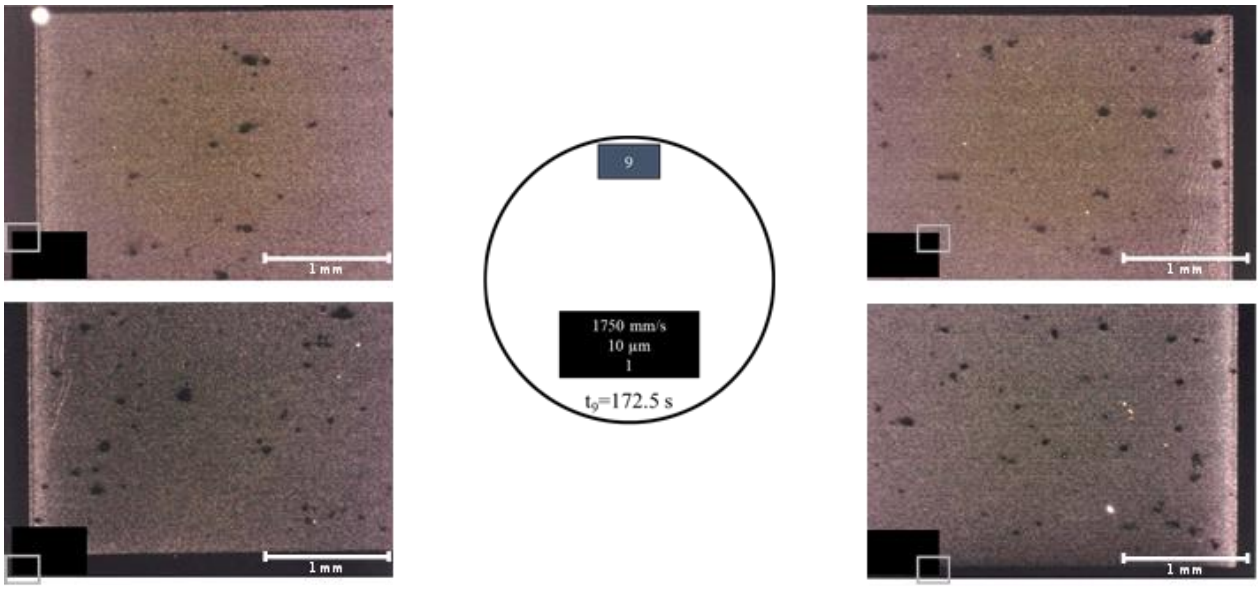

Figure 7.22. Sample area 9.

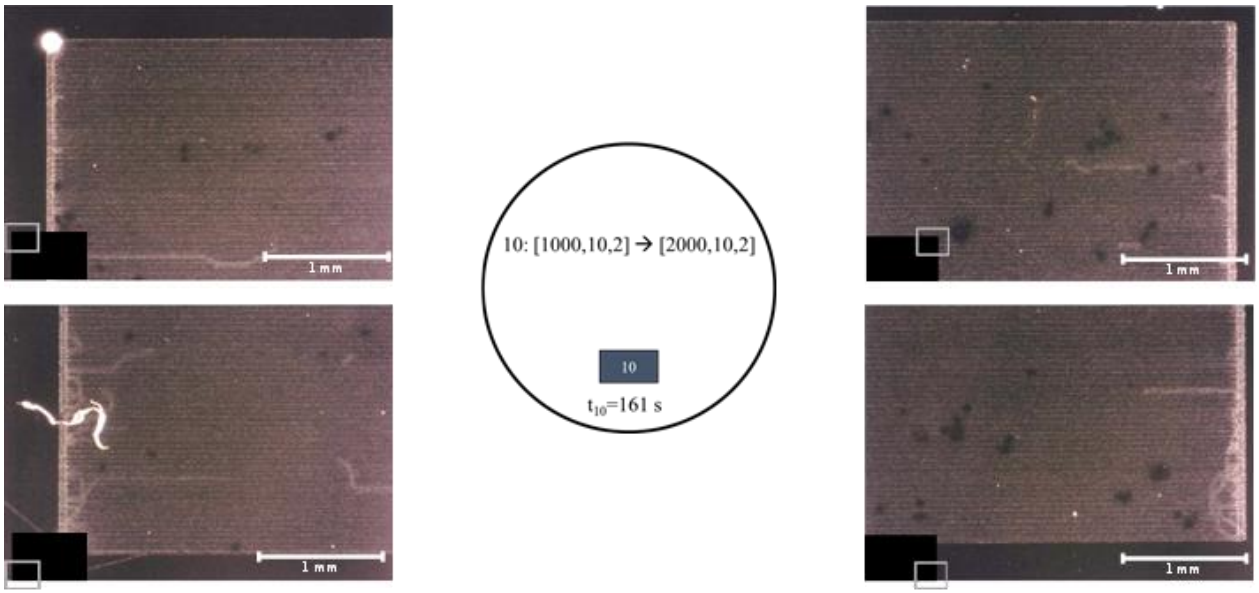

Figure 7.23. Sample area 10.

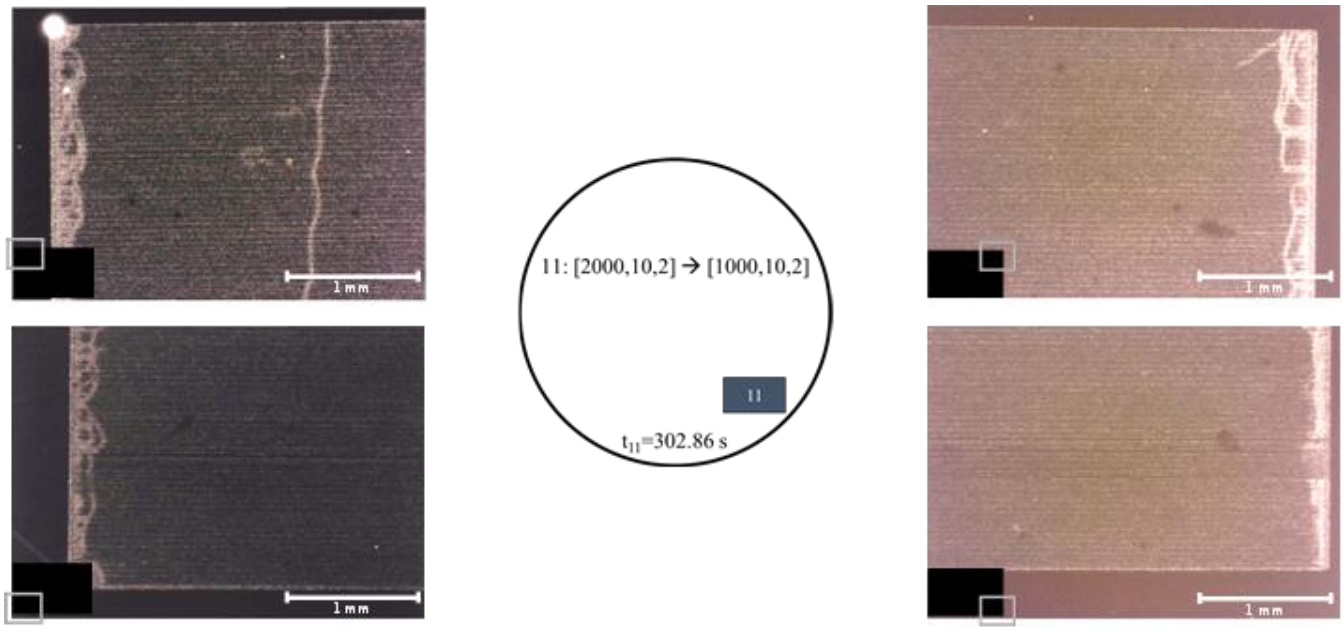

Figure 7.24. Sample area 11.

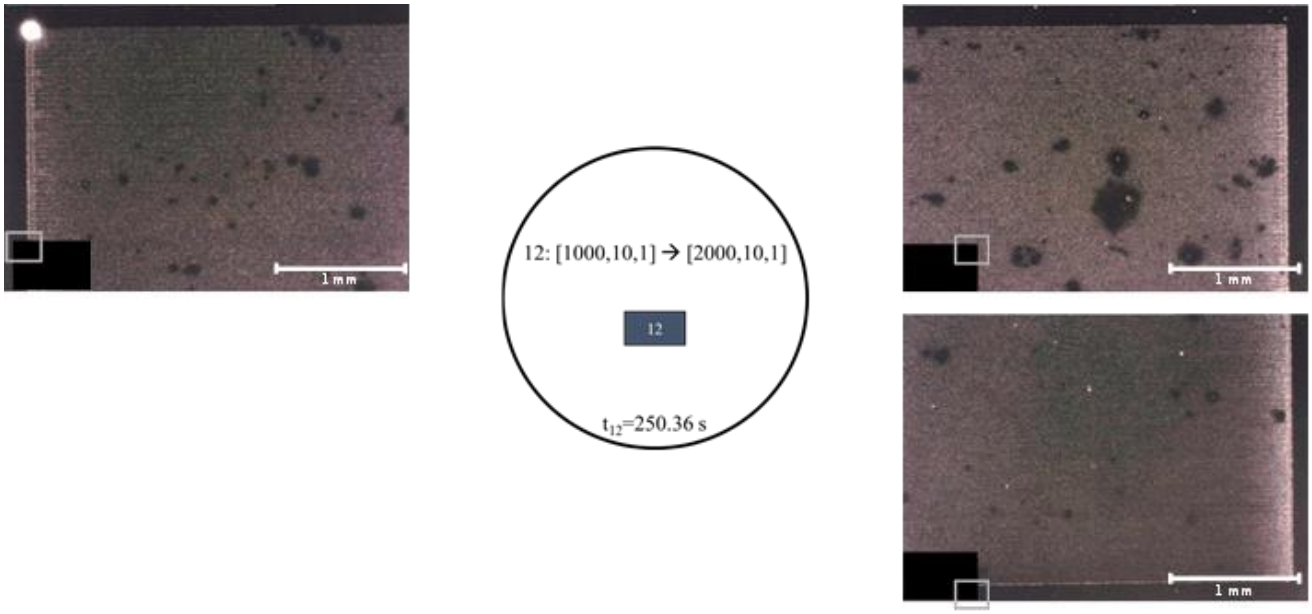

Figure 7.25. Sample area 12. The bottom left corner was not registered.

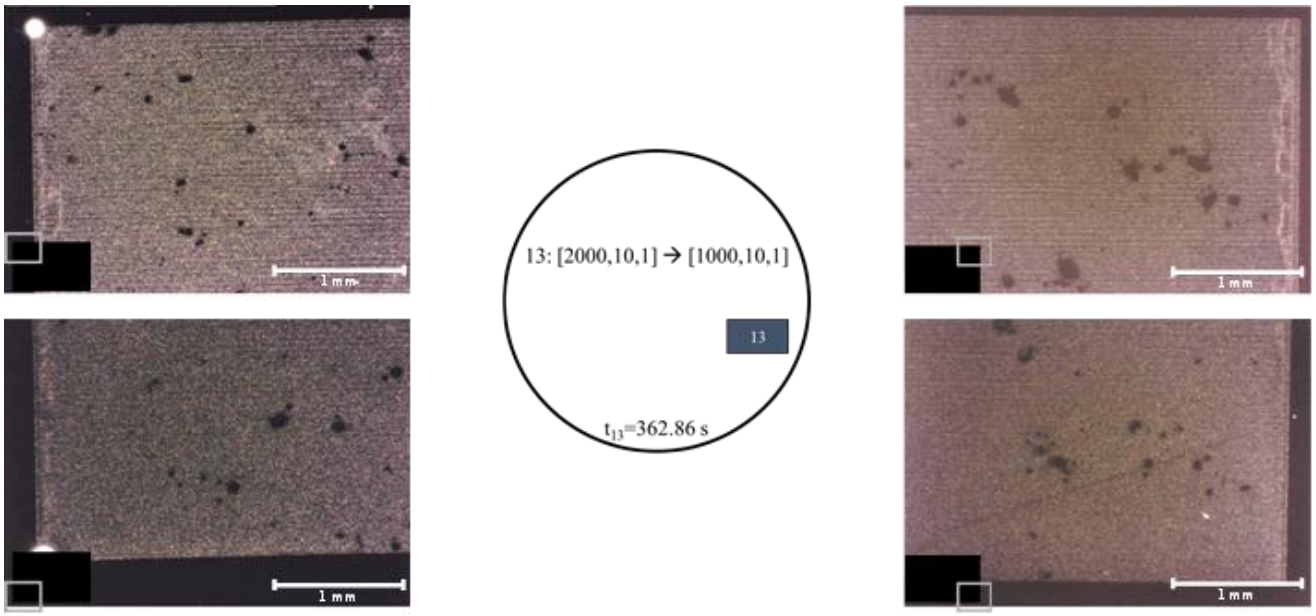

Figure 7.26. Sample area 13.

7.3. Annex C – Emitter using Polycarbonate window (2020-12-04)

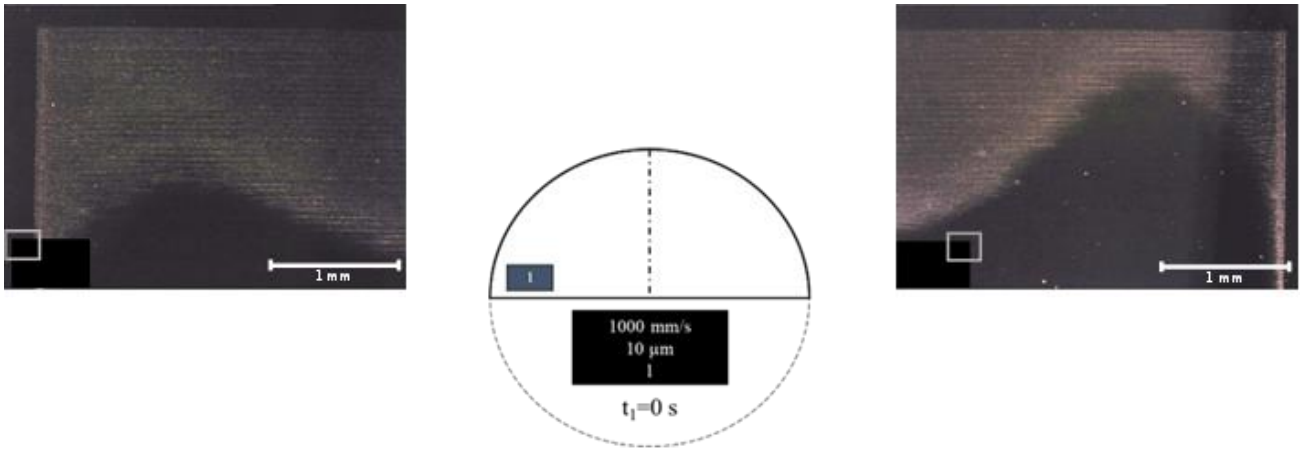

Figure 7.27. Sample area 1. The bottom corners were totally pitch-black areas.

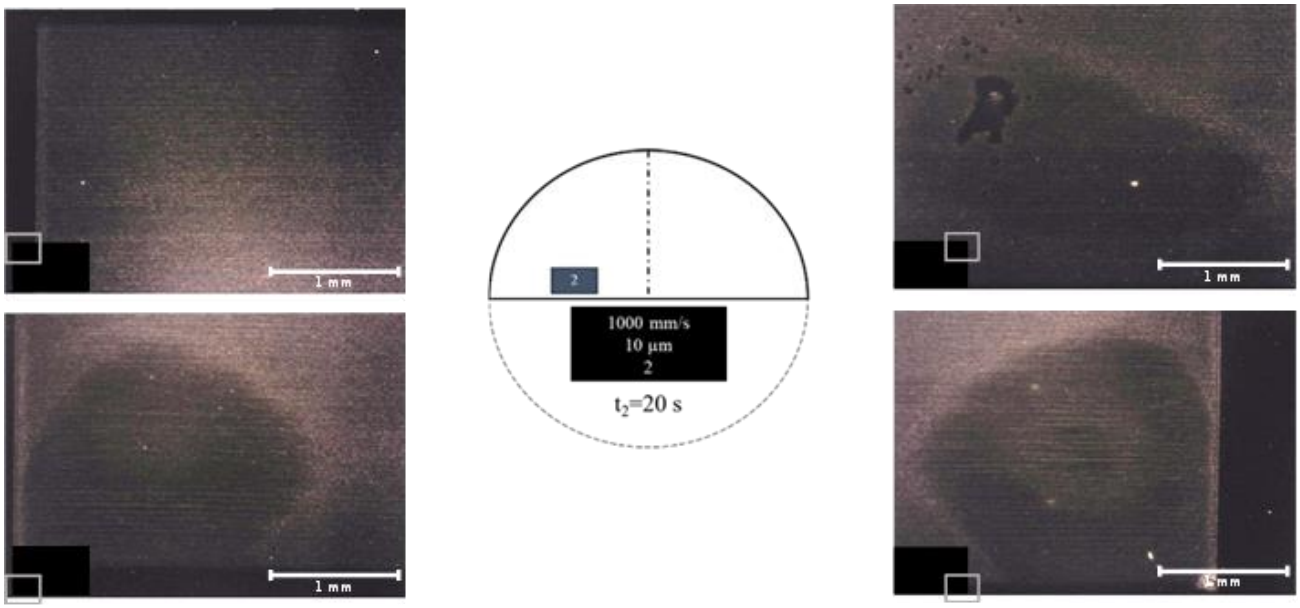

Figure 7.28. Sample area 2.

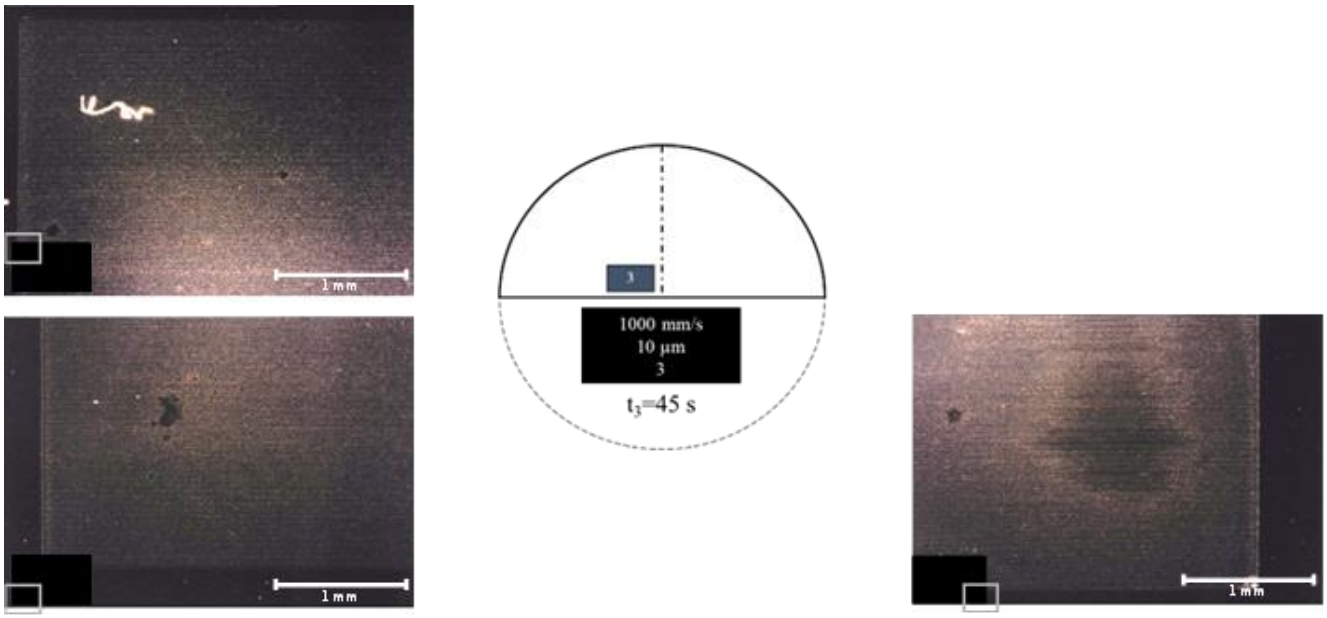

Figure 7.29. Sample area 3.

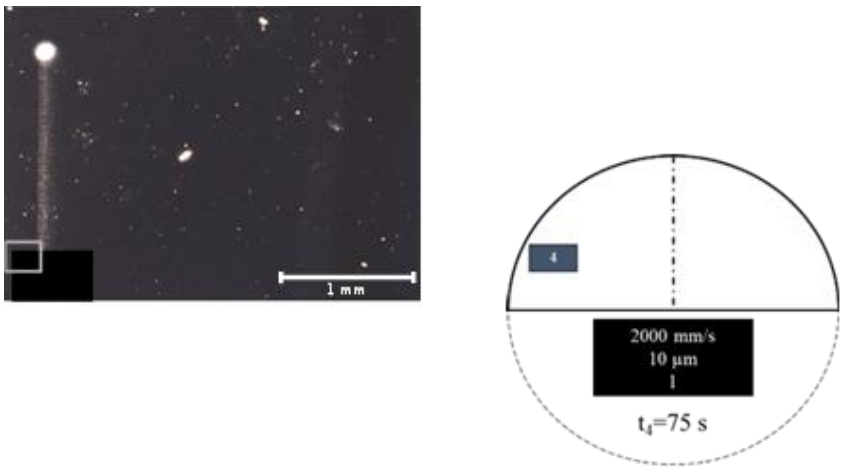

Figure 7.30. Sample area 4. No interaction in the entire treated area.

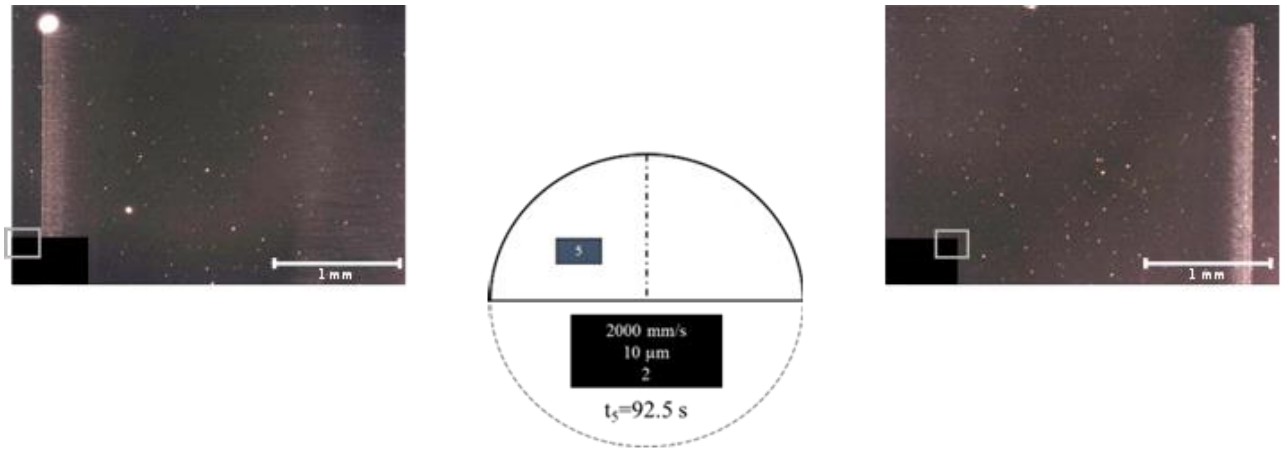

Figure 7.31. Sample area 5. Bottom corners were not registered, nearly total black area (no interaction).

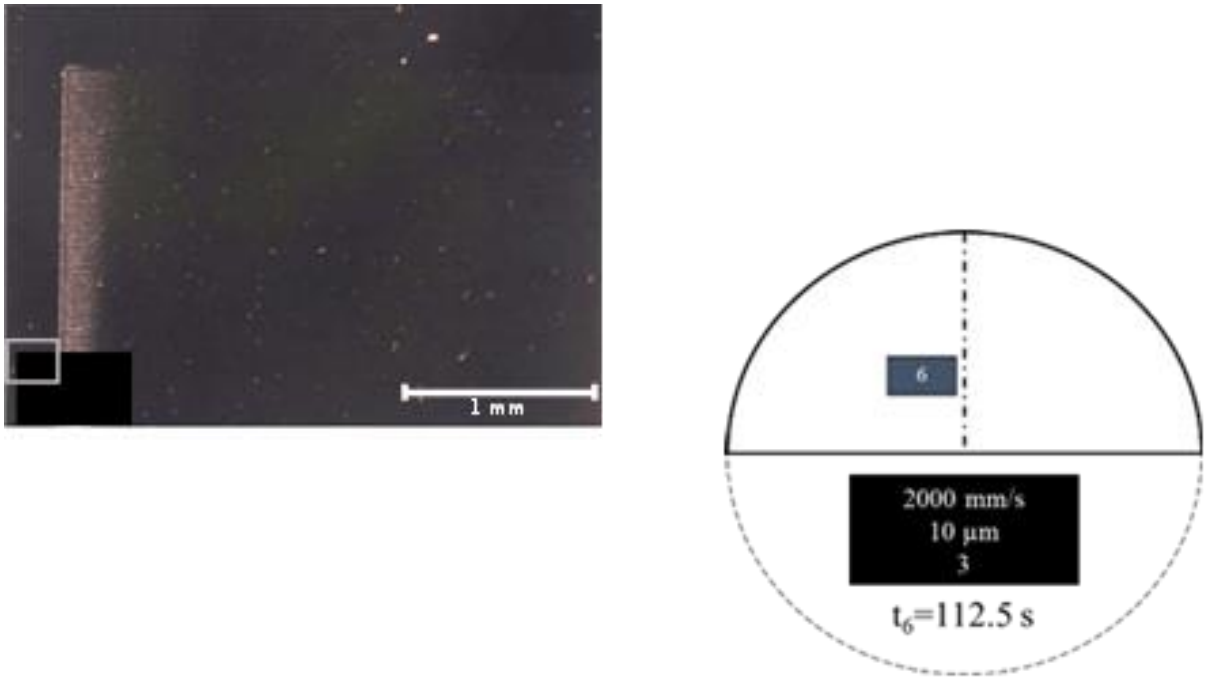

Figure 7.32. Sample area 6. No interaction in the missing corners.

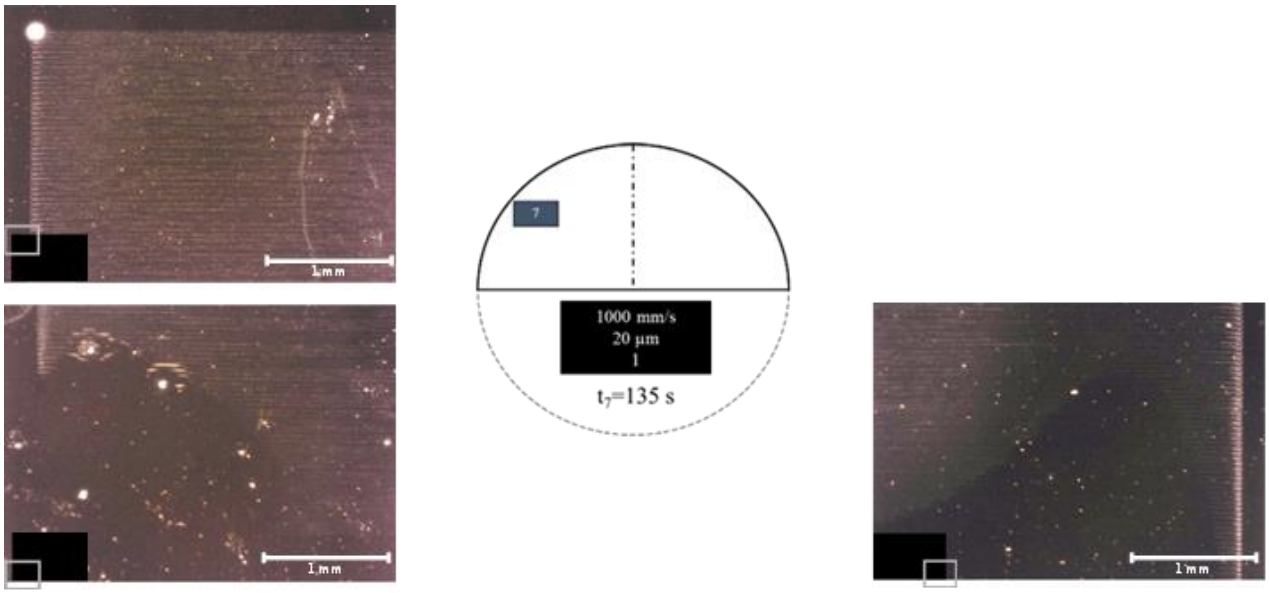

Figure 7.33. Sample area 7. Top right corner was not registered.

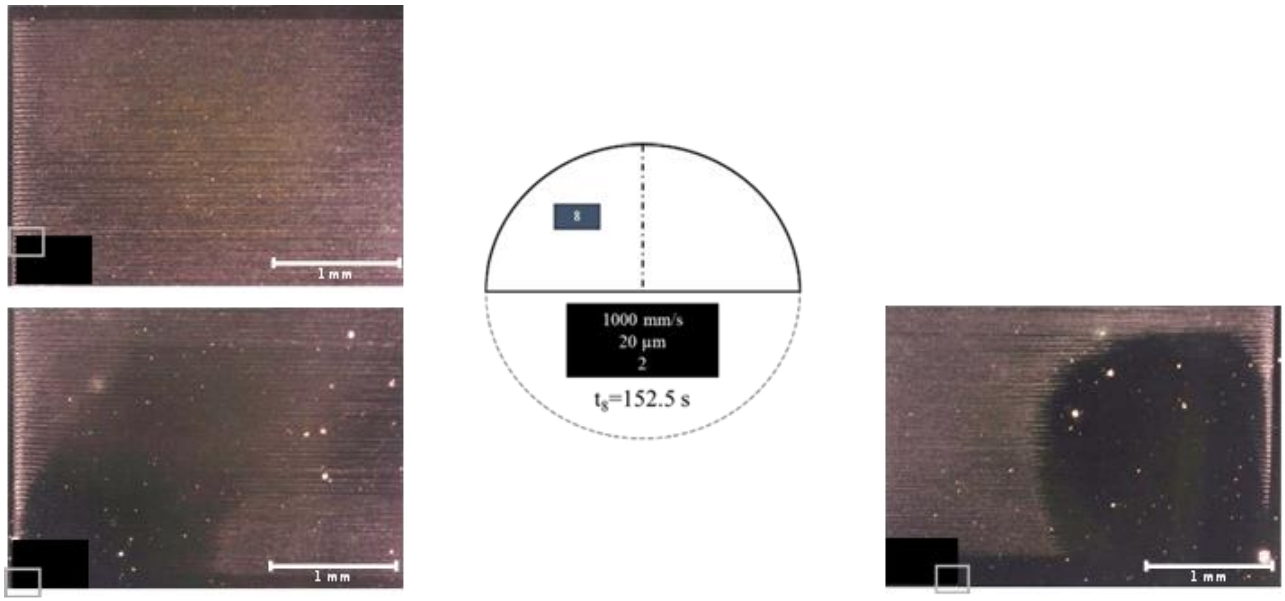

Figure 7.34. Sample area 8. Top right corner was not registered.

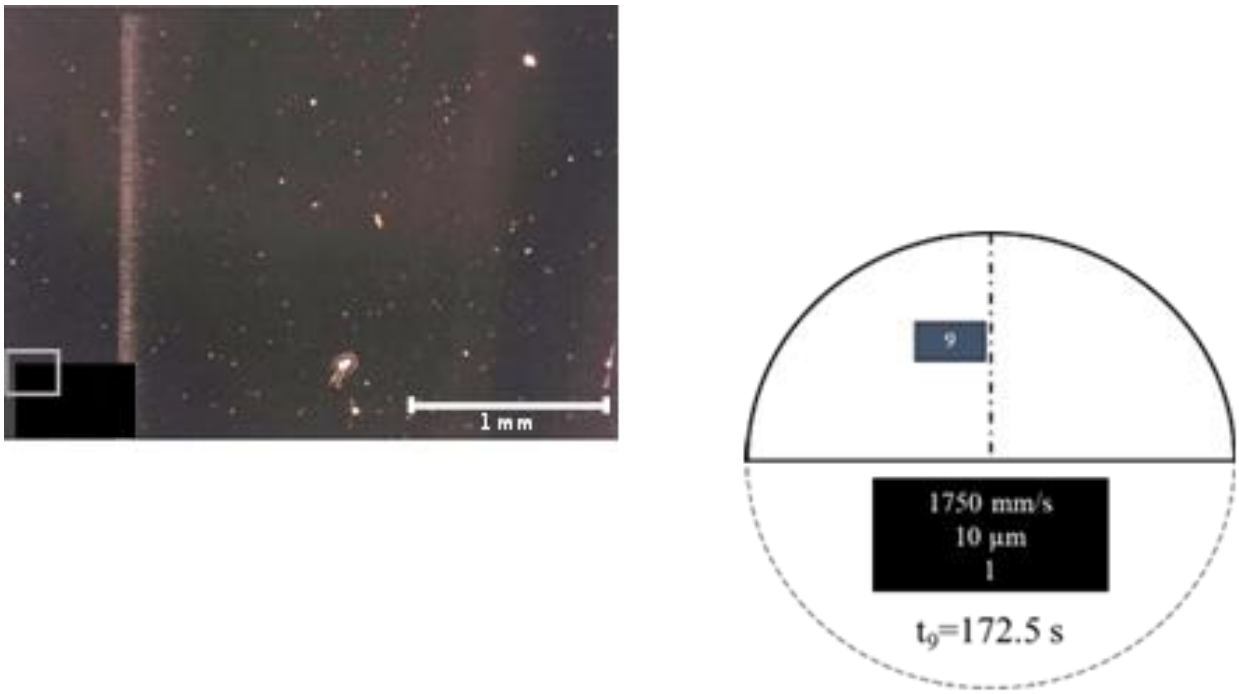

Figure 7.35. Sample area 9. The missing corners were not registered since there was no interaction.

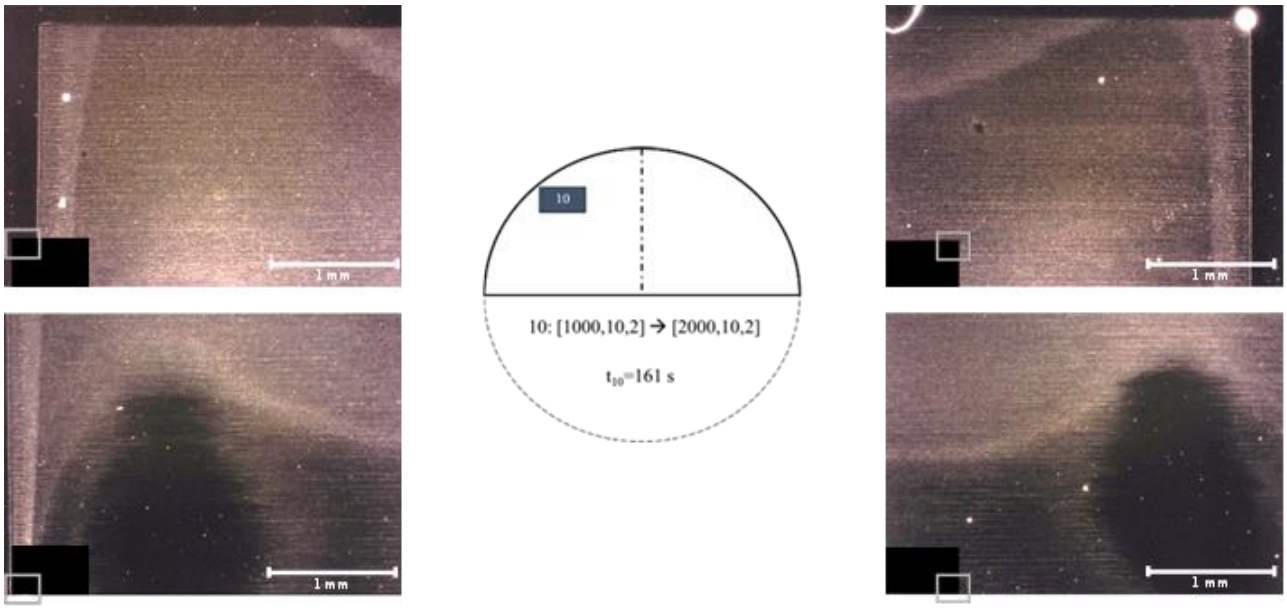

Figure 7.36. Sample area 10.

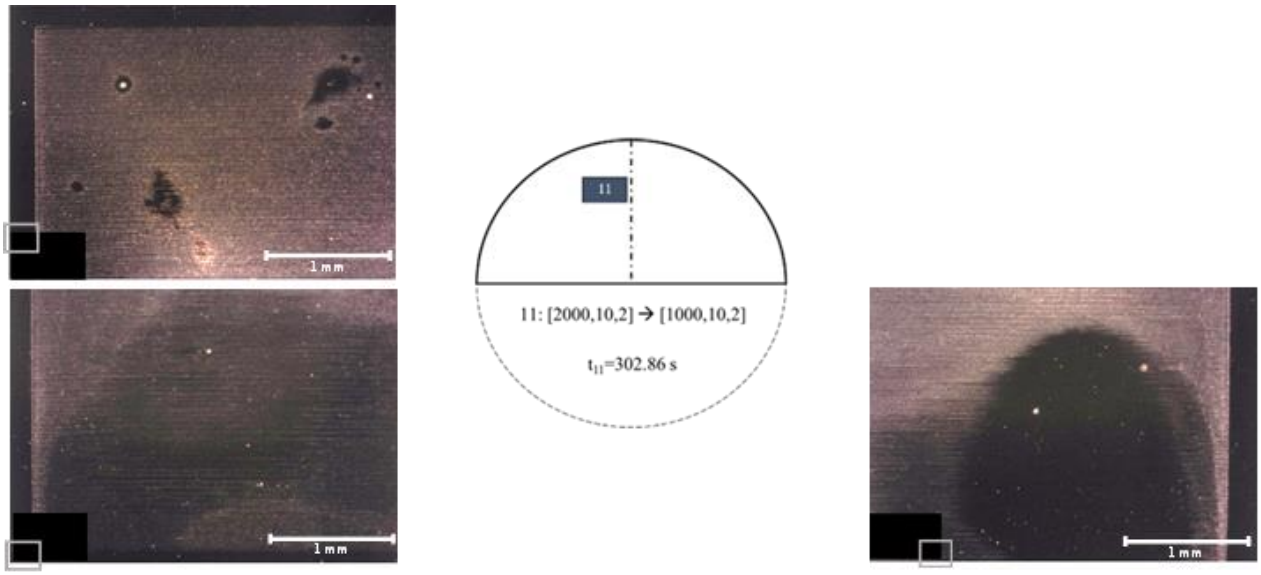

Figure 7.37. Sample area 11. Top right corner was not registered.

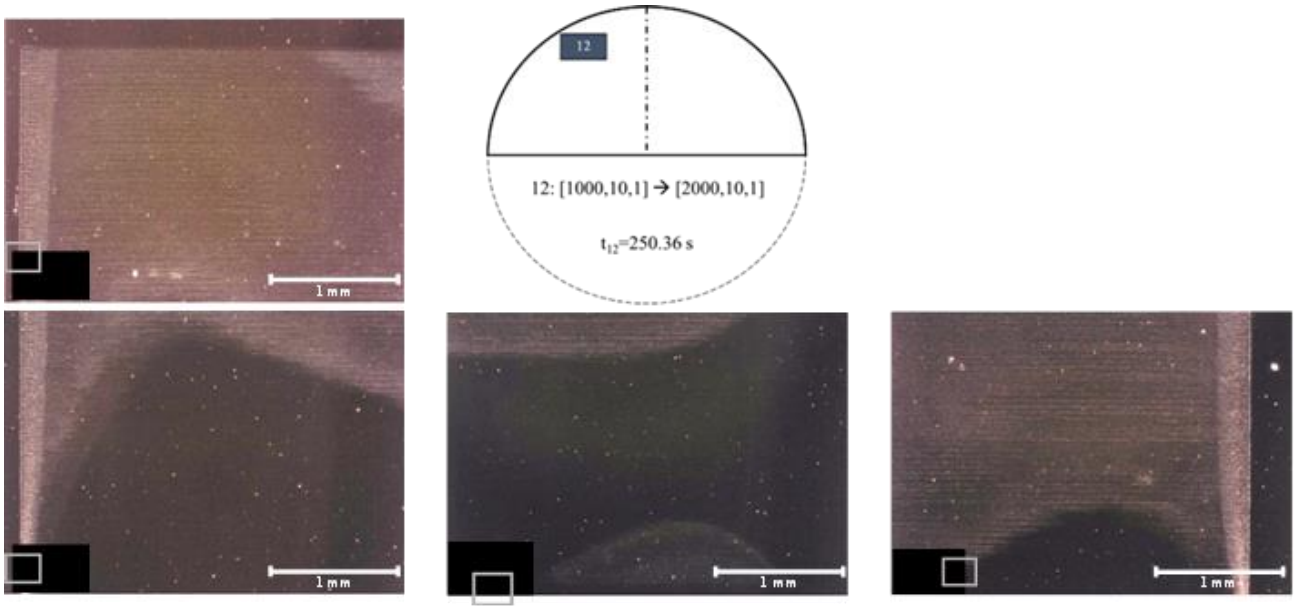

Figure 7.38. Sample area 12. Top right corner was not registered.

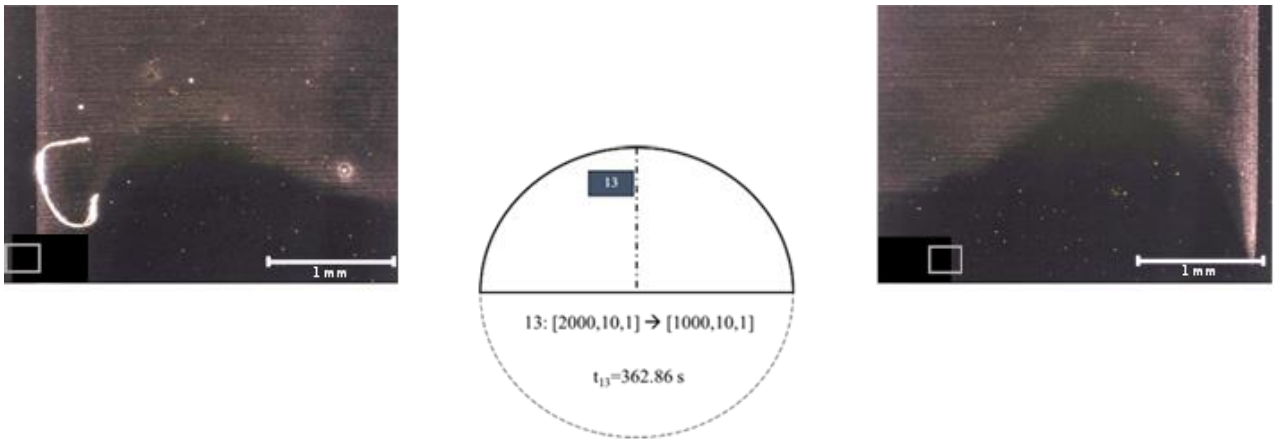

Figure 7.39. Sample area 13. Bottom half of this sample area was completely pitch-black.

7.4. Annex D – Single and superficial sets comparison

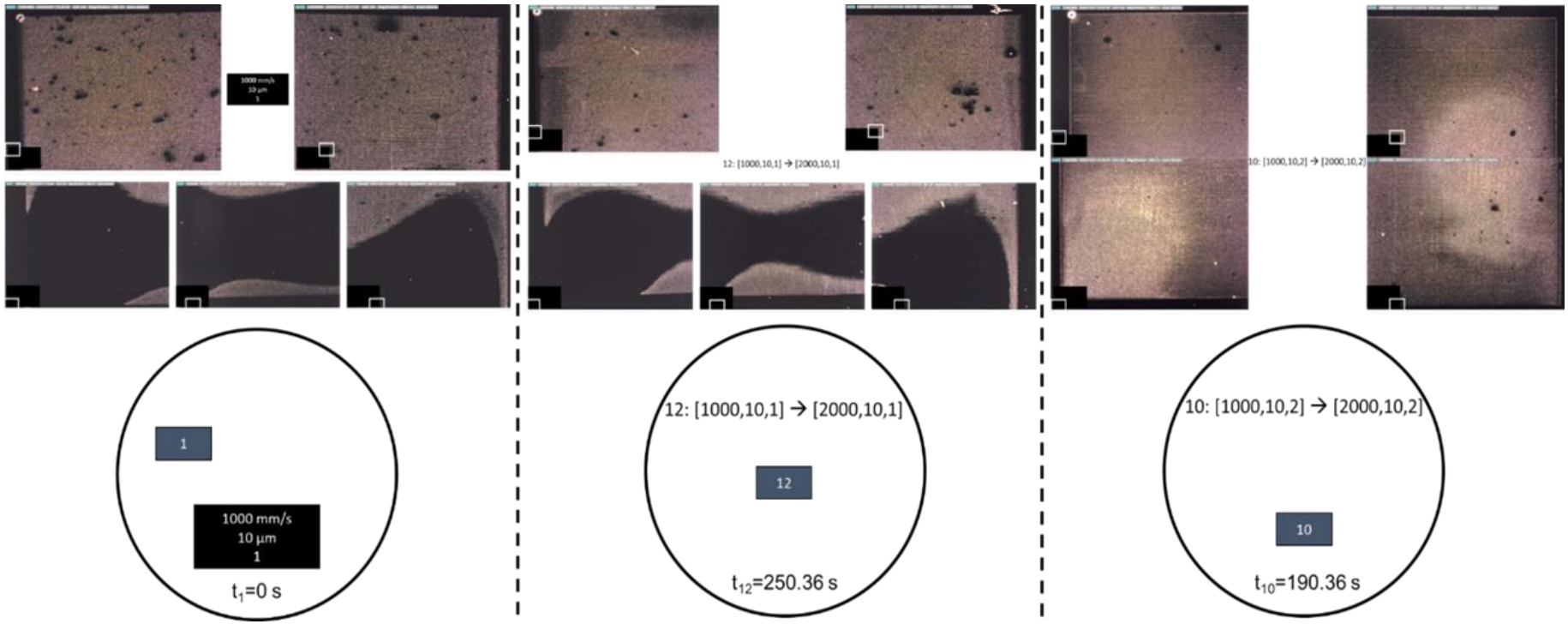

Figure 7.40: Comparison between a single scan set, the superficial melting and the in-depth melting. Polycarbonate window.

7.5. Annex E – Scheme of the similar and associated set of scans

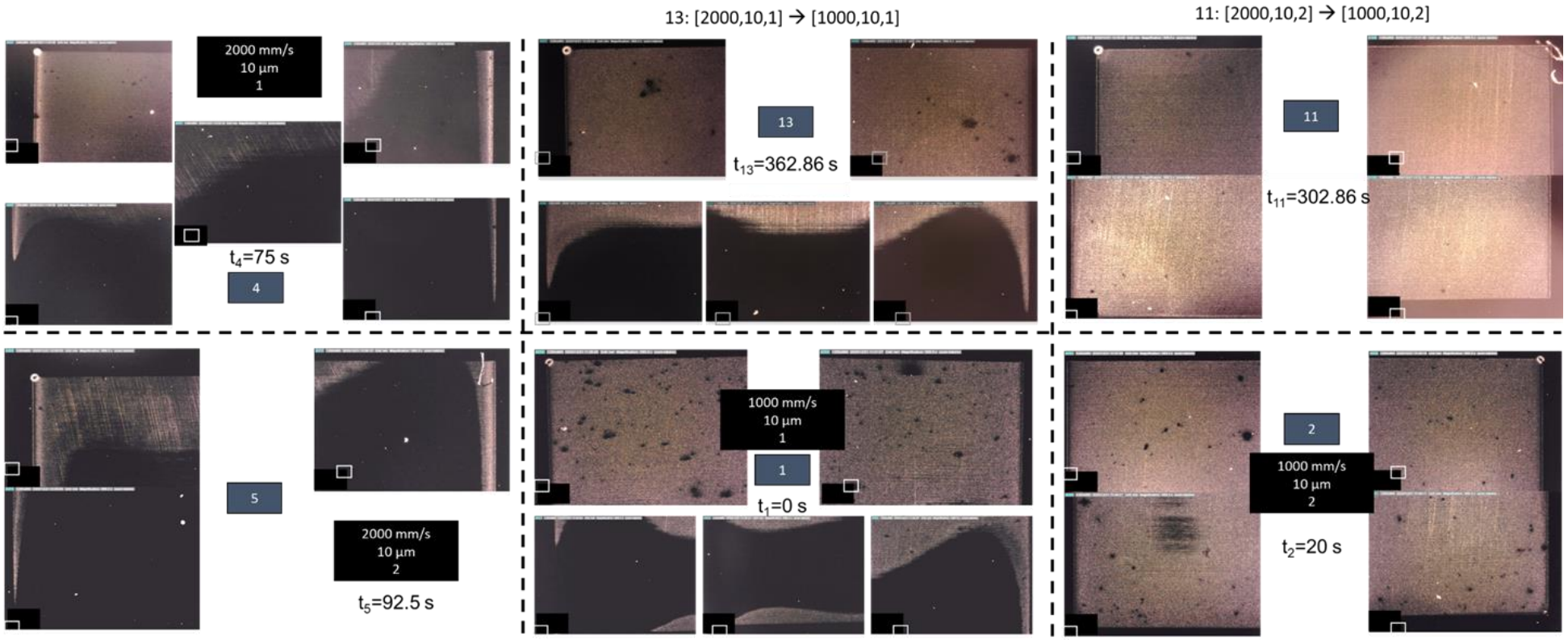

Figure 7.41: Comparison between related set of parameters

7.6. Annex F – Horizontal latent heat phenom

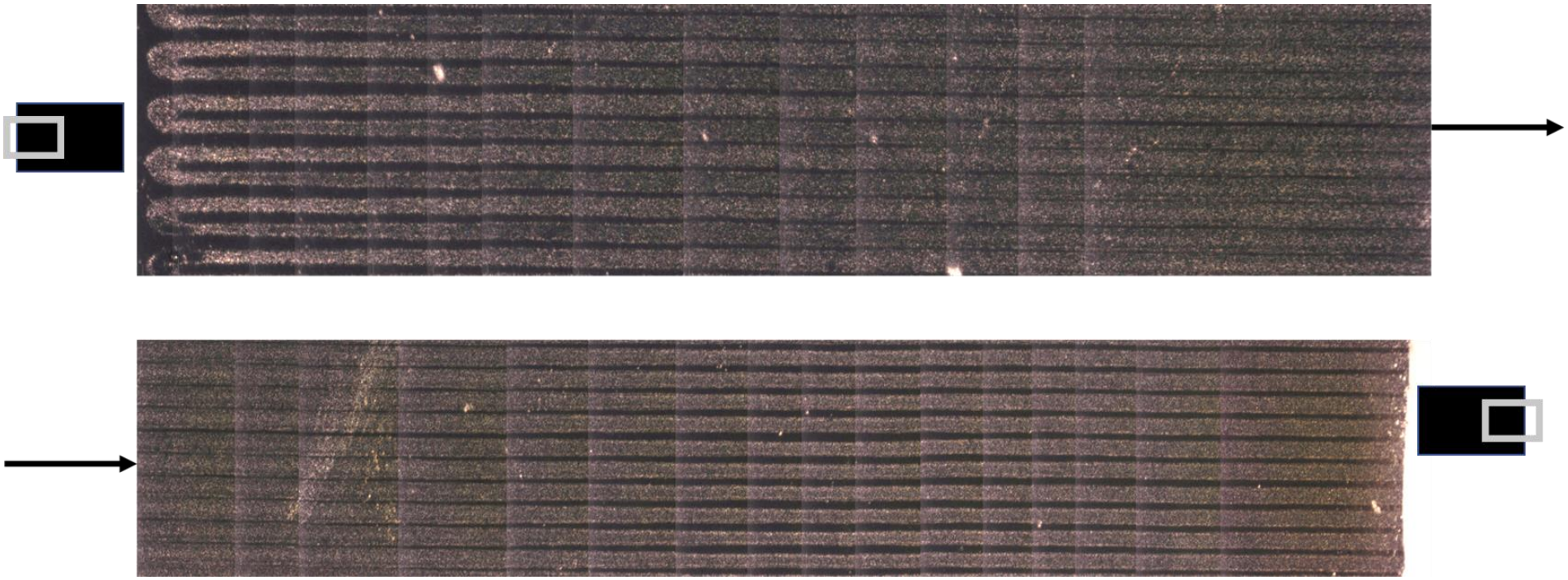

Figure 7.42: Horizontal profile of a sample area. Normal wafer using polycarbonate window with a parameter set of [1000,40,2].

7.7. Annex G – Parameters setup on the laser software

- SC 0';
- 'SI 1000' (sets the laser power to 100%, 20W);
- 'SR 350000' (if the objective is cutting samples – 350 kHz) or 'SR 500000' (if the objective is creation of samples – 500 kHz);
- 'GI' or 'GR' (To check the power and frequency, respectively);
- 'SS 0';
- 'SS 1'.

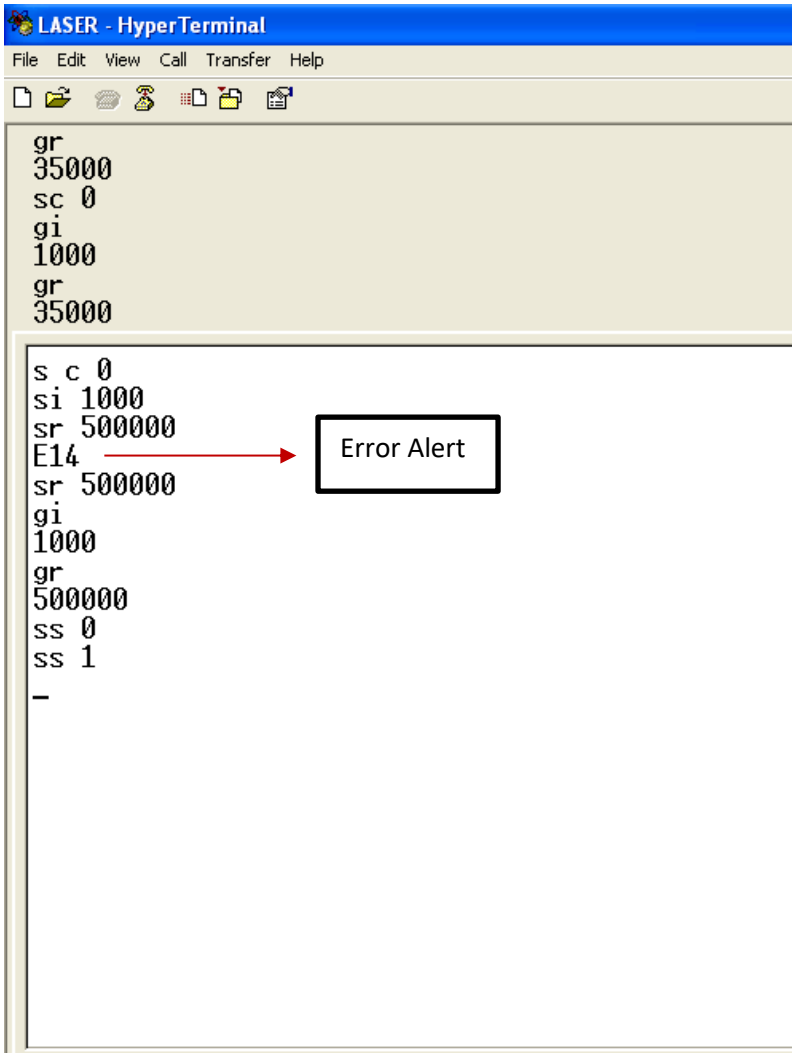

Figure 7.43: HyperTerminal parameters setup.